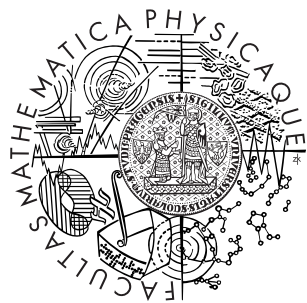


Univerzita Karlova v Praze  
Matematicko-fyzikální fakulta

## DIPLOMOVÁ PRÁCE



Radek Žlebčík

### **Studium produkce dijetů ve fotoprodukčních interakcích na HERA**

Ústav částicové a jaderné fyziky

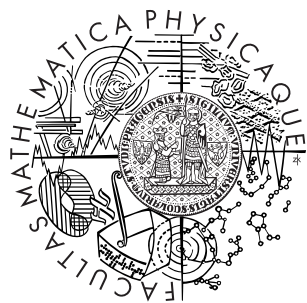
Vedoucí diplomové práce: RNDr. Alice Valkárová, DrSc.  
Studijní program: Fyzika Mgr., Jaderná a částicová fyzika

2011



Charles University in Prague  
Faculty of Mathematics and Physics

## DIPLOMA THESIS



Radek Žlebčík

## The Study of Diffractive Dijet Production in Photoproduction at HERA

Institute of Particle and Nuclear Physics

Supervisor: RNDr. Alice Valkárová, DrSc.  
Master Degree in Physics, Nuclear and Particle Physics

2011



## Acknowledgements

On the first place, I would like to thank my supervisor Alice Valkárová, who was always ready to give me useful advice and the time spent consulting various problems belonged to the most beautiful moments. She also introduced me to the diffractive group in DESY, where I had the opportunity to present my results.

My thesis could not arise without the assistance of other members from Prague diffractive group, specially Karel Černý, who initiated me to many procedures and programs used in this thesis.

I also want to express my gratitude to Jiří Chýla, who helped me with the theoretical aspects of this task.

## Poděkování

Velký dík patří v první řadě mé vedoucí Alici Valkárové, která mi byla vždy oporou a chvíle strávené konzultací nejrůznějších problémů patřily k těm nejhezčím. Představila mě taktéž difrakční skupině v DESY, kde jsem několikrát své výsledky prezentoval.

Má práce by nemohla vzniknout ani bez podpory ostatních členů pražské difrakční skupiny, zejména Karla Černého, který mě zasvětil do mnohých postupů a programů použitých v této práci.

Průvodcem po teoretických aspektech mi byl mimo jiné Jiří Chýla, kterému tímto rovněž děkuji.



Prohlašuji, že jsem svou diplomovou práci napsal samostatně a výhradně s použitím citovaných pramenů. Souhlasím se zapůjčováním práce a jejím zveřejňováním.

Beru na vědomí, že se na moji práci vztahují práva a povinnosti vyplývající ze zákona č. 121/2000 Sb., autorského zákona v platném znění, zejména skutečnost, že Univerzita Karlova v Praze má právo na uzavření licenční smlouvy o užití této práce jako školního díla podle § 60 odst. 1 autorského zákona.

V Praze dne 15.4.2011 Radek Žlebčík





*Dedicated to  
my future wife  
Helen.*

# Contents

<b>1</b>	<b>Introduction</b>	<b>5</b>
<b>2</b>	<b>Theory</b>	<b>6</b>
2.1	Deep Inelastic Scattering . . . . .	6
2.1.1	Kinematics . . . . .	6
2.1.2	Cross Section . . . . .	8
2.1.3	Parton model . . . . .	9
2.2	Quantum Chromodynamics . . . . .	10
2.2.1	Space Time Picture of Interaction . . . . .	11
2.2.2	Parton Distribution Functions . . . . .	13
2.2.3	QCD Matrix Element . . . . .	15
2.2.4	Hadronization . . . . .	16
2.3	Diffraction . . . . .	18
2.3.1	Kinematics . . . . .	19
2.3.2	Regge Phenomenology of Diffraction . . . . .	21
2.3.3	Factorisation in Inclusive Diffractive DIS . . . . .	23
2.3.4	Regge Factorisation of DPDFs . . . . .	25
2.3.5	Factorisation in Diffractive Dijet Photoproduction . . . . .	26
2.3.6	Methods of Detection of Diffractive Events . . . . .	27
<b>3</b>	<b>Motivation and Recent Results</b>	<b>32</b>
3.1	HERA Collider . . . . .	32
3.1.1	H1 Detector . . . . .	33
3.1.2	ZEUS Detector . . . . .	34
3.2	DPDFs from Diffractive Inclusive Data . . . . .	34
3.3	Diffraction Measured by Forward Proton Spectrometers . . . . .	36
3.4	Diffractive Dijet Production in DIS . . . . .	39
3.5	Factorisation Breaking in Hadron-Hadron Collisions . . . . .	41
3.6	Diffractive Dijet Photoproduction . . . . .	43
3.7	Diffractive Open Charm Production in Photoproduction . . . . .	48

<b>4</b>	<b>Crosscheck of H1 and ZEUS Results</b>	<b>50</b>
4.1	Reconstruction Formulas . . . . .	50
4.2	Parton-Level NLO Calculations . . . . .	52
4.3	Hadronization Corrections . . . . .	53
4.4	Hadron-Level NLO QCD Predictions . . . . .	65
4.5	Alternative Photon Structure Function . . . . .	66
<b>5</b>	<b>Extrapolation between Measurements</b>	<b>74</b>
5.1	Description of the Method . . . . .	74
5.2	H1 Low Pt $\rightarrow$ H1 High Pt . . . . .	76
5.3	ZEUS $\rightarrow$ H1 High Pt . . . . .	76
5.4	H1 Low Pt $\rightarrow$ ZEUS . . . . .	76
<b>6</b>	<b>Conclusions</b>	<b>81</b>

**Abstrakt:** V této práci jsou analyzována současná měření difrakční fotoprodukce dijetů na urychlovači HERA s důrazem na možné narušení faktorizace. Jsou zkoumány možné důvody rozdílnosti studií H1 a ZEUS kolaborací, jako rozdílné hadronizační korekce a rozdílný fázový prostor obou měření.

Klíčová slova: difrakční fotoprodukce, dijet, suppression

**Abstract:** Recent experimental data on dijet cross section in diffractive photoproduction at HERA collider are analyzed with an emphasis on QCD factorization breaking effects. The possible sources of the contradiction in conclusions of H1 and ZEUS collaborations such as different hadronization corrections and different phase space of both analysis are studied.

Keywords: diffractive photoproduction, dijet, suppression

# Chapter 1

## Introduction

Diffractive events in high energy  $pp$  or  $ep$  collisions are characterized by the presence of a leading proton or anti-proton, which remains intact and by presence of a rapidity gap between a leading  $p(\bar{p})$  and the hadronic system.

One of the most interesting questions which are discussed in the studies of such diffractive processes with the hard scale, like photon virtuality or transverse jet energy, is whether they can be considered being factorisable into diffractive parton distribution functions and perturbatively calculable partonic cross sections. Such concept, called hard QCD factorisation, was theoretically and experimentally probed to be valid in the regime of diffractive  $ep$  deep inelastic scattering.

On the other hand far from clear is the situation in the photoproduction regime of the diffractive  $ep$  scattering. Small virtuality of the exchanged photon in photoproduction allows for partonic fluctuations that live long enough. It means that the photon does not need to interact directly, but could act as a hadron with similar quantum numbers like the photon. Structure of such (resolved) photon is described by photon distribution functions.

These resolved photon interactions resemble hadron-hadron ones since two particles with the structure scattered on each other. However the factorisation concept was found not to be valid for hard processes in diffractive hadron-hadron scattering as measured for example in  $p\bar{p}$  interactions at Tevatron.

The puzzle of the validity of factorisation in diffractive photoproduction of dijets is even more emphasize by the presence of analyses with contradictory conclusions about factorisation breaking made by H1 and ZEUS collaborations.

In this thesis the possible sources of the contradiction in conclusions of H1 and ZEUS collaborations such as different hadronization corrections, NLO QCD calculations and different phase space of both analyses are studied.

# Chapter 2

## Theory

### 2.1 Deep Inelastic Scattering

#### 2.1.1 Kinematics

Deep inelastic scattering (DIS) is in general scattering of charged ( $e, \mu, \tau$ ) or neutral ( $\nu_e, \nu_\mu, \nu_\tau$ ) leptons on nucleons. In DIS the virtuality of the exchanged intermediate particle is much higher than mass of the nucleon. Further we restrict our discussion to  $ep$  interactions where  $e$  is electron or positron

$$e(k) + p(P) \rightarrow e(k') + X(P_X) \quad (2.1)$$

and  $k, P, k'$  and  $P_X$  are four-momentum vectors (see Fig. 2.1). Proton dissociates to a hadronic final state (HFS)  $X$  which has higher invariant mass than proton while electron stays intact.

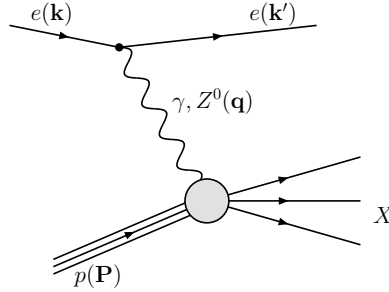


Fig. 2.1: The leading order Feynman diagram for DIS.

To describe the kinematics of this process, the following invariants are useful (electron mass is always neglected, neglecting of proton mass is expressed by  $\simeq$ ):

- Total energy square in the center of mass system (CMS)

$$s = (k + P)^2 \simeq 4E_e^{beam} E_P^{beam}. \quad (2.2)$$

- Virtuality of the exchanged intermediated particle ( $\gamma^*$  or  $Z^0$ )

$$Q^2 = -q^2 = -(k - k')^2. \quad (2.3)$$

- Inelasticity (relative loss of electron energy in the proton rest system)

$$y = \frac{qP}{kP} = \frac{E_e^{lab} - E_e'^{lab}}{E_e^{lab}} \simeq \frac{W^2 + Q^2}{s}. \quad (2.4)$$

- Fraction of the proton four-momentum transferred to the interaction

$$x = \frac{Q^2}{2qP} \simeq \frac{Q^2}{W^2 + Q^2}. \quad (2.5)$$

- Invariant mass of HFS

$$W^2 = M_X^2 = (q + P)^2 = M_P^2 + \left(\frac{1}{x} - 1\right) Q^2. \quad (2.6)$$

Elastic scattering occurs if  $W = M_P \Leftrightarrow x = 1$ .

In case of unpolarized particles only two variables are independent (except of CMS energy which is usually the same for all events). This statement can be seen with the help of the relation

$$xy = \frac{Q^2}{s - M_P^2} \simeq \frac{Q^2}{s}. \quad (2.7)$$

Common choice of these two independent variables is  $(x, Q^2)$ ,  $(y, Q^2)$  or  $(x, y)$ . If particle masses are neglected then  $0 < x < 1$ ,  $0 < y < 1$  and  $0 < Q^2 < s$ .

Previous quantities can be obtained for example from  $\theta'$ ,  $E_e'$  measurement of the scattered electron.

## Rapidity

Useful variable to describe a polar angle of the particle is a rapidity  $y_\eta$  defined as

$$y_\eta = \frac{1}{2} \ln \frac{E + p_z}{E - p_z} \quad (2.8)$$

where  $E$  is the energy and  $p_z$  the third component of momentum. If we define transverse energy as  $E_T = \sqrt{m^2 + p_T^2}$ , then the  $E$  and  $p_z$  are expressed as

$$E = E_T \cosh y_\eta \quad (2.9)$$

$$p_z = E_T \sinh y_\eta \quad (2.10)$$

and Sudakov variables  $p_\pm$  are then defined as

$$p_\pm = \frac{1}{\sqrt{2}}(E \pm p_z) = \frac{1}{\sqrt{2}}E_T e^{\pm y_\eta}. \quad (2.11)$$

Difference of rapidities is invariant with respect to boost along  $z$  axis<sup>1</sup>. For relativistic particles  $E \gg m$  the rapidity can be approximately expressed as

$$y_\eta = -\ln \tan \frac{\theta}{2}. \quad (2.12)$$

Formula (2.12) is simultaneously definition of pseudorapidity  $\eta$  for particles with arbitrary energy.

### 2.1.2 Cross Section

In considered kinematics region ( $Q^2 \ll M_Z^2$ ) the  $Z^0$  contribution can be safely neglected hence  $\gamma^*$  exchange dominates. Photon acts here as a probe of the proton with a characteristic size of  $1/Q$ . From fundamental principles like Lorentz invariance, parity conservation and gauge invariance of electromagnetic interactions follows that cross section of DIS must have following form

$$\frac{d\sigma}{dx dQ^2} = \frac{4\pi\alpha_{em}^2}{Q^4} \left[ \left(1 - y - \frac{M_P^2 xy}{s}\right) \frac{F_2(x, Q^2)}{x} + \frac{1}{2} y^2 2F_1(x, Q^2) \right], \quad (2.13)$$

where  $\alpha_{em}$  is electromagnetic coupling and  $F_{1,2}$  are DIS structure functions of proton. For high energy scattering the term with proton mass could be neglected. We further assume validity of Callan-Gross relation [1]  $F_2 = 2xF_1$  which is exactly true in parton model approach discussed later. Taking into account these approximations, we obtain

$$\frac{d\sigma}{dx dQ^2} = \frac{4\pi\alpha_{em}^2}{Q^4} \left(1 - y + \frac{1}{2} y^2\right) \frac{F_2(x, Q^2)}{x}. \quad (2.14)$$

---

<sup>1</sup>If the moving system has a speed  $\beta$  then  $y'_\eta = y_\eta + \frac{1}{2} \ln \frac{1+\beta}{1-\beta}$  and  $E'_T = E_T$



### 2.1.3 Parton model

Small  $Q^2$  dependence of  $F_2$  for  $Q^2$  above resonances region in  $ep$  scattering (see Fig. 2.2) as was measured at SLAC [2] yields to an assumption that electron is scattered on point-like proton's constituents. It means that proton is composed from more elementary objects called partons and  $\gamma^*$  interacts only with one of them, others stay intact (see Fig. 2.3). It is obvious that these partons must carry electric charge. In this approach  $x$  has a clear interpretation as a fraction of the proton momentum carried by the struck parton.

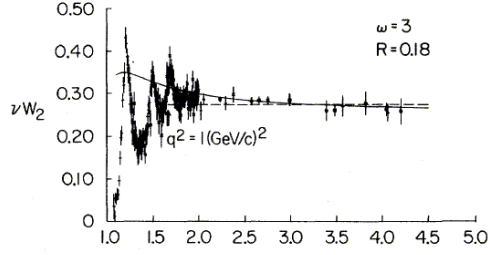


Fig. 2.2: SLAC measurement of  $F_2 = \nu W_2$  dependence on  $Q^2$  (in  $\text{GeV}^2$ ) for  $x = 1/\omega = 1/3$  [2].

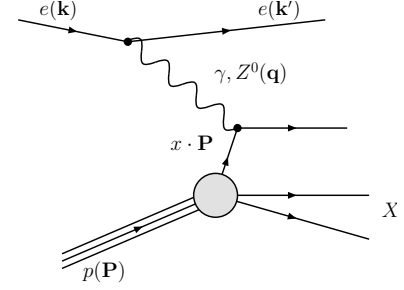


Fig. 2.3: Leading order Feynman diagram of  $ep$  collision in parton model

Cross section for scattering of two charged particles with spin 1/2 (electron and parton) neglecting its mass is according to quantum electrodynamics (QED)

$$\frac{d\sigma}{d\hat{Q}^2} = \frac{4\pi\alpha_{em}^2 e_q^2}{\hat{Q}^4} \left( 1 - y + \frac{1}{2}y^2 \right), \quad (2.15)$$

where  $e_q$  is electric charge of the corresponding parton. The previous formula is consistent with (2.14) if we suppose that proton is composed from partons with spin 1/2 and  $q_i(x)dx$ , respective  $\bar{q}_i(x)dx$ , is the probability that we find a parton, respective anti-parton, of type  $i$  with momentum fraction  $(x, x + dx)$  inside the proton. If the partons would be bosons with spin 0 or 1 the scattering formula analogous to (2.15) would be not consistent with the measurement. Proton structure function  $F_2$  is therefore within parton model expressed as

$$F_2(x, Q^2) = x \sum_i e_i^2 (q_i(x) + \bar{q}_i(x)). \quad (2.16)$$

As the parton distribution functions (PDFs) behave like  $1/x$  for small  $x$  (see Fig. 2.4), mean number of partons of type  $i$  inside proton ( $\int_0^1 q_i(x)dx$ ) goes to

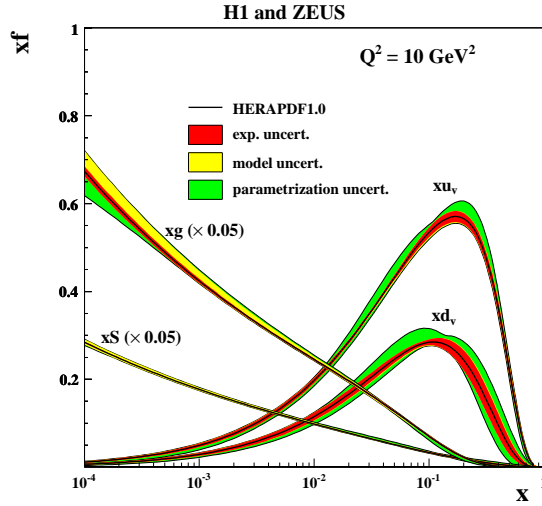


Fig. 2.4: DIS parton distribution functions as measured at HERA in 2010 [4].

infinity. The quantities which relate to the quarks in additive SU(3) quark flavour model [3] are so called valence parton distribution functions

$$q_i^{val}(x) = q_i(x) - \bar{q}_i(x). \quad (2.17)$$

Mean values of u and d quarks inside proton are then 2 and 1, respectively, in agreement with the additive quark flavour model. The flavour index  $i$  denotes up, down, strange, charm, bottom or top quark.

It is possible to measure total momentum fraction carried by the all quarks in proton

$$\int_0^1 dx x \Sigma(x) = \int_0^1 dx x \sum_i (q_i(x) + \bar{q}_i(x)) dx. \quad (2.18)$$

Value  $\simeq 0.5$  which was obtained indicates that there must be others, electrically neutral partons carrying remaining half of proton momentum. These partons were identified as gluons known from quantum chromodynamics.

## 2.2 Quantum Chromodynamics

Quantum chromodynamics (QCD) is non-abelian gauge theory of strong interaction based on SU(3) group. It describes interactions between quarks with spin 1/2 by exchange of gluons – massless gauge bosons with spin 1. Each quark has a

color ("strong charge"), analog of electric charge in QED. In contrast to quantum electrodynamics gluons have color too; the interaction between gluons is possible. There exist three colors for quarks and eight colors for gluons which correspond to dimension of fundamental representation and adjoint representation of SU(3) color group.

Strong interaction is characterised by a strong coupling constant  $\alpha_s$ . Contrary to QED this constant decreases with increasing renormalization scale which can be matched to  $Q^2$  in the case of inclusive DIS. It means that for very high energy (small distances) is the strong interaction negligible which is known as asymptotic freedom. On the other hand for small scales (close to  $\Lambda_{N_f}$  defined in (2.19)) strong constant grows which disables using of perturbative theory. These properties could be clearly seen from one-loop expression for  $\alpha_s$

$$\alpha_s(\mu/\Lambda_{N_f}) = \frac{1}{b \ln \mu/\Lambda_{N_f}} \quad \text{where} \quad b = \frac{33 - 2N_f}{6\pi} \quad (2.19)$$

and the number of active flavors is denoted as  $N_f$ . Constant  $\Lambda_4 \doteq 0.2 \text{ GeV}$  or equivalently  $\alpha_s(M_Z) \doteq 0.118$  must be determined from the experiment.

The fact that strength of QCD grows with distance causes that only color neutral objects (hadrons) are stable. Observation of individual quarks is impossible. This phenomenon is known as confinement [5].

### 2.2.1 Space Time Picture of Interaction

Although the perturbative QCD (p-QCD) is unable to describe whole process of interaction (due to presence of soft physic at least when partons are hadronised to color singlet objects), there still exists a class of "hard" collisions where QCD has a predictive power.

The general interaction of hadrons, leptons or gauge bosons  $A, B$

$$A + B \rightarrow F \quad (2.20)$$

could be factorised to tree steps (see Fig. 2.5) [6].

#### The initial evolution

is represented by the distribution functions  $D_{a/A}(x_1, M_1)$  and  $D_{b/B}(x_2, M_2)$  which can be interpreted as the probability density of finding parton  $a$  ( $b$ ) with longitudinal momentum fraction  $x_1$  ( $x_2$ ) in the hadron  $A$  ( $B$ ). The factorisation scales are denoted as  $M_1$  and  $M_2$ . These densities are determined by interaction at large distances and thus are incalculable within p-QCD.

#### The hard scattering of partons

$$a + b \rightarrow c + d \quad (2.21)$$

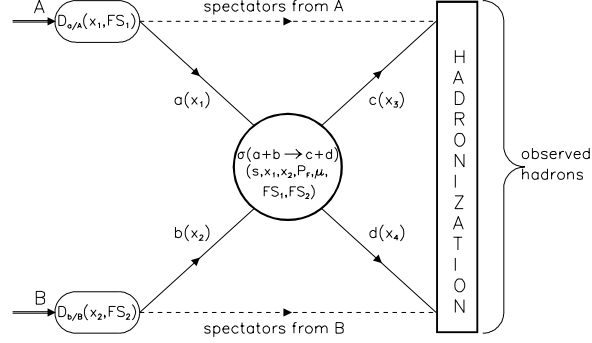


Fig. 2.5: General schema of QCD improved parton model.

where the partonic cross section  $\sigma_{ab \rightarrow cd}$  could be calculated by p-QCD

$$\sigma_{ab \rightarrow cd}(s, x_1, x_2, p_c, p_d, \mu, M_1, M_2). \quad (2.22)$$

The resulting cross section depends in addition on previously defined variables  $x_1$  and  $x_2$ ,  $M_1$  and  $M_2$ , on the CMS energy of collision  $s = (p_A + p_B)^2$ , four-momenta of outgoing partons  $p_c$ ,  $p_d$  and renormalization scale  $\mu$  which describes the "hardness" of the process.

### Hadronization

The existence of color charge objects (partons) at large distance is not possible as well as using of p-QCD. New quark-anti-quark pairs are created to make the outgoing objects color neutral to ensure confinement. First models of hadronization were based on the fragmentation functions  $D_{h/p}(z, p_T^2)$  which describe probability density of finding hadron  $h$  with longitudinal momentum fraction  $z$  and the transverse momentum  $p_T$  with respect to the initial parton  $p$ . In this approach is fragmentation of each parton considered to be independent on the other ones. At the present time Monte Carlo (MC) generators allow to use more complex models of hadronization.

In all steps the same renormalization scheme ( $\overline{\text{MS}}$  or DIS) must be used. Cross section of the interaction  $A + B \rightarrow F$  is then

$$\begin{aligned} \sigma(A + B \rightarrow F) &= \sum_{abcd} \int \int dx_1 dx_2 D_{a/A}(x_1, M_1) D_{b/B}(x_2, M_2) \\ &\quad \sigma_{ab \rightarrow cd}(s, x_1, x_2, p_c, p_d, \mu, M_1, M_2) \otimes D_{hadr}(p_c, p_d, P_F), \end{aligned} \quad (2.23)$$

where  $D_{hadr}$  is model-dependent term which describes hadronization.

The final cross section depends on values of factorisation and renormalization scales and on factorisation scheme used. This unphysical dependence theoretically vanishes if the perturbative series is summed to all orders (see for example Figs. 2.6 and 2.7).

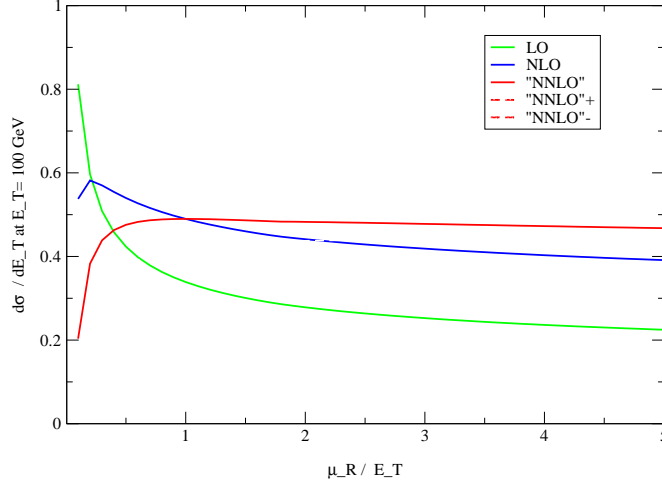


Fig. 2.6: Scale dependence of inclusive single differential jet cross section  $d\sigma/dE_T|_{E_T=100 \text{ GeV}}$  in  $\bar{p}p$  interactions for  $\sqrt{s} = 1.8 \text{ TeV}$  ( $0.1 < |\eta| < 0.7$ ) [7].

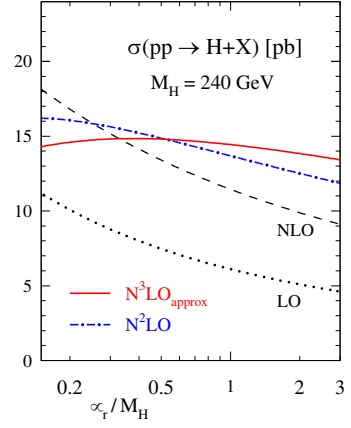


Fig. 2.7: Scale dependence of the cross section of Higgs boson production in  $pp$  interactions [8].

### 2.2.2 Parton Distribution Functions

Parton distribution functions (PDFs) describe the probability density of finding a parton with momentum fraction  $x$  inside a hadron. There exists PDF for each quark and anti-quark flavour and for gluon; together  $2N_f + 1$  functions ( $N_f$  is number of active quark flavours).

Parton model predicts independence of PDFs on the scale. Indeed small logarithmic dependence exists (see Fig. 2.8) which disappears only for  $x \sim 1/6$ . Although it is impossible to estimate PDFs from first principles, QCD fully describes the dependence of parton distribution functions on the scale. If the quark and gluon densities  $f_i(x, M_0)$  are known at some initial scale  $M_0$  for interval  $x \in (x_0, 1)$  then DGLAP evolution equations [9] provide PDFs at arbitrary scale  $M$

$$\frac{df_i(x, M)}{d \ln M^2} = \sum_j \int_x^1 \frac{dy}{y} P_{ij}^{(n)}\left(\frac{x}{y}, M\right) f_j(y, M). \quad (2.24)$$

## H1 and ZEUS

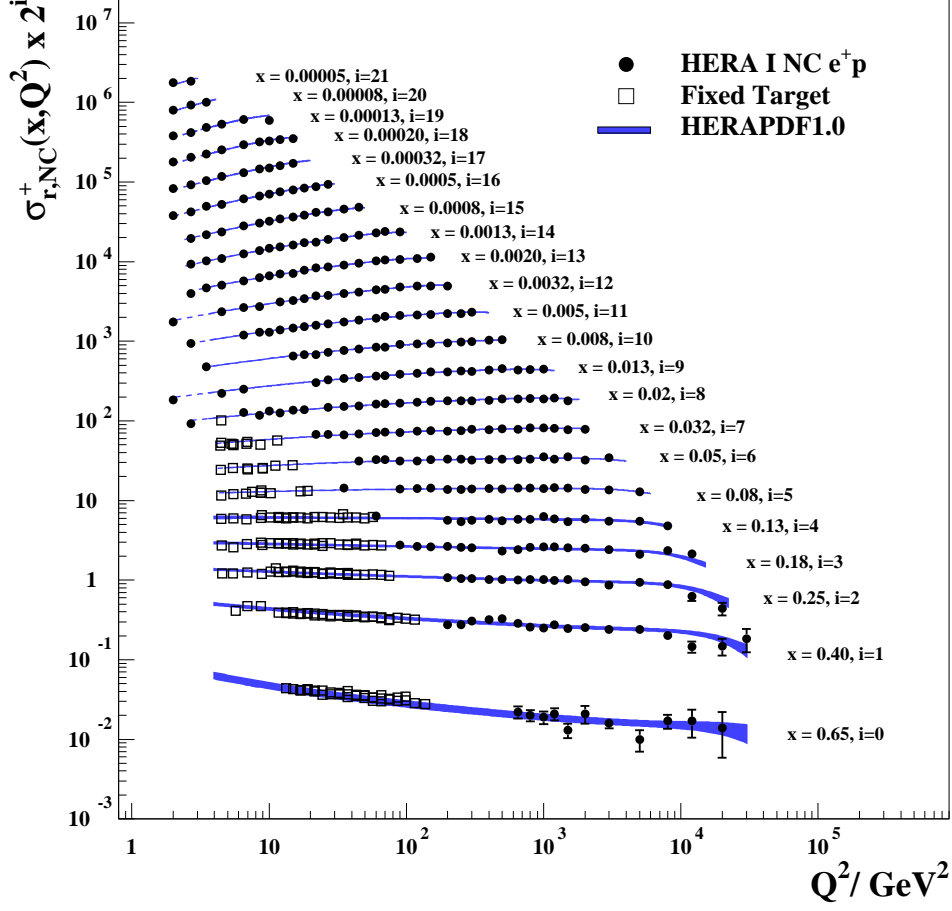


Fig. 2.8: DIS reduced cross section  $\sigma_r \simeq F_2$  as a function of  $Q^2$  for several  $x$  values as measured by HERA in 2010 [4].

$$\begin{array}{cccc}
P_{qq}^{(0)}(x/\xi, M) & P_{qG}^{(0)}(x/\xi, M) & P_{Gq}^{(0)}(x/\xi, M) & P_{GG}^{(0)}(x/\xi, M) \quad (2.26) \\
\begin{array}{c} \text{Diagram 1: } b \xrightarrow{\xi} \text{ vertex } \rightarrow \begin{array}{l} \nearrow a \\ \searrow \text{gluon} \end{array} \end{array} & \begin{array}{c} \text{Diagram 2: } g \xrightarrow{\xi} \text{ vertex } \rightarrow \begin{array}{l} \nearrow a \\ \searrow \text{quark} \end{array} \end{array} & \begin{array}{c} \text{Diagram 3: } b \xrightarrow{\xi} \text{ vertex } \rightarrow \begin{array}{l} \nearrow \text{gluon} \\ \searrow \text{quark} \end{array} \end{array} & \begin{array}{c} \text{Diagram 4: } g \xrightarrow{\xi} \text{ vertex } \rightarrow \begin{array}{l} \nearrow \text{gluon} \\ \searrow \text{gluon} \end{array} \end{array}
\end{array}$$

Fig. 2.9: Feynman diagrams of QCD splitting functions in the leading order, for analytic expressions see [10].

The indexes  $i$  and  $j$  run over all quarks and anti-quark flavours and gluon. The partonic splitting functions  $P^{(n)}$  can be derived from p-QCD at arbitrary order. In the leading order (LO) are non zero only

$$P_{q_i q_i}^{(0)}, P_{q_i g}^{(0)}, P_{g q_i}^{(0)}, P_{g g}^{(0)}, P_{\bar{q}_i \bar{q}_i}^{(0)}, P_{\bar{q}_i g}^{(0)}, P_{g \bar{q}_i}^{(0)} \quad (2.25)$$

splitting functions which are factorisation scheme independent (see Fig. 2.9).

To make next to leading order (NLO) evolution which is widely used nowadays, one must use splitting functions  $P^{(1)}$  depending on factorisation scale and factorisation scheme. In addition to leading order the splitting functions between different flavours  $P_{q_i q_j}^{(1)}$ ,  $P_{q_i \bar{q}_j}^{(1)}$  and  $P_{\bar{q}_i q_j}^{(1)}$  are non-zero. Explicit form of NLO evolution equations and splitting functions can be found in [10].

### 2.2.3 QCD Matrix Element

The second part of formula (2.23) is the matrix element. It must be of the same order as PDFs and in the same factorisation scheme as well.

In perturbative calculations ultraviolet, collinear and soft divergences occur. The first ones are absorbed to new defined renormalized quantities like coupling constant or wave functions. Infrared divergences disappear with proper definition of initial and final state according to Kinoshita-Lee-Nauenberg theorem [11]. Definition must reflect for instance inability to distinguish emission of soft gluon with energy below some threshold (energy resolution of the detector) from no gluon emission or emission of nearly collinear gluon from quark from no emission (emission below angle resolution). Next reason why it is not possible to distinguish between "close" partons is the hadronization effect. In simulations is this ambiguity removed by means of the jet algorithms (see section 2.2.4) with merge neighbouring partons into one object – jet.

As an example of this procedure Feynman diagrams for  $\gamma^* q$  are depicted in Fig 2.10, where (b) and (c) configurations have collinear and soft singularities if the

gluon is emitted close to quark. These infinities disappear by adding of negative infinity from the interference term.

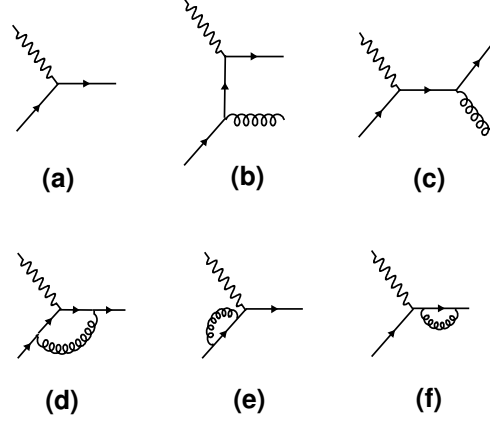


Fig. 2.10:  $\gamma^*q$  interactions. (a) Zero order parton model  $\gamma^*$  absorption, (b,c) LO QCD Compton process in  $t$  and  $s$  channel. Diagrams (d,e,f) in combination with  $(a) - 2 \text{Re}[(d+e+f) \times (a)]$  represent LO contribution which removes infrared gluon singularities of (b,c).

#### 2.2.4 Hadronization

Various models exist to describe the transition from partons to hadrons. The most common are the Lund string model implemented in PYTHIA [12] and RAPGAP [13] and the cluster model in HERWIG [14] MC generators.

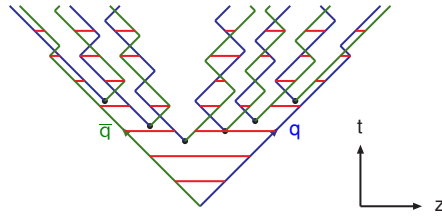


Fig. 2.11: Simplified picture of hadron production from  $q - \bar{q}$  pair flying in opposite directions with respect to  $z$  axis.

The string model of hadronization can be described in the following way. The potential between quarks is known to grow linearly from some distance which is



modeled by a color string. If the quarks are moving apart the string is stretching and if its length exceeds some limit, the string breaks. At the ends of this break point new quark and anti-quark are created and so on as long as the quarks have enough energy to break the string (see Fig. 2.11).

### Jet Algorithm

The observation of the jets provides a view of the underlying hard quark and gluon interactions that occur at very small distance scales. However, this view is inevitably clouded by the subsequent long distance showering and eventual hadronization of the primary quarks and gluons. Furthermore, since the quarks and gluons carry non-zero color charges and the final hadrons do not, there can be no unique association of a jet of hadrons with a particular quark or gluon. Nevertheless, with a suitable definition of the jet cross section (by means of suitable jet algorithm) one hopes to minimize the effect of long distance physics and of the inherent jet ambiguities and obtain a fairly precise picture of the short distance dynamics.

In this thesis the inclusive  $k_T$  jet algorithm [15, 16] is used which fulfils all necessary conditions like infrared and collinear safety,  $z$ -boost invariance, good correspondence between different levels (hadron, parton, detector) and small dependence on hadronization model. Roughly saying this algorithm merges particles which are close in  $(\eta, \phi)$  plane into jets.

Inclusive  $k_T$  algorithm works with proto-jets here denoted with indexes  $i, j, k, l, m$  which are on the beginning identical with the particles. The procedure is following:

1. Define a distances

$$D_{ij} = \frac{(\eta_j - \eta_i)^2 + (\phi_j - \phi_i)^2}{R^2} \min(P_{Ti}^2, P_{Tj}^2) \quad D_i = P_{Ti}^2 \quad (2.27)$$

2. Find the smallest value from each pair  $D_{ij}$  ( $i \neq j$ ) and each  $D_i$ .

- If this value is  $D_{kl}$  then merge jets  $k$  and  $l$  into jet  $m$ .

$$P_{T,m} = P_{T,k} + P_{T,l} \quad (2.28)$$

$$\eta_m = \frac{P_{T,k}\eta_k + P_{T,l}\eta_l}{P_{T,m}} \quad (2.29)$$

$$\phi_m = \frac{P_{T,k}\phi_k + P_{T,l}\phi_l}{P_{T,m}} \quad (2.30)$$

- If the smallest value is  $D_k$  then the corresponding proto-jet  $k$  turns into jet and is removed from the proto-jet list.

3. Go to step 1 until any proto-jet remains.

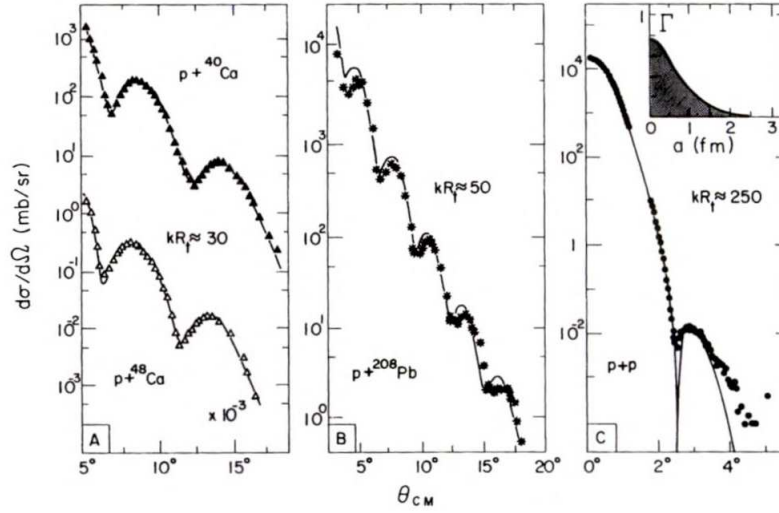


Fig. 2.12: Differential cross section as a function of scattered angle for interaction of proton with atom or proton [17].

## 2.3 Diffraction

The diffraction of light in optics is known from 17th century. For diffraction is typical a pattern of diffractive maxima and minima behind the obstacle. In twentieth century similar behavior was observed for X-rays and electrons. It was found that even larger objects like protons can have wave-like behavior (see Fig. 2.12). Positions of diffractive minima provide information about size of the obstacle, for smaller objects are the minima farther one of each other. Intensities of minima depend on the shape and oscillations of the obstacle. The Fig. 2.12 shows that even in particle physics (here  $pp$ ) diffraction occurs.

Diffraction in particle physics can be defined in the following alternative ways [18].

1. A reaction in which no quantum numbers are exchanged between the colliding particles is, at high energies, a diffractive reaction.
2. A diffractive reaction is characterized by a large, non exponentially suppressed rapidity gap in the final state.

In both definitions the contamination from non-diffractive events exists. In the first case the contamination disappears in the high energy limit with respect to the particle masses. In the second case the distribution of diffractive events with respect

to rapidity gap  $\Delta\eta$  is constant

$$\frac{dN_{diff}}{d\Delta\eta} \sim \text{constant} \quad (2.31)$$

while the non-diffractive background is exponentially suppressed

$$\frac{dN_{non-diff}}{d\Delta\eta} \sim e^{-\Delta\eta}. \quad (2.32)$$

The bridge between these two definitions provides Regge model [19] which describes diffractive scattering as a consequence of exchange of a colorless object with vacuum quantum numbers – the pomeron.

The colliding particles in diffraction need not to be the same as the final particles. One or both particles can dissociate into the system  $X$  with the same quantum numbers as incoming particles

$$1 + 2 \rightarrow 1' + 2' \quad 1 + 2 \rightarrow 1' + X_2 \quad 1 + 2 \rightarrow X_1 + X_2. \quad (2.33)$$

Soft diffraction without any hard scale cannot be described by perturbative quantum chromodynamics.

Renewed interest in diffraction was risen with the observation of the diffractive production of "hard" jets in  $p\bar{p}$  collisions at UA8 experiment at CERN in 1988 [20]. Existence of such a class of events was theoretically predicted by Ingelman and Schlein [21] in 1985 and is often referred as a hard diffraction.

In 1993 were in  $ep$  interaction in DIS at HERA [22] observed events with a large gap in pseudorapidity between the scattered proton  $p'$  and other final state hadrons. So the process ( $\gamma^*$  is a virtual photon "emitted" from the electron)

$$\gamma^* + p \rightarrow X + p'(Y) \quad (2.34)$$

is according to the second definition diffractive. The virtual photon is dissociated to the hadronic system  $X$  with the same quantum numbers as photon while the beam proton usually stays intact or dissociates to low mass hadronic system  $Y$ .

As well as in  $p\bar{p}$  collision was the hard scale provided by transverse energy of the jets, in  $ep$  collision it is a photon virtuality  $Q^2$  for inclusive diffractive DIS or the function of transverse jet energy and  $Q^2$  for dijet production in DIS. The hard diffraction can be then described within the framework of p-QCD.

### 2.3.1 Kinematics

#### Inclusive Diffraction

To describe inclusive diffractive process  $2 \rightarrow 3$  of unpolarized particles (see Fig. 2.13)

$$e(k) + p(P) \rightarrow e(k') + X(P_X) + Y(P_Y) \quad (2.35)$$

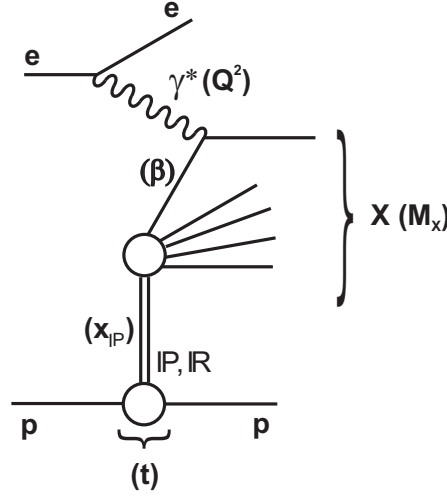


Fig. 2.13: Leading order diagram of inclusive diffractive process. States  $X$  and  $Y$  are separated by large gap in rapidity.

four independent variables are needed. We suppose that system  $Y$  is either proton or low mass hadronic state with mass  $M_Y \leq M_Y^{\max}$  where the limit mass  $M_Y^{\max}$  is usually done by the detector properties. In addition to the DIS variables (see section 2.1.1) we define (symbol  $\simeq$  means neglecting of  $t$  and mass  $M_Y$ ):

- Longitudinal momentum fraction carried by the diffractive exchange

$$x_{IP} = \frac{q(P - P_Y)}{qP} \simeq \frac{M_X^2 + Q^2}{W^2 + Q^2}. \quad (2.36)$$

- Momentum fraction of the stuck parton with respect to diffractive exchange

$$\beta = \frac{Q^2}{q(P - P_Y)} \simeq \frac{Q^2}{M_X^2 + Q^2}. \quad (2.37)$$

- Momentum transfer at the proton vertex

$$t = (P - P_Y)^2. \quad (2.38)$$

For  $x$  variable then holds the relation  $x = \beta x_{IP}$ . Variables  $x_{IP}$  and  $\beta$  are by virtue of their definition dimensionless and have the values between 0 and 1.

Widely used set of variables for description of inclusive diffractive DIS is  $(\beta, Q^2, x_{IP}, t)$  or  $(x, Q^2, x_{IP}, t)$ .

### Diffractive Dijet Production

In more exclusive diffractive process

$$e + p \rightarrow e + \underbrace{jj + X'}_X + Y, \quad (2.39)$$

where  $jj$  denotes system of two jets, additional kinematic variables are needed. Leading order diagrams of diffractive dijet production are shown in figure 2.14. In DIS regime ( $Q^2 \gg 0$ ) is contribution from diagram (b) negligible whereas in photoproduction ( $Q^2 \sim 0$ ) must be both diagrams taken into account. The four-momenta of partons entering the hard subprocess from photon and pomeron side are denoted as  $u$  and  $v$ . In case of (a) is  $u$  identical with four-momentum  $q$  of the virtual photon.

We define the invariant mass of dijet system  $M_{12}$  as

$$M_{12} = \sqrt{(u + v)^2} \quad (2.40)$$

and longitudinal fraction of pomeron (photon) four-momentum  $z_{IP}$  ( $x_\gamma$ ) entering to the hard subprocess

$$z_{IP} = \frac{qv}{q(P - P_Y)} \quad x_\gamma = \frac{Pu}{Pq}. \quad (2.41)$$

Variable  $x_\gamma$  is for diagram (a) where  $u = q$  identically equal to one whilst for (b) it has values between 0 and 1. Due to this feature  $x_\gamma$  is usually used in experiments as a discriminator between direct (a) and resolved (b) photoproduction.

### 2.3.2 Regge Phenomenology of Diffraction

Regge phenomenology [19] originates from studying of analytical properties of scattering amplitude  $A(s, t)$ <sup>2</sup> of process  $2 \rightarrow 2$ . It was realised that in Regge limit ( $s \gg |t|$ ) dominant behaviour of amplitude is

$$A(s, t) \sim s^{\alpha(t)}. \quad (2.42)$$

This expression follows from partial wave expansion of  $A(s, t)$  in the  $t$  channel. The relativistic partial wave amplitude  $A_l(t)$  can be analytically extended to complex  $l$  values in a unique way. The position of the pole in  $l$  plane with the highest real part is denoted as  $\alpha(t)$ .

---

<sup>2</sup> $s$ ,  $t$  and  $u$  are so called Mandelstam variables of process  $a + b \rightarrow c + d$  with corresponding four-momenta  $p_a, p_b, p_c, p_d$ . Mandelstam variables are defined as  $s = (p_a + p_b)^2$ ,  $t = (p_a - p_c)^2$  and  $u = (p_a - p_d)^2$ .

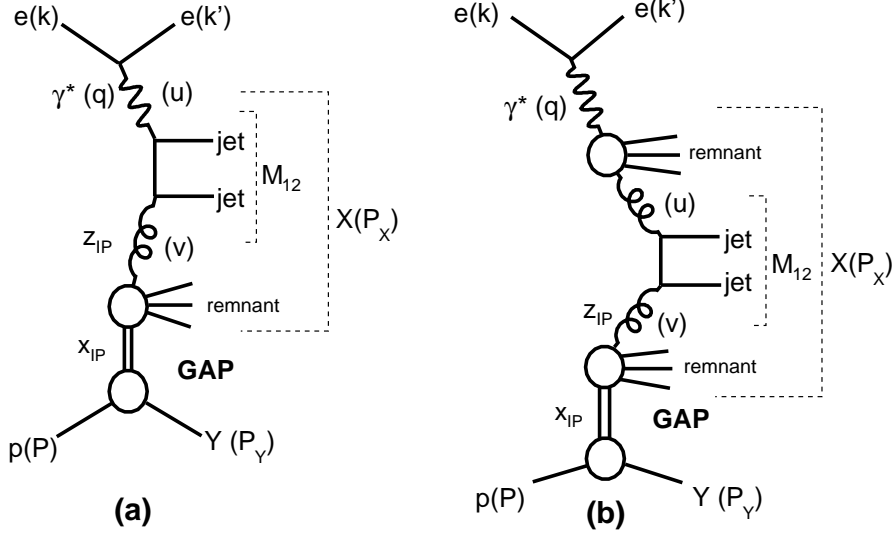


Fig. 2.14: Leading order diagrams of direct (a) and resolved (b) diffractive dijet production.

This leading singularity relates to the exchanging particles (resonances) which can be plotted on Chew-Frautschi graph ( $J = \alpha(t)$  vs.  $M^2 = |t|$ ). The mesonic trajectory (see Fig. 2.15) seems to be linear

$$\alpha(t) = \alpha(0) + \alpha' t \quad (2.43)$$

with  $\alpha(0) \simeq 0.5$  and slope  $\alpha' \simeq 1 \text{ GeV}^{-2}$ .

Total cross section can be obtained from scattering amplitude (2.42) with help of optical theorem

$$\sigma_{tot} \sim s^{\alpha(0)-1}. \quad (2.44)$$

If one interprets  $pp$  interaction as a consequence of exchange of the mesonic trajectory (exchange of reggeon) then  $\sigma_{tot} \sim s^{-1/2}$ . In reality growing of total cross section is observed for high energies (see Fig. 2.16) in  $pp(\bar{p})$ ,  $pn(\bar{n})$ ,  $\pi^\pm p$ ,  $\gamma p$  interactions which yields to introduction of the pomeron trajectory  $\alpha_{IP}(t)$  with  $\alpha(0) > 1$ .

Total cross section is then fitted by formula

$$\sigma_{tot} = A_{IP} s^{\alpha_{IP}(0)-1} + A_{IR} s^{\alpha_{IR}(0)-1}. \quad (2.45)$$

In contrast to reggeon trajectory  $\alpha_{IR}(t)$  no real particle was discovered at the pomeron line. Therefore pomeron is interpreted as a hypothetical object with vacuum quantum numbers.

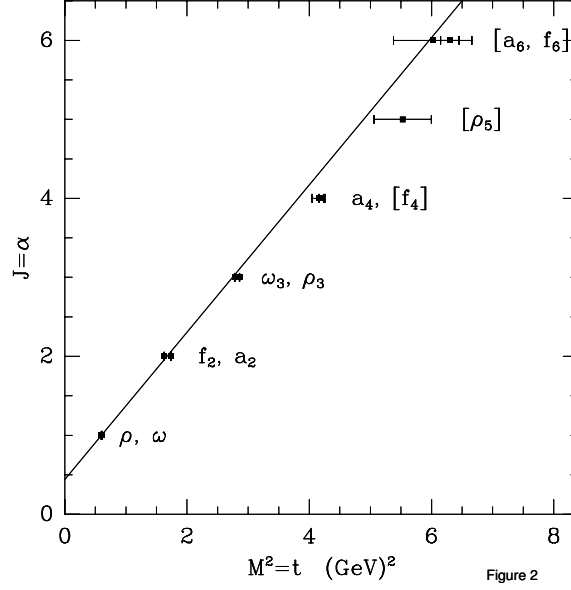


Fig. 2.15: The leading mesonic trajectory – dependence of spin of the mesons on square of their mass [23].

Diffractive  $ep$  interactions are well described by parametrization based on exchange of pomeron and reggeon. Reggeon trajectory is not negligible only in region  $x_{IP} \gtrsim 0.01$  and for  $x_{IP} = 0.01$  is its contribution around 10 % [24].

### 2.3.3 Factorisation in Inclusive Diffractive DIS

Cross section of inclusive diffractive DIS can be written in the similar way like in DIS (2.14)

$$\frac{d^4\sigma}{dx dQ^2 dx_{IP} dt} = \frac{4\pi\alpha_{em}^2}{xQ^4} \left(1 - y + \frac{1}{2}y^2\right) \sigma_r^{D(4)}(x, Q^2, x_{IP}, t). \quad (2.46)$$

Reduced diffractive cross section  $\sigma_r^{D(4)}$  is expressed by diffractive structure functions

$$\sigma_r^{D(4)} = F_2^{D(4)} - \frac{y^2}{1 + (1 - y)^2} F_L^{D(4)}, \quad (2.47)$$

where longitudinal structure function  $F_L^{D(4)}$ , which relates to the scattering of photons with longitudinal polarisation, can be usually neglected except of region with high  $y$ .

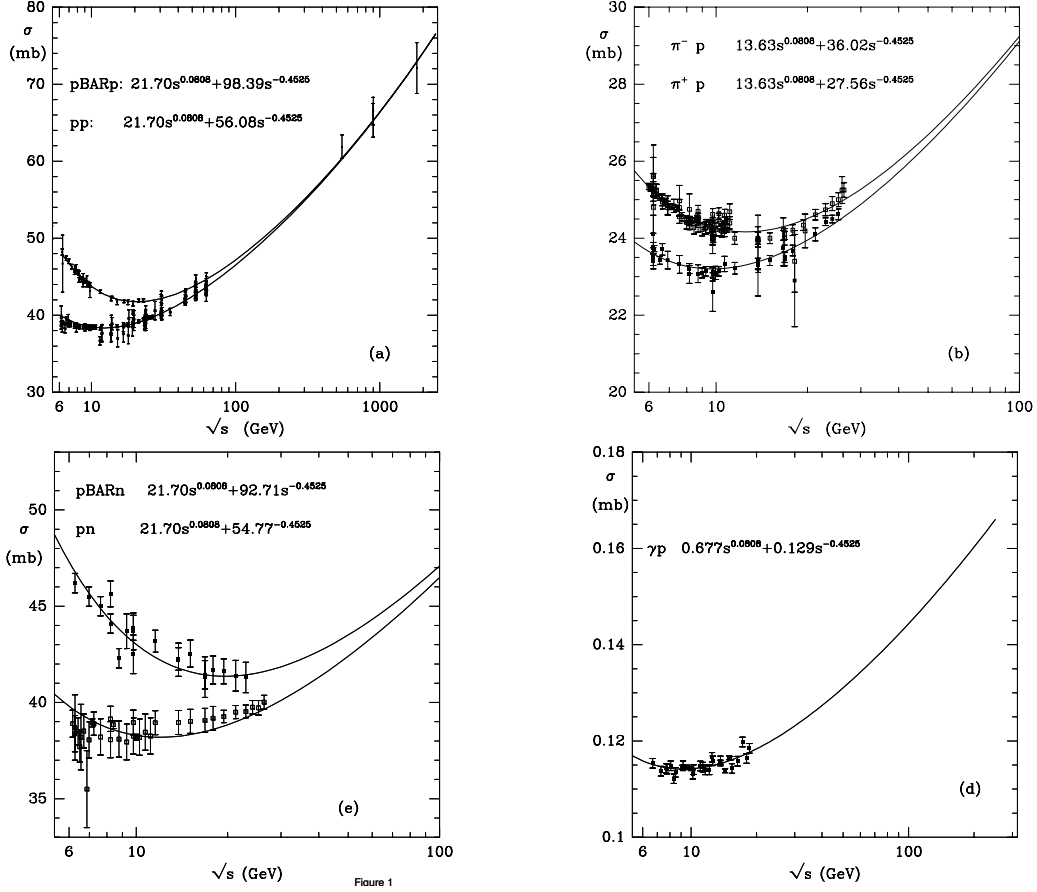


Fig. 2.16: Total cross sections for  $pp$ ,  $\pi p$ ,  $pn$  and  $\gamma p$ . All cross sections are fitted by formula  $As^{0.08} + Bs^{-0.45}$  where  $A$  is the same for particle and anti-particle [23].

It has been proven in p-QCD [25] that like in inclusive DIS scattering, a factorisation theorem holds for diffractive DIS processes. Therefore the diffractive structure functions  $F_{2,L}^D$  can be written by means of diffractive parton distribution functions  $f_i^D$  which represent the probability to find a parton  $i$  in a hadron under the condition that the hadron undergoes diffractive scattering

$$F_{2,L}^{D(4)}(x, Q^2, x_{IP}, t) = \sum_i \int_x^{x_{IP}} d\xi f_i^D(\xi, \mu^2, x_{IP}, t) \hat{F}_{2,L}^i\left(\frac{x}{\xi}, Q^2, \mu^2\right). \quad (2.48)$$

The perturbatively calculable coefficients  $\hat{F}_{2,L}^i$  are so called coefficient functions which are the same as in non-diffractive DIS [26]. At the lowest order they are



expressed as

$$\hat{F}_2^q(z, Q^2, \mu^2) = e_q^2 \delta(1 - z) \quad \hat{F}_2^g(z, Q^2, \mu^2) = 0 \quad \hat{F}_L^i(z, Q^2, \mu^2) = 0. \quad (2.49)$$

Formulas (2.48) allow to calculate  $\sigma_r^{D(4)}$  from diffractive parton distribution functions (DPDFs). These DPDFs obey the same DGLAP evolution equations as non-diffractive PDFs

$$\frac{d}{d \ln \mu^2} f_i^D(x, \mu^2, x_{IP}, t) = \sum_j \int_x^1 \frac{d\xi}{\xi} P_{ij}^{(n)}\left(\frac{x}{\xi}, \alpha_s(\mu)\right) f_j^D(\xi, \mu^2, x_{IP}, t) \quad (2.50)$$

where  $P_{ij}^{(n)}$  is a splitting function between parton  $i$  and  $j$  in order  $n + 1$  of  $\alpha_s$ .

Unphysical factorisation scale ( $\mu^2$ ) dependence in (2.48) is cancelled in each order of  $\alpha_s$ . The structure functions  $F_{2,L}^{D(4)}$  are in reality  $\mu^2$  dependent because the coefficient functions are known only in finite order as well as DGLAP evolution of DPDFs,.

Factorisation theorem can be written in more general way as a convolution of DPDFs with the elementary partonic cross section  $\hat{\sigma}$  (for comparison see 2.23)

$$d\sigma^{\gamma^* p \rightarrow Xp}(x, Q^2, x_{IP}, t) = \sum_i f_i^D(x, Q^2, x_{IP}, t) \otimes d\hat{\sigma}_{\gamma^* i}(x, Q^2). \quad (2.51)$$

### 2.3.4 Regge Factorisation of DPDFs

Regge theory which describes diffraction as a consequence of pomeron and sub-leading reggeon exchange makes an extra assumption for DPDFs

$$f_i^D(x, Q^2, x_{IP}, t) = f_{IP/p}(x_{IP}, t) f_{i/IP}(\beta = x/x_{IP}, Q^2) + n_{IR} f_{IR/p}(x_{IR}, t) f_{i/IR}(\beta = x/x_{IP}, Q^2). \quad (2.52)$$

Probability of finding parton  $i$  inside proton  $p$  is factorised as a product of pomeron flux  $f_{IP/p}$  (probability of finding pomeron inside proton) and parton densities of pomeron  $f_{i/IP}$ . The reggeon contribution is added in the same way with the scale factor  $n_{IR}$ .

Pomeron and reggeon fluxes are usually parametrized as

$$f_{IP/p}(x_{IP}, t) = A_{IP} \frac{e^{B_{IP}t}}{x_{IP}^{2\alpha_{IP}(t)-1}} \quad f_{IR/p}(x_{IP}, t) = A_{IR} \frac{e^{B_{IR}t}}{x_{IP}^{2\alpha_{IR}(t)-1}} \quad (2.53)$$

with linear pomeron  $\alpha_{IP}(t)$  and reggeon  $\alpha_{IR}(t)$  trajectories (2.43). Coefficients  $A$ ,  $B$ ,  $\alpha(0)$  and  $\alpha'$  for both trajectories are obtained from the experiment.

### 2.3.5 Factorisation in Diffractive Dijet Photoproduction

Contrary to inclusive diffractive DIS where the photon acts as a small distance probe of pomeron structure, in diffractive photoproduction is rather the structure of the photon tested. The factorisation theorem was not proved for diffractive dijet photoproduction and there are theoretical indications that the factorisation is here broken [27].

There exist two kinds of photoproduction processes (see Fig. 2.14) the direct, where photon enters with all its momentum to the hard subprocess and resolved where photon dissociates into a hadronic system which is a source of quarks and gluons. The partonic structure of the photon is described by  $\gamma$ -PDFs  $f_{j/\gamma}$  which are of order  $\frac{\alpha_{em}}{\alpha_s}$  [28]. The physical meaning has only the sum of direct and resolved contributions.

The factorisation formulas for resolved (*res*) and direct (*dir*) photoproduction have the following form

$$d\sigma^{res}(ep \rightarrow e + 2\text{jets} + X + Y) = \sum_{i,j} \int dy f_{\gamma/e}(y) \int dx_\gamma f_{j/\gamma}(x_\gamma, \mu_F^2) \otimes \int dt \int dx_{IP} \int dz_{IP} d\hat{\sigma}(ij \rightarrow 2\text{jets}) f_i^D(z_{IP}, \mu_F^2, x_{IP}, t), \quad (2.54)$$

$$d\sigma^{dir}(ep \rightarrow e + 2\text{jets} + X + Y) = \sum_i \int dy f_{\gamma/e}(y) \otimes \int dt \int dx_{IP} \int dz_{IP} d\hat{\sigma}(\gamma i \rightarrow 2\text{jets}) f_i^D(z_{IP}, \mu_F^2, x_{IP}, t), \quad (2.55)$$

where  $f_{\gamma/e}$  is the equivalent photon flux done by Weizsäcker-Williams formula [29, 30]

$$f_{\gamma/e}(y) = \frac{\alpha_{em}}{2\pi} \left[ \frac{1 + (1-y)^2}{y} \ln \frac{Q_{max}^2}{Q_{min}^2} - 2m_e^2 y \left( \frac{1}{Q_{min}^2} - \frac{1}{Q_{max}^2} \right) \right]. \quad (2.56)$$

In the photoproduction is  $Q_{min}^2$  lowest kinetically allowed value  $Q_{min}^2 = \frac{m_e^2 y^2}{1-y}$  and  $Q_{max}^2$  is determined from the  $Q^2$  cut of the measurement.

DPDFs can be for small  $x_{IP}$  (where reggeon term is negligible) written as a product of "integrated" pomeron flux<sup>3</sup> and pomeron PDF (2.52). Factorisation formula for the resolved part has then same form from photon and pomeron side with clear physical meaning. Formula for direct cross section is obtained by setting

---

<sup>3</sup>In the diffractive measurement using large rapidity gap method to identify of diffractive events, the momentum transfer  $t$  cannot be measured, there exists only the upper limit of  $|t|$ . The lower limit of  $|t|$  is kinematically restricted to  $|t| = \frac{M_P^2 x_{IP}^2}{1-x_{IP}}$ . The formula is then integrated over  $t$  within this range.

$$f_{j/\gamma} = \delta(1 - x_\gamma)$$

$$\begin{aligned} d\sigma^{res}(ep \rightarrow e + 2\text{jets} + X + Y) = \sum_{i,j} \int dy \int dx_\gamma f_{\gamma/e}(y) f_{j/\gamma}(x_\gamma, \mu_F^2) \otimes \\ \int dx_{IP} \int dz_{IP} d\hat{\sigma}(ij \rightarrow 2\text{jets}) f_{i/IP}(z_{IP}, \mu_F^2) f_{IP/p}(x_{IP}). \end{aligned} \quad (2.57)$$

The matrix element is in the LO (NLO) approach of order<sup>4</sup>  $\alpha_{em}\alpha_s$  ( $\alpha_{em}\alpha_s^2$ ) for direct photoproduction and  $\alpha_s^2$  ( $\alpha_s^3$ ) for resolved photoproduction. The number of produced partons (jets) within the NLO (LO) matrix element in direct or resolved photoproduction is therefore maximally 3 (2) [31].

### 2.3.6 Methods of Detection of Diffractive Events

#### Large Rapidity Gap

In a typical inclusive DIS event (see Fig. 2.17) is a beam proton completely destroyed and the rapidity interval between the struck quark and the proton remnant is due to color interaction completely filled by particles created in hadronization process. The hadronic activity in the forward region of the detector is observed.

In the diffractive case (see Fig. 2.17) the leading proton remains nearly intact and is lost in the beam pipe. Because the diffractive exchange pomeron has vacuum quantum numbers, there is no hadronic activity between hadronic system  $X$  and system of the scattered (leading) proton  $Y$ . The gap in pseudorapidity between these two systems is observed. The Fig. 2.18 shows the distribution of the pseudorapidity  $\eta_{max}$  of the most forward hit cluster in ZEUS detector. It can be seen that for low  $\eta_{max}$  values (events with no detected hadronic activity for  $\eta > \eta_{max}$ ) the diffractive contribution, which is not described by non-diffractive MC model, dominates.

With the applying of tight cut on  $\eta_{max}$ , large number events of interests are loosed. This cut i.e. limits the upper  $M_X$  bound. Better way is to detect a rapidity gap in very forward region. The H1 collaboration requires no activity in region  $3.2 < \eta < 7.5$ <sup>5</sup>. This rapidity range is not completely covered with the detectors (see section 3.1.1), so the real gap in pseudorapidity should be smaller. The rapidity gap  $\Delta\eta$  relates to the  $x_{IP}$  variable by formula

$$x_{IP} \simeq e^{-\Delta\eta}. \quad (2.58)$$

Therefore the  $x_{IP}$  reconstructed from the HFS also provides information about rapidity gap. For instance H1 analysis [32] requires  $x_{IP} < 0.03$  which corresponds to  $\Delta\eta \gtrsim 3.5$ .

<sup>4</sup>Note that the  $\gamma$ -PDF are of order  $\frac{\alpha_{em}}{\alpha_s}$ .

<sup>5</sup>The pseudorapidity  $\eta = 7.5$  corresponds to  $t = -1 \text{ GeV}^2$  for HERA proton beam energy.

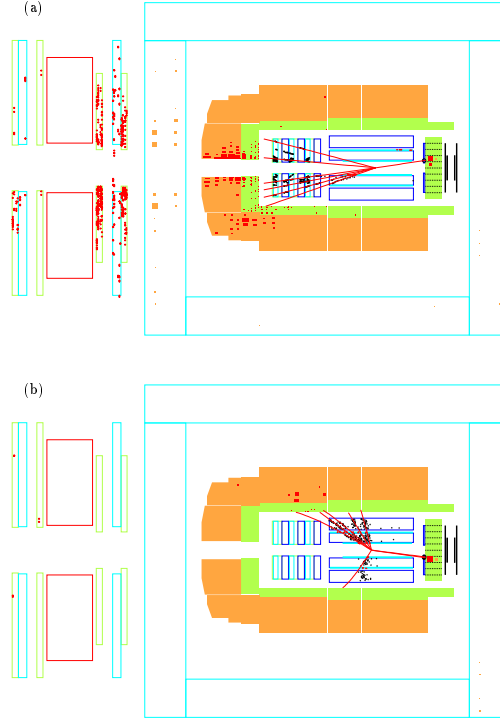


Fig. 2.17: a) "Standard" DIS event, b) event with large rapidity gap (no activity in the forward region of the detector) as seen in H1 detector at HERA.

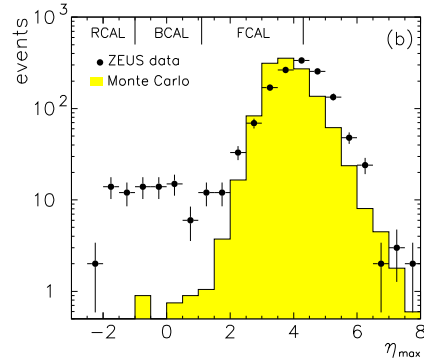


Fig. 2.18: Distribution of  $\eta_{\max}$ , the maximum pseudorapidity of a calorimeter cluster in an event, compared with non-diffractive Monte Carlo [22].

### M-Subtraction

The M-subtraction method is based on the different  $M_X^2$  distribution for diffractive and non-diffractive events

$$\frac{dN_{diff}}{d \ln M_X^2} \sim \frac{1}{M_X^{2\alpha_{IP}(0)-1}} \sim \text{const.} \quad \frac{dN_{non-diff}}{d \ln M_X^2} \sim \exp(a \ln M_X^2) \quad , \text{ with } a > 0. \quad (2.59)$$

The non-diffractive background is therefore for small  $\ln M_X^2$  exponentially suppressed while the diffractive contribution remains constant.

Distributions of the logarithms of the invariant hadronic mass squared as measured at HERA [33] are plotted in Fig. 2.19. It can be seen that the diffractive events selected by large rapidity gap method dominate for small  $M_X$  values.

The diffractive sample is defined by a means of M-subtraction method as the excess of the contribution in the  $\ln M_X^2$  distribution above the exponential fall-off (2.59) of the non-diffractive peak.

This M-subtraction method was used only by ZEUS collaboration.

### Leading-Proton Detection

The diffractive events are characterised by a final state proton scattered at very small angle and with energy nearly to that of the incoming proton. The scattered proton can be detected in the forward proton spectrometers which are positioned very close to the beam pipe approx. 100 m from the interaction point. From the scattered proton energy and the position of the hit cluster in the detector can be estimated  $x_{IP}$  and  $t$  variables.

The measured relative energy spectrum  $x_L = 1 - x_{IP}$  of the scattered proton is shown in Fig. 2.20. It could be seen that in the diffractive peak around  $x_L \sim 1$  the pomeron contribution dominates whilst for smaller  $x_L$  the pion exchange contribution must be take into account.

The main disadvantage of the leading-proton detection method is small geometric acceptance of the forward proton spectrometers – the most part of the scattered protons from the diffractive events is undetected.

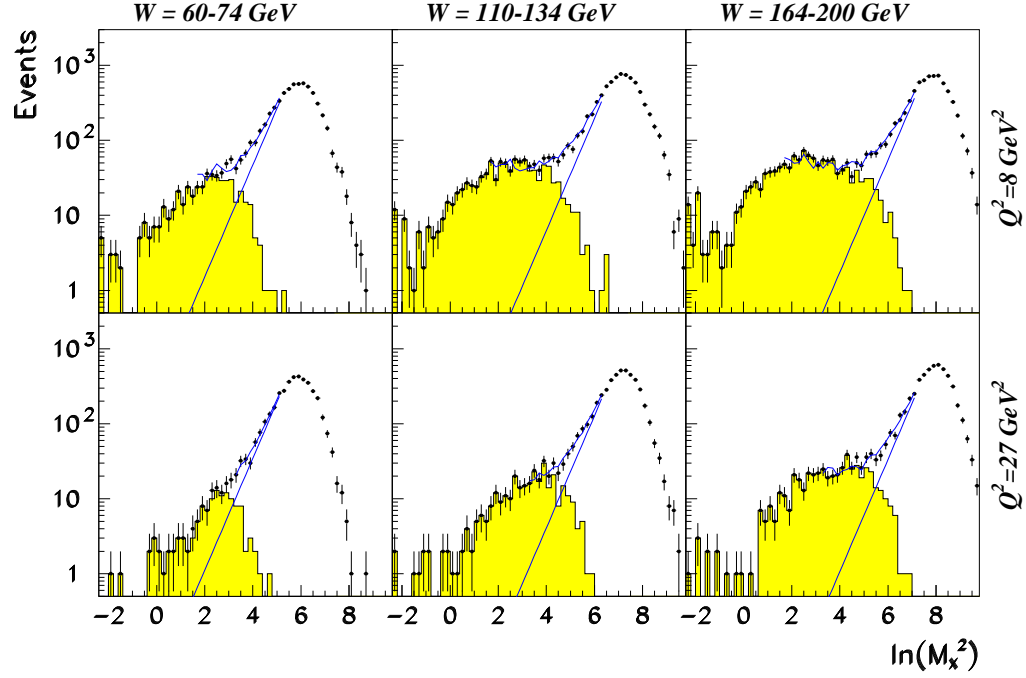


Fig. 2.19: Distribution of  $\ln M_X^2$  (black points) of reaction  $\gamma^*p \rightarrow X + \text{anything}$ , where  $X$  is the system observed in the detector as measured at ZEUS [33]. It was measured for three  $\gamma^*p$  CMS energies and for two photon virtualities. The straightforward blue line gives the non-diffractive contributions as obtained from the fits. The yellow area is the same measurement with additional cut  $\eta_{max} < 1.5$ . It means the events where no particles are detected in the forward region  $\eta > 1.5$  – events with a rapidity gap.

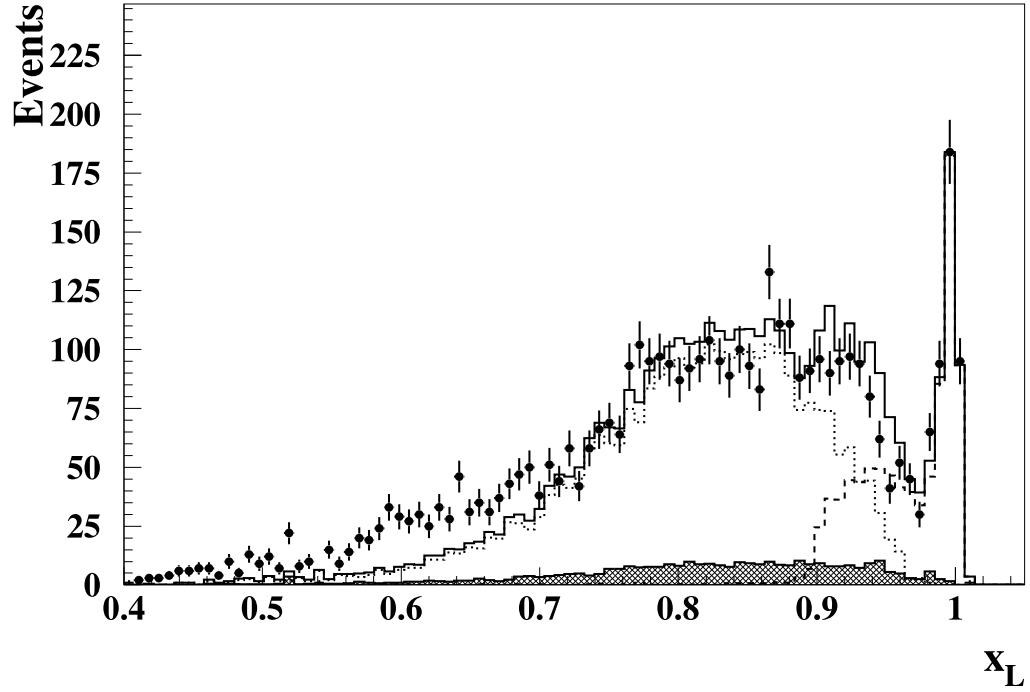


Fig. 2.20: Observed momentum fraction  $x_L = 1 - x_{IP}$  of the leading proton with respect to the beam proton momentum. Note the diffractive peak around  $x_L = 1$ . Diffractive signal modeled by MC is represented by the dashed line. The dotted line is pion-exchange contribution and shaded area corresponds to proton dissociation [34].

## Chapter 3

# Motivation and Recent Results

In this chapter the recent progress in the study of the factorization in diffractive  $ep$  and  $pp$  interactions will be reported.

### 3.1 HERA Collider

The HERA (Hadron-Elektron Ring Anlage) was a particle collider located at DESY (Deutsches Elektron Synchrotron) laboratory in Hamburg. Its circumference is approximately 6.3 km (see Fig. 3.1) and is roughly 20 m under the ground.

After major upgrade in 2004 (HERA II phase) protons with energy 920 GeV were collided with the electrons (positrons) at energy 27.5 GeV. Total collected integrated luminosity is  $400 \text{ pb}^{-1}$  and  $140 \text{ pb}^{-1}$  before the upgrade (1992-2000).

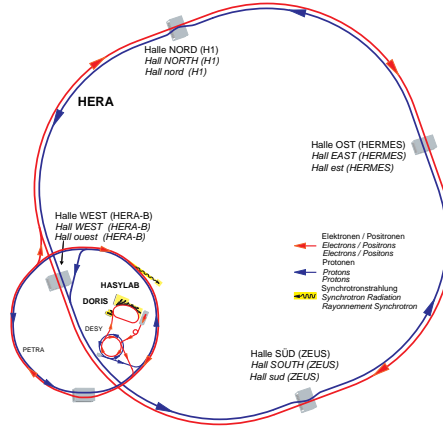


Fig. 3.1: The HERA accelerator with H1 detector in the north and ZEUS detector in the south.



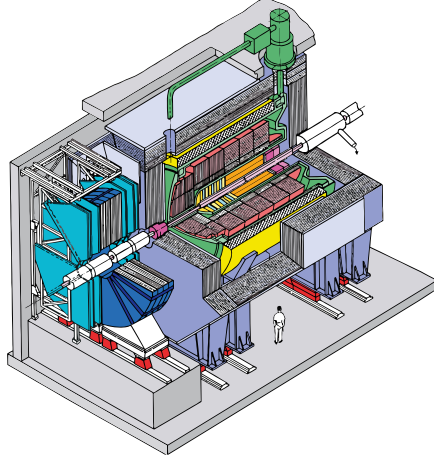


Fig. 3.2: H1 detector

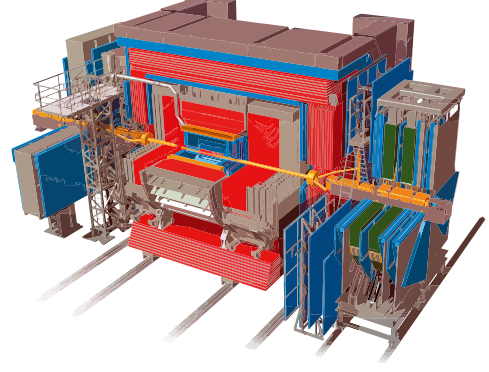


Fig. 3.3: ZEUS detector

The  $ep$  collisions are highly asymmetric, the rapidity of CMS is about 1.75 in the system where the proton beam direction conventionally corresponds to the positive  $z$  axis. Two general purpose detectors H1 and ZEUS must reflect this setup.

### 3.1.1 H1 Detector

The  $ep$  interaction point (the origin of the coordinate system) is surrounded by silicon strip detectors.

Concentric drift chambers in 1.16 T solenoidal magnetic field cover  $-1.5 < \eta < 1.5$  pseudorapidity range and measure charged tracks with accuracy  $\Delta p_T/p_T = 0.005 p_T/\text{GeV}$ .

The liquid argon calorimeter covers range  $-1.5 < \eta < 3.4$  with resolution  $\Delta E/E = 0.11/\sqrt{E/\text{GeV}}$  for electromagnetic showers and  $\Delta E/E = 0.50/\sqrt{E/\text{GeV}}$  for hadrons.

A lead-scintillating fibre calorimeter covers backward region  $-4 < \eta < -1.4$  and its main purpose is detection of scattered electron.

The Forward Muon Detector (FMD) and Proton Remnant Tagger (PRT) covered the forward region  $1.9 < \eta < 3.7$  (or higher due to secondary scattering within the beam pipe) and  $6 < \eta < 7.5$ . These detectors are used to reject events which do not exhibit a rapidity gap between  $Y$  and  $X$  system in LRG method of diffraction detection.

Photoproduction events can be selected by tagging positrons scattered to a very small angles, corresponding to quasi-real photon emission, using a crystal Cerenkov calorimeter at  $z = -33\text{ m}$  (electron tagger).

### 3.1.2 ZEUS Detector

The central tracking detector in magnetic field of 1.43 T covers pseudorapidity region  $-2 < \eta < 2$  and measured resolution is  $\Delta p_T/p_T = 0.006 p_T/\text{GeV}$ .

The uranium-scintillator calorimeter covers region  $-4.3 < \eta < 3.8$  and consists from three parts. The energy resolution for electromagnetic showers was  $\Delta E/E = 0.18/\sqrt{E/\text{GeV}}$  and  $\Delta E/E = 0.35/\sqrt{E/\text{GeV}}$  for hadrons.

Forward plug calorimeter increases forward rapidity coverage to  $\eta \lesssim 5$  and it is used to identify diffractive events by large rapidity gap method.

The luminosity is measured from the rate of QED bremsstrahlung processes  $ep \rightarrow e\gamma p$ . The resulting small-angle photons are detected by the luminosity monitor placed at  $z = -107\text{ m}$ . The similar method was used also by H1 collaboration.

## 3.2 DPDFs from Diffractive Inclusive Data

The widely used H1 2006 DPDF fit [24] was obtained from the analysis of inclusive diffractive data (see Fig. 2.13) measured by H1 collaboration using large rapidity gap method (see section 2.3.6). This method allows to measure the diffractive cross section as a function of  $x_{IP}$ ,  $\beta$  and  $Q^2$ . The  $t$  dependence can be obtained only by direct scattered proton measurement (see section 3.3). Therefore only the integrated reduced cross section in the region  $|t| < 1\text{ GeV}^2$  and  $M_Y < 1.6\text{ GeV}$  is measured. In addition a diffractive cut  $x_{IP} < 0.05$  is applied because the rapidity gap  $\Delta\eta \sim \ln 1/x_{IP}$ .

The measured reduced cross section  $\sigma_r^{D(3)}(x_{IP}, \beta, Q^2)$  (2.46) is fitted by means of NLO QCD fit (see Figs. 3.4, 3.5, 3.6).

From the diffractive parton densities which obey DGLAP evolution (2.50) is the reduced cross section determined by formulas (2.48) and (2.47) with explicitly known perturbatively calculable coefficient functions.

In addition a Regge proton vertex factorisation expressed by formula (2.52) is supposed to be valid.

The pomeron and reggeon flux factors  $f_{IP/p}(x_{IP})$ ,  $f_{IR/p}(x_{IP})$  (2.53) are integrated over  $|t| < 1\text{ GeV}^2$  and their parameters are mostly fixed - known from other experiments (mainly from previous leading proton analysis [35]). Only two free parameters which will be fitted are the pomeron intercept  $\alpha_{IP}(0)$  and the scale factor  $n_{IR}$  which determines the fraction of the reggeon contribution.

The distribution function of the pomeron has at the initial scale  $Q_0^2 = 1.75\text{ GeV}^2$  for fit A, respectively  $Q_0^2 = 2.5\text{ GeV}^2$  for fit B the following form

$$zf_{i/IP}(z, Q_0^2) = A_q z^{B_q} (1-z)^{C_q} \quad i = u, d, s, \bar{u}, \bar{d}, \bar{s} \quad (3.1)$$

$$zf_{g/IP}(z, Q_0^2) = A_g (1-z)^{C_g}. \quad (3.2)$$

The contribution of heavy flavours is set to be zero for initial scale  $Q_0^2$  and is generated by DGLAP evolution above heavy quark mass threshold.

The parton densities  $f_{i/IR}$  of sub-leading reggeon exchange are taken from a parameterisation derived from fits to pion structure function data [36].

Finally there are 7 (6 for Fit B) free parameters to be fitted. Results are shown in Tab. 3.1. Fit B differs in different starting scale and by fixing of  $C_g$  coefficient to zero. The gluon part is therefore supposed to be constant for  $Q_0^2$ . The  $\chi^2$  values obtained for both fits are comparable.

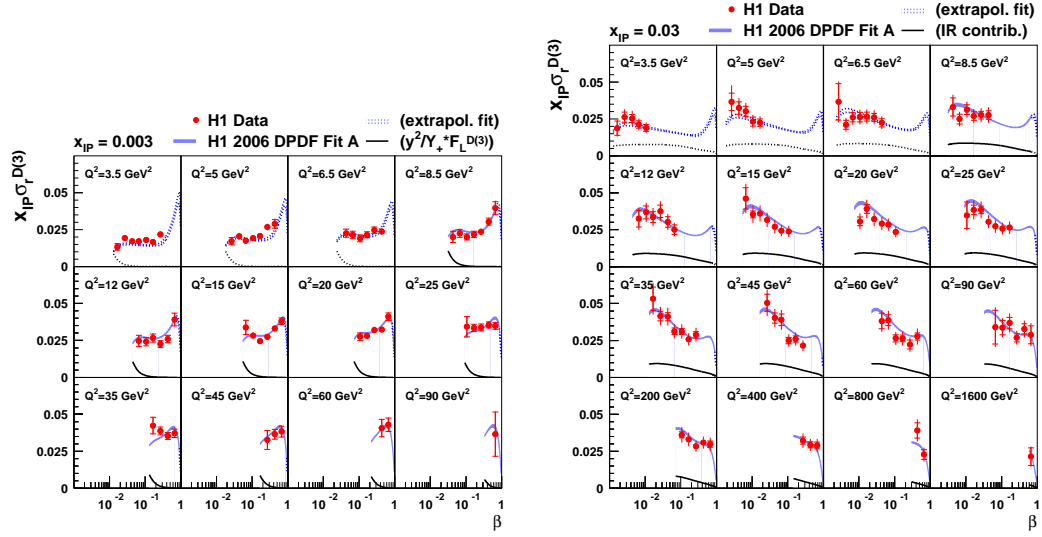


Fig. 3.4: The  $\beta$  dependence of  $\sigma_r$  for  $x_{IP} = 0.003$  (left) and  $x_{IP} = 0.03$  (right) and several  $Q^2$  values. The data are plotted by red points, the DPDF Fit A has a blue color. The black line denotes contribution from longitudinal structure function (in the left) and from sub-leading reggeon ( $IR$ ) exchange (in the right) to  $\sigma_r$  [24].

Fit Parameter	Fit A	Fit B
$\alpha_{IP}(0)$	$1.118 \pm 0.008$	$1.111 \pm 0.007$
$n_{IR}$	$1.7 \times 10^{-3}$	$1.4 \times 10^{-3}$
$A_q$	$1.06 \pm 0.32$	$0.70 \pm 0.11$
$B_q$	$2.30 \pm 0.36$	$1.50 \pm 0.12$
$C_q$	$0.57 \pm 0.15$	$0.45 \pm 0.09$
$A_g$	$0.15 \pm 0.03$	$0.37 \pm 0.02$
$C_g$	$-0.95 \pm 0.20$	0 (fix)

Tab. 3.1: Fitted parameters of H1 2006 Fit A and H1 2006 Fit B [24].

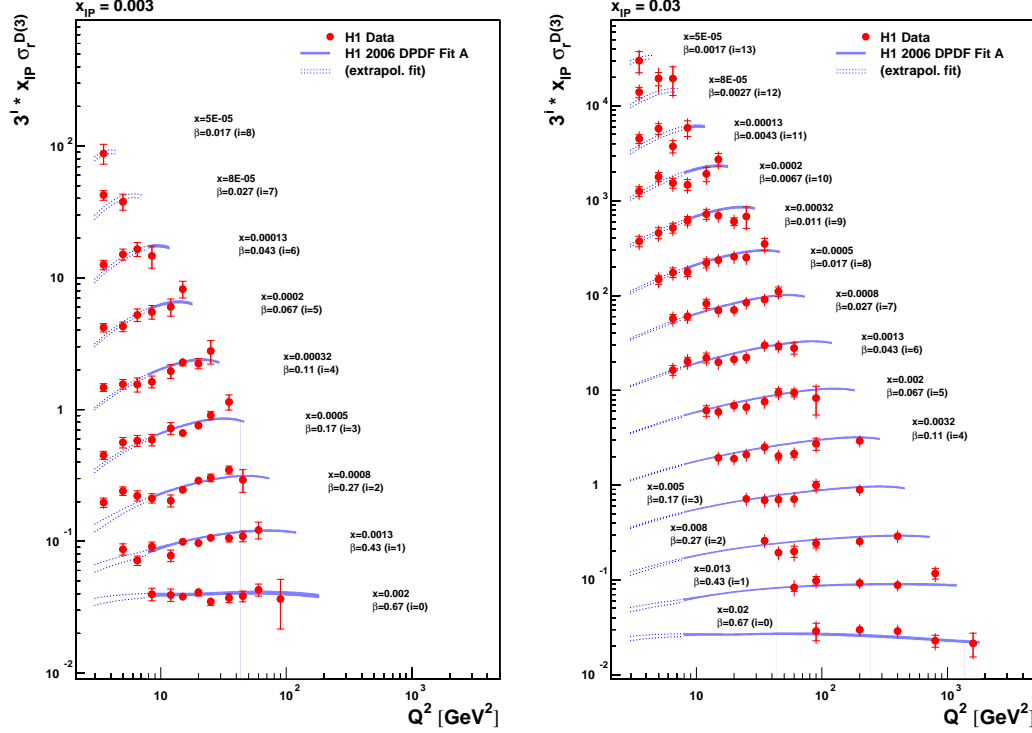


Fig. 3.5: The  $Q^2$  dependence of  $\sigma_r$  for  $x_{IP} = 0.003$  (left) and  $x_{IP} = 0.03$  (right) and various  $\beta$ . The data are plotted by red points, the DPDF Fit A has a blue color [24].

The fact that DPDF fits describe the data for different  $Q^2$  values demonstrates that the DGLAP evolution and generally QCD approach is valid for inclusive diffraction. This measurement also proved validity of "integrated" Regge vertex factorisation, i.e.  $x_{IP}$  dependence of  $\sigma_r$  is described by fit A (see Fig. 3.6).

### 3.3 Diffraction Measured by Forward Proton Spectrometers

Regge factorisation of proton vertex can be in detail studied using of method of detection of the scattered proton (see section 2.3.6). It allows to measure  $\sigma_r^{D(4)}$  in all four variables including the momentum transfer  $t$ . Other advantage of this method is the accessibility of higher  $x_{IP}$  values (up to  $x_{IP} < 0.1$  in the latest H1 analysis [37]) in comparison with the large rapidity gap method. Unfortunately due to low geometrical acceptance of the forward proton spectrometers this method can

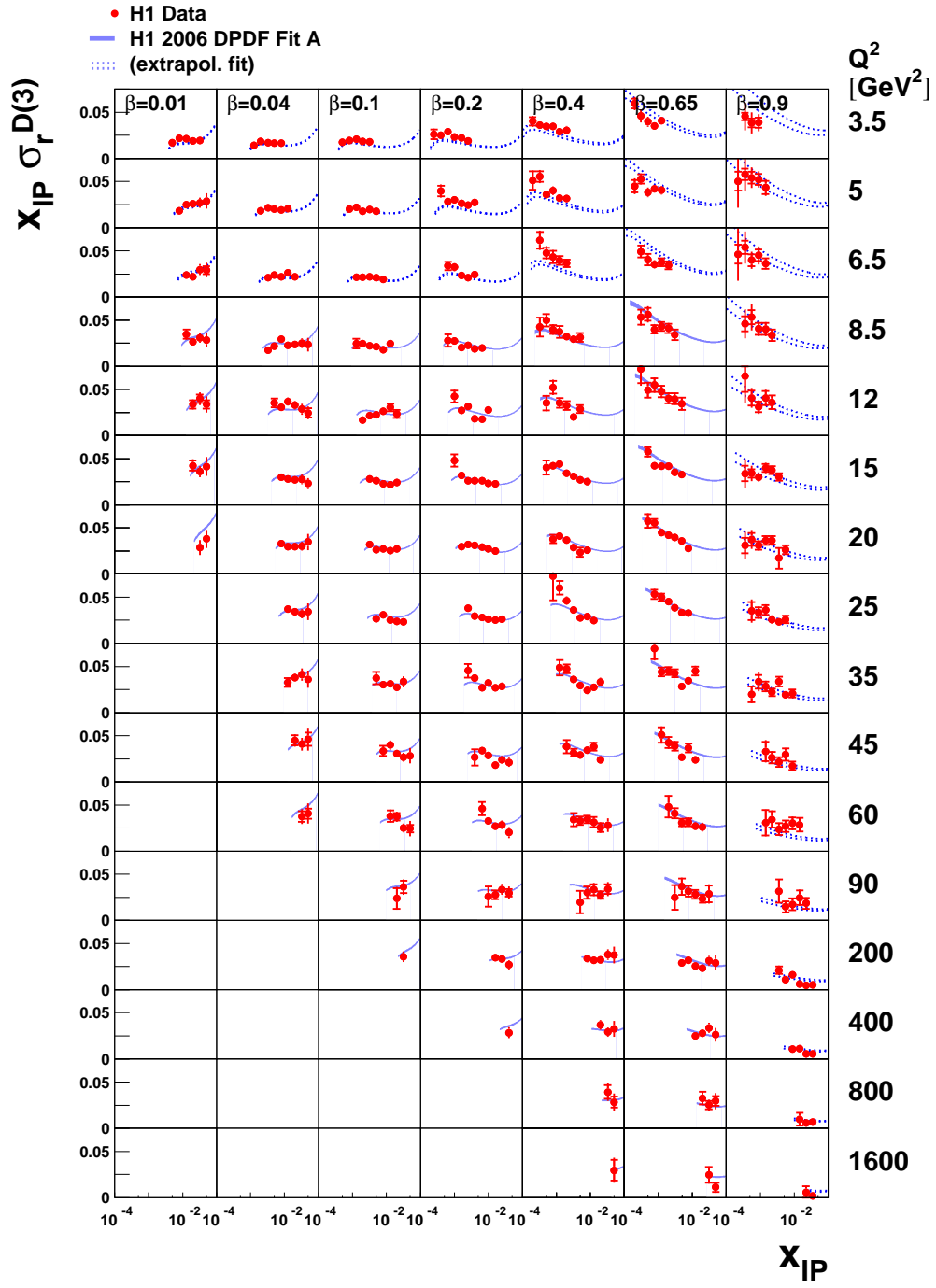


Fig. 3.6: The  $x_{IP}$  dependence of  $\sigma_r$  for different  $\beta$  and  $Q^2$ . The data are plotted by red points, the DPDF Fit A has a blue color [24].

not be an only source of measurements for QCD fits.

Test of Regge factorisation was done in [37] by dividing the phase space into three regions

$$4 < Q^2 < 12 \quad 12 < Q^2 < 36 \quad 36 < Q^2 < 110 \quad , \text{ where } Q^2 \text{ is in GeV}^2. \quad (3.3)$$

Parameters of the pomeron flux were fitted to the data independently in each  $Q^2$  interval whereas other parameters are keeping fixed. Pomeron flux parameters are  $Q^2$  range independent (see Fig. 3.7) and therefore we can conclude that Regge factorisation holds.

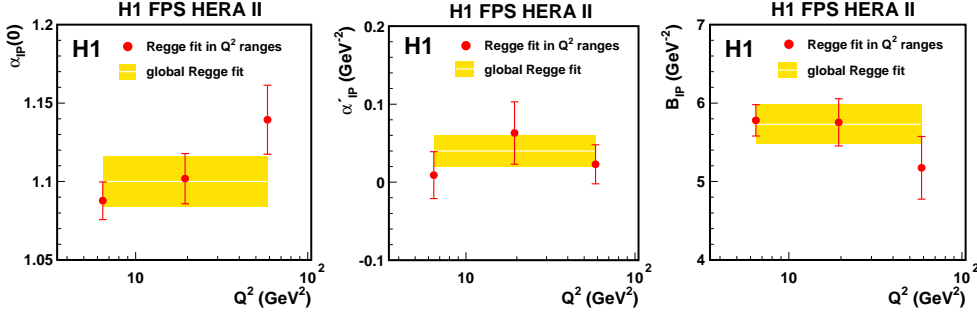


Fig. 3.7: The dependence of pomeron flux parameters on the  $Q^2$ . The white line with yellow error bar denotes the global full  $Q^2$  range Regge fit [37].

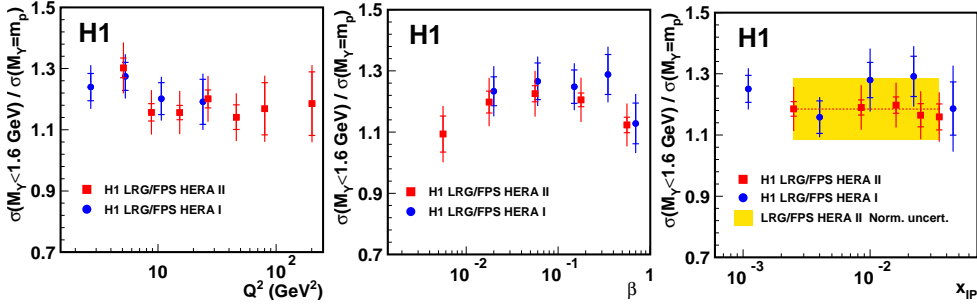


Fig. 3.8: The ratio of the reduced diffractive cross section  $\sigma_r^{D(3)}$  for  $M_Y < 1.6 \text{ GeV}$  and  $|t| < 1 \text{ GeV}^2$  obtained by large rapidity gap method to that for  $M_Y = M_P$  and  $|t| < 1 \text{ GeV}^2$  obtained from measurement with forward proton spectrometer as a function of  $Q^2$ ,  $\beta$  and  $x_{IP}$  [37].

When a large rapidity gap is observed the scattered proton usually stays intact but can also dissociate to the low mass hadronic system with the mass  $M_Y < 1.6 \text{ GeV}$ . In the measurement with forward proton spectrometer only bare proton

is detected and the ratio of the cross sections using these two methods determines relative contribution of the dissociation. The dependence of this ratio on various kinematic parameters is shown in Fig. 3.8. The cross section ratios are within the errors independent on the kinematic variables  $Q^2$ ,  $\beta$ ,  $x_{IP}$  and the mean value is

$$\frac{\sigma(M_Y < 1.6 \text{ GeV})}{\sigma(M_Y = M_P)} = 1.20 \pm 0.11. \quad (3.4)$$

It means that in measurement by large rapidity gap method in about 20 % of the events the scattered proton dissociated into hadronic system with mass smaller than 1.6 GeV.

### 3.4 Diffractive Dijet Production in DIS

The measurement of diffractive dijet in DIS is directly sensitive to the gluon contribution of DPDFs<sup>1</sup> and represents the one of the tests of the factorisation in diffraction. The NLO QCD analysis of measured data was performed by both collaborations and the detailed description can be found in [38], [39].

The H1 collaboration [38] sets a renormalization and factorisation scale equal to<sup>2</sup>  $(E_T^{*\text{jet1}})^2 + Q^2$  whereas ZEUS collaboration [39] sets renormalization scale equal to  $(E_T^{*\text{jet1}})^2$  and factorization scale to  $Q^2$ . The  $E_T^*$  jets cuts in NLO QCD data analysis must be asymmetric. It was the reason why H1 collaboration [38] has chosen

$$E_T^{*\text{jet1}} > 5.5 \text{ GeV} \quad \text{and} \quad E_T^{*\text{jet2}} > 4 \text{ GeV} \quad (3.5)$$

and ZEUS [39]

$$E_T^{*\text{jet1}} > 5 \text{ GeV} \quad \text{and} \quad E_T^{*\text{jet2}} > 4 \text{ GeV}. \quad (3.6)$$

The reason for this asymmetric cutting is following. If one fixes  $E_T^{*\text{jet2}}$  cut and decreases cut on  $E_T^{*\text{jet1}}$  the phase space of the measurement is increasing and therefore the total cross section must grow. Indeed the NLO cross section reaches the maximum but then nonphysically drops off to smaller values because of not fully cancelled negative interference terms [40].

Fig. 3.9 shows that H1 2006 Fit A overestimates the measured cross sections while NLO calculation with H1 2006 Fit B agrees with the data well. A similar feature observed also ZEUS collaboration (see Fig. 3.10).

The fact that inclusive measurements are not sensitive to a gluon part of DPDFs could mean that the agreement of H1 2006 Fit B with the dijet data is simply a coincidence. Therefore the combined H1 2007 Fit Jets [38] has been done by fitting

<sup>1</sup>The dominant leading order process is a boson-gluon fusion in this case.

<sup>2</sup>The sign \* denotes variables in the  $\gamma^*p$  center of mass frame with  $z$  axis collinear with proton and  $\gamma^*$  momentum.

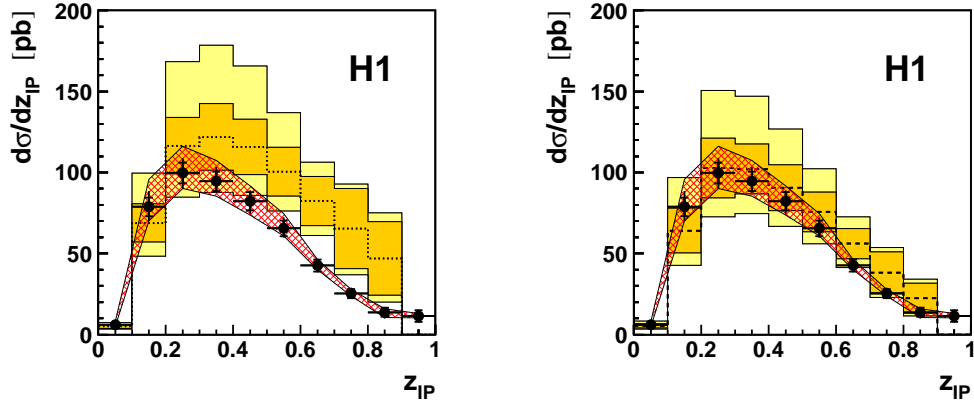


Fig. 3.9: H1 measurement of  $z_{IP}$  distribution [38] compared with NLO predictions with H1 2006 Fit A (left) and H1 2006 Fit B (right) DPDFs.

## ZEUS

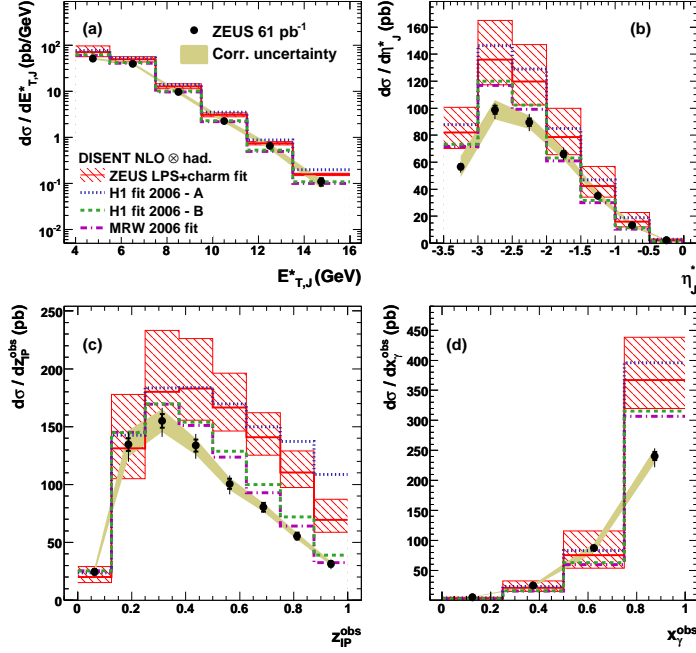


Fig. 3.10: ZEUS measurement of  $E_T$  and pseudorapidity of the leading jet in  $\gamma^*p$  CMS,  $z_{IP}$  and  $x_\gamma$  distribution [39] compared with NLO predictions with different DPDFs fits.



simultaneously inclusive and dijet diffractive data. Similar procedure was used also by ZEUS collaboration in [41] and this combined fit is called ZEUS SJ DPDF. The quark singlet and gluon parts of most common diffractive structure functions are shown in Fig. 3.11. It can be seen that the fits differ mostly in the gluon part where H1 Fit B has the highest values and the combined fits from H1 and ZEUS collaborations are smaller.

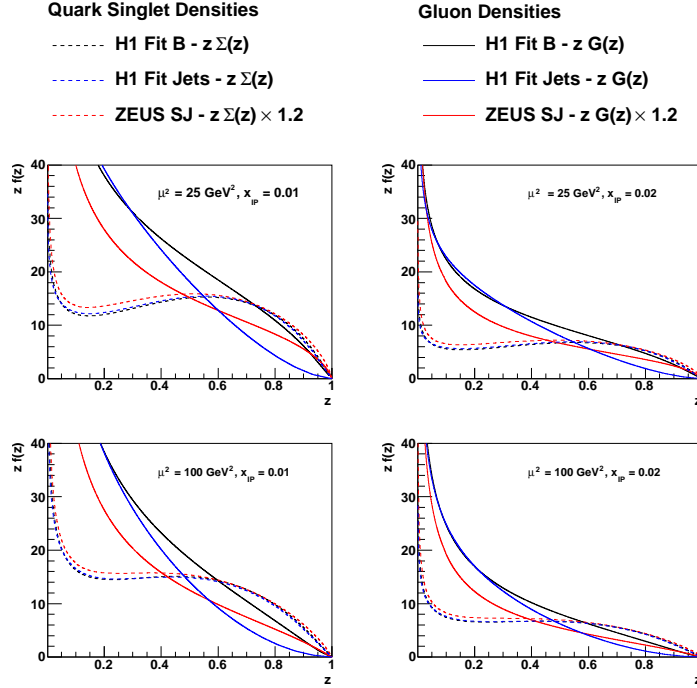


Fig. 3.11: Function values of quark singlet and gluon densities for DPDFs used in this analysis. Structure functions are integrated over  $|t| < 1 \text{ GeV}^2$  and  $M_Y < 1.6 \text{ GeV}$ .

We can conclude that the measurements of both collaborations confirm the factorisation theorem for the diffractive dijet production in DIS.

### 3.5 Factorisation Breaking in Hadron-Hadron Collisions

The hard diffraction was in a detailed way studied in  $p\bar{p}$  collision at Tevatron with the highest CMS energy around 2 TeV. The difference between diffraction at HERA and Tevatron is that diffraction at Tevatron can occur not only on either  $p$  or  $\bar{p}$  side but also on both sides. We call it single and double pomeron exchange (see Fig 3.12). Diffraction events can be detected by (anti-)proton spectrometers or by

means of large rapidity gap method. The hard scale is ensured by the presence of jets with high transverse energy.

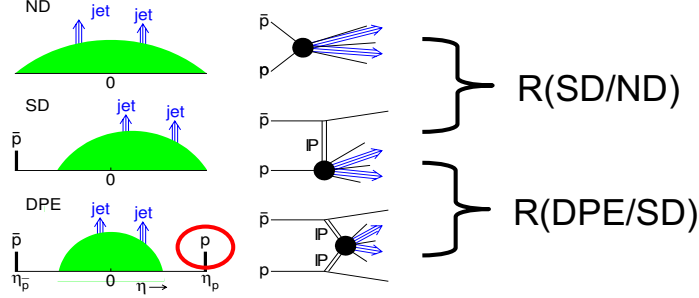


Fig. 3.12: Scheme of inclusive, single diffractive and double diffractive  $p\bar{p}$  collisions.

The interesting question is whether the diffractive structure function from HERA can be used at Tevatron. For this purpose the ratio  $R$  of dijet events in single diffractive and non-diffractive has been studied (see Fig 3.12)

$$R = \frac{N_{jj}^{SD}}{N_{jj}^{ND}}. \quad (3.7)$$

This ratio can be estimated from non-diffractive and diffractive parton distribution functions. In Fig. 3.13 is the  $R$  factor plotted as a function of fraction of the pomeron momentum with respect to the diffractive exchange  $\beta$  as measured by CDF collaboration [42]. The predicted values from HERA DPDFs are about one order in magnitude higher than the measurement!

This observation is explained theoretically assuming that factorisation breaking results from absorptive effects caused by multiple re-scattering effects. The rapidity gap can then be populated by secondary particles which spoil the experimental signature of the diffractive events [27].

The concept of so called rapidity gap survival probability  $S^2$  was introduced. By definition in  $ep$  diffractive DIS interactions is  $S^2 = 1$ . For Tevatron it reaches values  $S^2 \sim 0.1$  and is only a little bit  $\beta$  dependent (see Fig 3.13).

Understanding of the rapidity gap survival probability factors is of vital importance nowadays. Indeed a substantial attention is devoted to the central exclusive channel which is believed to be a discovery channel for the Higgs boson [43]

$$p + p \rightarrow p + p + H. \quad (3.8)$$

The advantage of this double pomeron exchange process is the presence of rapidity gap from both proton sides which provides a clean environment for Higgs production in the central region.

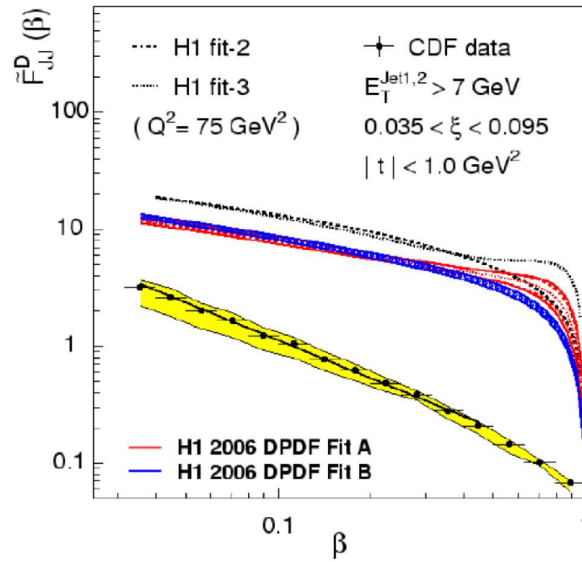


Fig. 3.13: The measurement of the  $R$  factor as a function of  $\beta$  at Tevatron. Result is compared with the prediction based on diffractive HERA DPDFs.

### 3.6 Diffractive Dijet Photoproduction

In diffractive photoproduction (see Fig. 2.14), in the leading order approximation, the small photon virtuality ( $Q^2 \ll 1 \text{ GeV}^2$ ) allows for partonic fluctuations that live long enough.

The photon may not couple directly to the quarks in the pomeron, but only a part of its four-momentum participates in the hard interaction. Such interactions are called resolved. The photon can still couple directly (with its whole four-momentum) to the quarks and these interactions are called direct. The resolved photon interactions resemble the hadron-hadron ones since two particles with structure, which is described by photon and diffractive structure functions, scatter on each other.

The variable  $x_\gamma$ , which is defined as a four-momentum fraction taking part in the hard interaction, is used to distinguish between the two regimes in photoproduction. Obviously, following relations hold:  $x_\gamma = 1$  and  $x_\gamma < 1$  for the direct and resolved photon interactions, respectively. Effects of fragmentation and a finite experimental resolution impose a smearing on the value of  $x_\gamma$ . In experiments, often a value of  $x_\gamma$  around 0.75 is considered to be a discriminator below (above) which the events are regarded as being due to resolved (direct) photon interaction, with reasonably low contamination of one in each other.

Because of the presence of these two photon interaction regimes, studying diffrac-

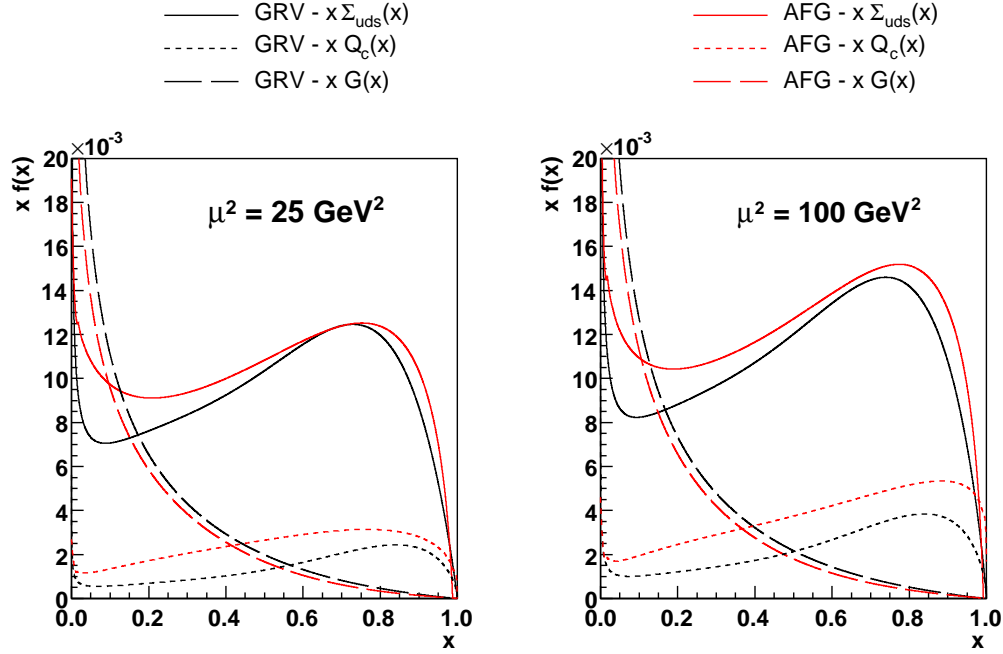


Fig. 3.14: Function values for  $uds$  quark singlet, charm and gluon contribution for GRV [44] and AFG [45]  $\gamma$ -PDF. NLO  $\gamma$ -PDFs are plotted in DIS $_{\gamma}$  factorisation scheme for two values of factorisation scale  $\mu^2 = 25 \text{ GeV}^2$  and  $\mu^2 = 100 \text{ GeV}^2$ .

tive processes in photoproduction is a useful tool for tests of the validity of the hard factorisation in diffraction.

The partonic structure of the photon was measured in  $\gamma^*\gamma$  deep inelastic scattering at LEP in  $e\bar{e}$  interactions [46]. The photon structure function contains perturbative point-like part and the resolved contribution which resembles to vector mesons. The photon PDFs are supposed to have a similar form as a PDFs of a meson at the starting scale  $Q_0^2$  and the point-like component at the initial scale is supposed to be zero. The evolution to the higher scales provides DGLAP equation which differs from equation for the proton by an additional inhomogeneous term. This term generate the point-like (or inhomogeneous) part of the photon PDFs and for high scales the point-like part is dominated except small  $x_{\gamma}$  values. The GRV HO [44] and AFG HO [45]  $\gamma$ -PDFs used in this thesis are plotted in Fig. 3.14.

There was an earlier prediction of Kaidalov et al. [47] that the factorisation breaking of the resolved part should induce a suppression of the NLO QCD expectation by about a factor of 0.34 due to additional interaction between the spectators which spoils the rapidity gap (see Fig. 3.15). This idea was widely discussed and

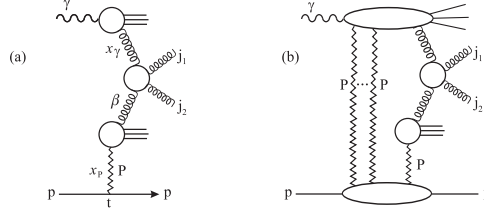


Fig. 3.15: Feynman diagrams for resolved diffractive photoproduction with exchange of one pomeron (left) and multiple pomeron (right) [27].

applied to published data in the studies of Klasen and Kramer [48, 49]. However recently [50] theoretical expectations were revised stressing the fact that due to the inhomogeneous term in the DGLAP evolution there is also point-like part of the  $\gamma$ -PDF the hadron-like part of the photon structure occurs only at lowest values of four-momentum fractions  $x_\gamma \sim 0.1$  which are experimentally hardly accessible. The dominant part of the resolved processes is therefore represented by the point-like photon interactions resulting in a significantly weaker suppression effect as compared to the 0.34 factor following from [50].

The first H1 measurement of diffractive dijet photoproduction with NLO QCD analysis [51] of the data was done in 2007<sup>3</sup>. H1 collaboration observed a global suppression of the dijet cross section with respect to NLO QCD calculation by a factor  $0.5 \pm 0.2$ . A new study of H1 collaboration [32] with a three time larger data sample and similar kinematic region (only exception is additional  $z_{IP} < 0.8$  cut) confirms the previous study [51] with a suppression factor of data with respect to NLO calculations  $0.6 \pm 0.2$ . Both H1 analyses used H1 2006 Fit B DPDF.

The ZEUS collaboration has made only one measurement with asymmetric cuts on  $E_T$  of the jets [54] in year 2007. They observed a suppression of the data about 0.8 for H1 2006 Fit B DPDF. In a recent study [41] ZEUS tests their new fit ZEUS SJ DPDF (see Fig. 3.11) also for diffractive dijet photoproduction data [54]. They obtained agreement of data and NLO simulations in shape and in normalisation for both published differential cross sections ( $x_\gamma$  and  $E_T^{\text{jets}}$ ). The hadronization corrections (see section 4.3) were taken from older publication [54].

In contradiction with expectations from [47, 50] neither experiment did observe a difference in suppression for the resolved enriched part ( $x_\gamma < 0.75$ ) and the direct enriched part of the cross section ( $x_\gamma > 0.75$ ). The calculations where such a kind of suppression is assumed do not describe the shape of  $x_\gamma$  distribution much worse

<sup>3</sup>Previous measurements of diffractive dijet photoproduction from H1 [52] and ZEUS [53] collaborations have been done with symmetric  $E_T^{\text{jets}}$  cuts and therefore are not suitable for NLO QCD analysis.

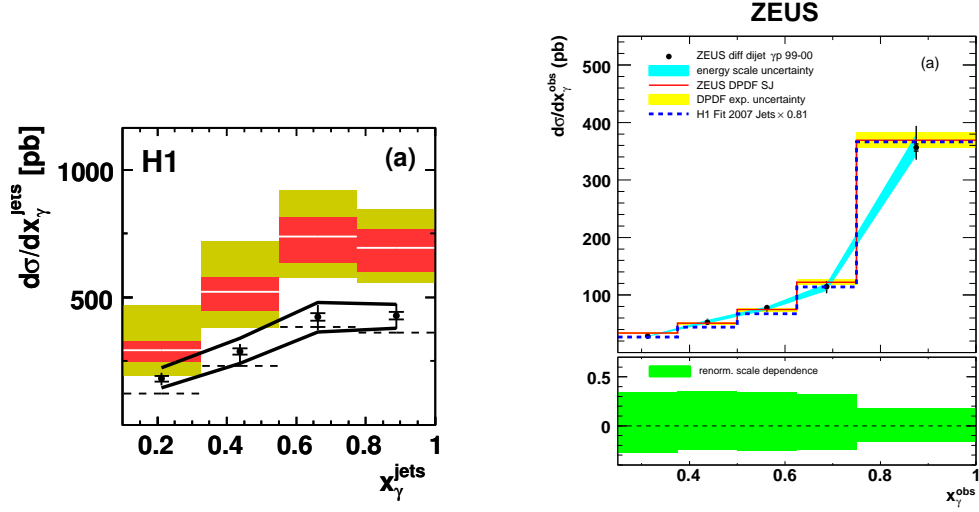


Fig. 3.16: The H1 [32] (left) and ZEUS [41] (right) measurements of  $x_\gamma$  distribution compared with NLO QCD predictions.

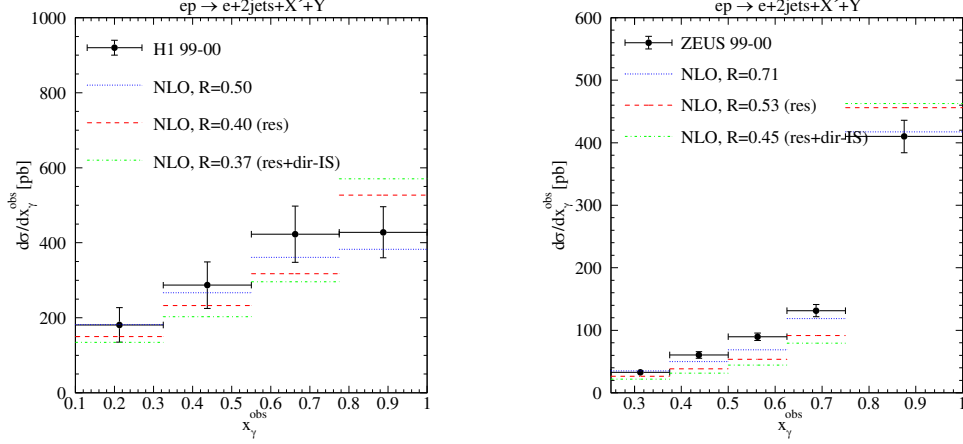


Fig. 3.17: The comparison of H1 [32] (left) and ZEUS [54] (right) measurements of  $x_\gamma$  distribution with NLO QCD prediction with H1 Fit B DPDF and GRV HO  $\gamma$ -PDF as calculated in [49]. Blue lines denote NLO distribution with global suppression factor, red and green lines represent NLO calculations with suppressed resolved part.

H1	ZEUS
$Q^2 < 0.01 \text{ GeV}^2$	$Q^2 < 1 \text{ GeV}^2$
$0.3 < y < 0.65$	$0.2 < y < 0.85$
$E_T^{\text{jet1}} > 5 \text{ GeV}$	$E_T^{\text{jet1}} > 7.5 \text{ GeV}$
$E_T^{\text{jet2}} > 4 \text{ GeV}$	$E_T^{\text{jet2}} > 6.5 \text{ GeV}$
$-1 < \eta^{\text{jet1(2)}} < 2$	$-1.5 < \eta^{\text{jet1(2)}} < 1.5$
Diffractive cuts	
$x_{IP} < 0.03$	$x_{IP} < 0.025$
$z_{IP} < 0.8$	
$ t  < 1 \text{ GeV}^2$	$ t  < 1 \text{ GeV}^2$
$M_Y < 1.6 \text{ GeV}$	$M_Y = M_P$

Tab. 3.2: Cuts used in H1 [32] and ZEUS [41, 54] analyses of diffractive dijet photoproduction.

than the predictions with global suppression factor (see Fig. 3.17).

In H1 and ZEUS analyses the diffractive events were selected with a large rapidity gap method and jets were identified using the inclusive  $k_T$  cluster algorithm (see section 2.2.4) in the laboratory frame. The phase space of both analyses was different (see Tab. 3.2), the main difference being at somewhat larger  $E_T^{\text{jet}}$  of ZEUS measurement. H1 collaboration collected data with a tagged electron that allowed to restrict the  $Q^2$  to very low values ( $Q^2 < 0.01 \text{ GeV}^2$ ), the ZEUS analysis was done with an untagged electron sample of events ( $Q^2 < 1 \text{ GeV}^2$ ). In H1 analysis the additional cut  $z_{IP} < 0.8$  was applied since the DPDF sets are not valid at the largest values of  $z_{IP}$  due to higher twist contribution.

There was a suggestion that the different conclusions about factorisation breaking of H1 and ZEUS analysis could be caused by different  $E_T^{\text{jets}}$  cuts of the analysis. The  $E_T$  jet dependence of the factorisation was motivated by observation that the suppression decreases with increasing  $E_T$  of the leading jet (see Fig. 3.18).

To study this effect in a more detailed way the H1 Hight Pt analysis [55] was done with the cuts similar to ZEUS analysis. The only differences between both analyses are in  $y$ ,  $Q^2$  and  $M_Y$  cuts (see Fig. 5.1). Suppression factor in [55] was really a little bit smaller (0.61 whereas Low Pt analysis [32] gives 0.58, both for H1 Fit B DPDF) but it was still present.

The challenge of this thesis is to check and discuss a possible sources for different H1 and ZEUS conclusions which concern diffractive dijet in photoproduction.

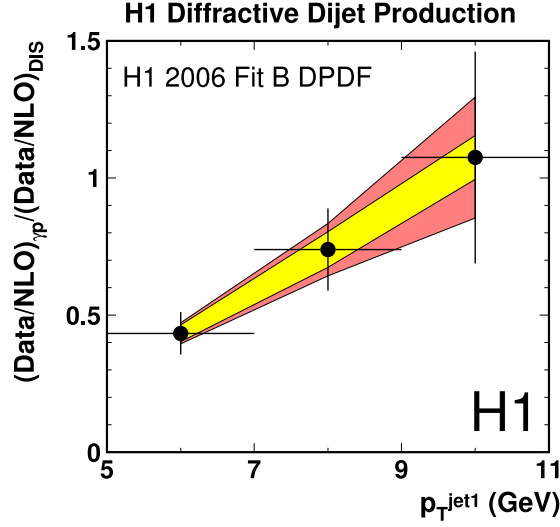


Fig. 3.18: The double ratio of  $d\sigma/dE_T^{\text{jet1}}$  for data to NLO QCD predictions in diffractive photoproduction to DDIS. Plot is based on published data from [51].

### 3.7 Diffractive Open Charm Production in Photoproduction

The H1 and ZEUS collaborations measured diffractive photoproduction  $ep \rightarrow eXY$  where the diffractive system  $X$  contains at least one charmed hadron [56, 57]. The  $D^*$  mesons are reconstructed via a golden decay into a kaon and two pions.

The measured distributions for  $y$  and  $W$  variable<sup>4</sup> are presented in Fig. 3.19. It can be seen that the NLO predictions overestimated H1 data while ZEUS data are above NLO calculations.

The cross section ratios of data and NLO calculations for H1 and ZEUS open charm analysis are

$$\sigma_{data}^{H1}/\sigma_{NLO}^{H1} = 0.74 \pm 0.25 \pm 0.17 \quad (3.9)$$

$$\sigma_{data}^{ZEUS}/\sigma_{NLO}^{ZEUS} = 1.35 \pm 0.23 \pm 0.40, \quad (3.10)$$

where the NLO calculations were performed with H1 2006 Fit B DPDF. The first error is experimental and the second error is theoretical one connected with a scale uncertainty of NLO calculations. It is obvious that due to large errors results of both collaboration are compatible with no suppression hypothesis.

---

<sup>4</sup>In photoproduction  $W = \sqrt{ys}$



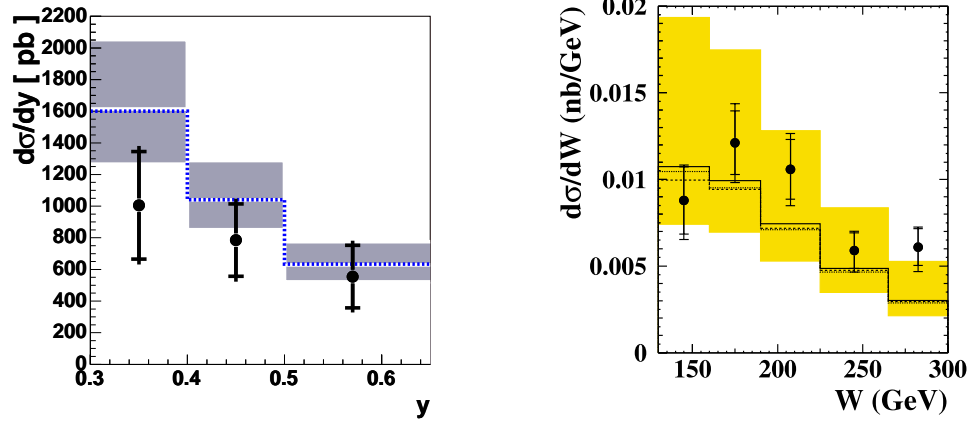


Fig. 3.19: Measurement of  $y$  (left) and  $W$  (right) distribution for diffractive open charm production in photoproduction published by H1 [56] (left) and ZEUS [57] (right) collaborations. NLO calculations with H1 Fit B are denoted with full blue line on the left and with dashed line on the right.

The double ratio between H1 and ZEUS measurements with experimental uncertainty

$$\frac{\sigma_{data}^{H1}/\sigma_{NLO}^{H1}}{\sigma_{data}^{ZEUS}/\sigma_{NLO}^{ZEUS}} = 0.55 \pm 0.21 \quad (3.11)$$

can however signalise that similar discrepancy between analyses like in diffractive dijet photoproduction could be not excluded.

## Chapter 4

# Crosscheck of H1 and ZEUS Results

In the following the crosscheck of theoretical calculations which were published by H1 [32] and ZEUS [41, 54] collaborations will be done (see section 3.6). Both collaboration made their calculation in next-to-leading order accuracy. Unfortunately no NLO Monte Carlo (with incorporated hadronization) exists nowadays for  $ep$  interactions. It means that the parton-level NLO results must be corrected for hadronization by so called hadronization corrections (HC). These HC are estimated from LO Monte Carlo. Final results are obtained as a product of NLO cross sections and HC.

In next three sections the crosscheck of NLO calculations at parton level (section 4.2), hadronization corrections (section 4.3) and NLO predictions corrected for hadronization (section 4.4) will be presented. At the end the sensitivity of the calculation to photon structure function will be studied (section 4.5).

### 4.1 Reconstruction Formulas

Invariant quantities which are defined in the theory chapter must be obtained from momenta of the particles or the jets. There usually exist more reconstructions formulas for particular kinematic quantity. The choice of the method depends on experimental ability and accuracy of the measurement of observables using different reconstruction formulas.

In the case of tagged photoproduction the scattered electron energy  $E'_e$  is measured directly in electron tagger. Inelasticity  $y$  is then calculated as

$$y = 1 - \frac{E'_e}{E_e^{\text{beam}}} \quad (4.1)$$

where  $E_e^{\text{beam}}$  is a beam energy of the electron. For untagged photoproduction  $y$  is

determined from all particles in HFS (system  $X$ ) according to the formula

$$y = \frac{\sum_{\text{HFS}} (E_i - P_{z,i})}{2E_e^{\text{beam}}} = \frac{\sum_{\text{HFS}} E_{T,i} e^{-\eta_i}}{2E_e^{\text{beam}}}. \quad (4.2)$$

The invariant mass of  $\gamma^* p$  system  $W$  in photoproduction is always determined from the relation  $W = \sqrt{sy}$ .

Because the scattered proton is not detected in neither analysis the analog of formula (4.2) is used to reconstruct  $x_{IP}$ <sup>1</sup>

$$x_{IP} = \frac{\sum_{\text{HFS}} (E_i + P_{z,i})}{2E_P^{\text{beam}}} = \frac{\sum_{\text{HFS}} E_{T,i} e^{\eta_i}}{2E_P^{\text{beam}}}. \quad (4.3)$$

Next variables which must be reconstructed are the fractions of four-momentum transferred to the hard process from photon and pomeron side ( $x_\gamma$  and  $z_{IP}$ )

$$x_\gamma = \frac{\sum_{\text{jets}} (E_i - P_{z,i})}{2yE_e^{\text{beam}}} = \frac{\sum_{\text{jets}} (E_i - P_{z,i})}{\sum_{\text{HFS}} (E_i - P_{z,i})} = \frac{\sum_{\text{jets}} E_{T,i} e^{-\eta_i}}{\sum_{\text{HFS}} E_{T,i} e^{-\eta_i}} \quad (4.4)$$

$$z_{IP} = \frac{\sum_{\text{jets}} (E_i + P_{z,i})}{2x_{IP}E_P^{\text{beam}}} = \frac{\sum_{\text{jets}} (E_i + P_{z,i})}{\sum_{\text{HFS}} (E_i + P_{z,i})} = \frac{\sum_{\text{jets}} E_{T,i} e^{\eta_i}}{\sum_{\text{HFS}} E_{T,i} e^{\eta_i}}. \quad (4.5)$$

Sum over jets is sum of contributions from leading and sub-leading jet reconstructed using inclusive  $k_T$ -jet algorithm in laboratory frame with parameter  $R = 1$  (see section 2.2.4).

Mean pseudorapidity  $\langle \eta^{\text{jets}} \rangle$  of dijet system and the interval in pseudorapidities between jets  $|\Delta \eta^{\text{jets}}|$  is defined in a natural way

$$|\Delta \eta^{\text{jets}}| = |\eta^{\text{jet1}} - \eta^{\text{jet2}}| \quad \langle \eta^{\text{jets}} \rangle = \frac{1}{2} (\eta^{\text{jet1}} + \eta^{\text{jet2}}). \quad (4.6)$$

Invariant masses of diffractive system  $X$  and effective mass of the dijet system are reconstructed as

$$M_X = \sqrt{yx_{IP}s} \quad M_{12} = \sqrt{2J^{(1)} \cdot J^{(2)}} \quad (4.7)$$

where  $J^{(1)}$  and  $J^{(2)}$  are four-momenta of the first and the second jet which are regarded to be massless.

---

<sup>1</sup>In the analyses with scattered proton measured in forward proton spectrometers is  $x_{IP}$  estimated directly by analogy with (4.1) as  $x_{IP} = 1 - \frac{E'_P}{E_P^{\text{beam}}}$ .

## 4.2 Parton-Level NLO Calculations

For our NLO calculation the program Frixione *et al.* [58] adopted for diffractive photoproduction was used. The renormalization and factorisation scales are both set to the leading jet transverse energy i.e.  $\mu_R = \mu_F = E_T^{\text{jet1}}$ . The NLO calculations are performed with number of flavours fixed to 5 and with  $\Lambda_5 = 0.228 \text{ GeV}$ , corresponding to 2-loop  $\alpha_s(M_Z) = 0.118$ . These parameters are the same as in H1 analysis. NLO results only slightly depend on the number of active flavours (5 or 4) used. Scale error band is conventionally given by varied renormalization and factorization scale simultaneously by factor 0.5 and 2.

ZEUS collaboration uses alternative NLO QCD program written by Klasen and Kramer [59]. A compatibility of both NLO programs was checked in [55]. The difference between these two programs in differential cross sections is mostly much smaller than scale uncertainty and is caused by another method of cancellations of infrared and collinear singularities. ZEUS calculations in [54] are performed with  $N_f = 4$ . Changing of number of active flavours to  $N_f = 5$  (with the same  $\alpha_s(M_Z)$ ) leads [54] to increase of cross section for  $x_\gamma > 0.75$  by about 10 % and is negligible elsewhere.

Frixione NLO program was written to simulate hadron-hadron and photon-hadron collisions. Adoption of NLO program for diffractive photoproduction is done by segmentation in  $x_{IP}$  and  $y$  variables from proton and electron side. Effectively the program simulates the interaction of resolved photon with pomeron (hadron-hadron type of collision) or photon with pomeron (photon-hadron type) for direct photoproduction. These cross sections are summed for all  $(x_{IP}, y)$  combinations with the weight done as product of pomeron (2.53) and photon flux (2.56) according to the factorization formula (2.57). Photon has energy  $yE_e^{\text{beam}}$  and pomeron  $x_{IP}E_P^{\text{beam}}$ . At the end the direct and resolved parts must be summed because only sum has a physical meaning. This approach is possible because virtuality of the "colliding" photon  $Q^2$  and pomeron  $-t$  (both maximally  $1 \text{ GeV}^2$ ) are much smaller than square of the hard scale ( $\mu^2 > 25 \text{ GeV}^2$ ) so the time of life of colliding objects is long enough in comparison with time of the collision.

Results of NLO calculations for H1 (ZEUS) kinematics are plotted with full line in Fig. 4.1 (Fig. 4.2). In the calculations the GRV HO (High Order)  $\gamma$ -PDF is used. Calculation are made for H1 2006 Fit B, H1 2007 Fit Jets and ZEUS 2009 SJ DPDFs (see section 3.4). The H1 data measured by large rapidity gap method and the fits done by H1 collaboration are published for  $M_Y < 1.6 \text{ GeV}$  range whereas ZEUS unfolds cross sections and fits to the proton mass ( $M_Y = M_P$ ). Therefore the ZEUS fits must be multiplied by factor 1.2 to convert them to the H1  $M_Y$  convention or H1 fits must be divided by 1.2 to convert them to  $M_Y = M_P$  convention used in ZEUS analysis. This factor was determined from the measurements with forward proton spectrometers (see section 3.3). From Figs. 4.1 and 4.2 is seen that the most

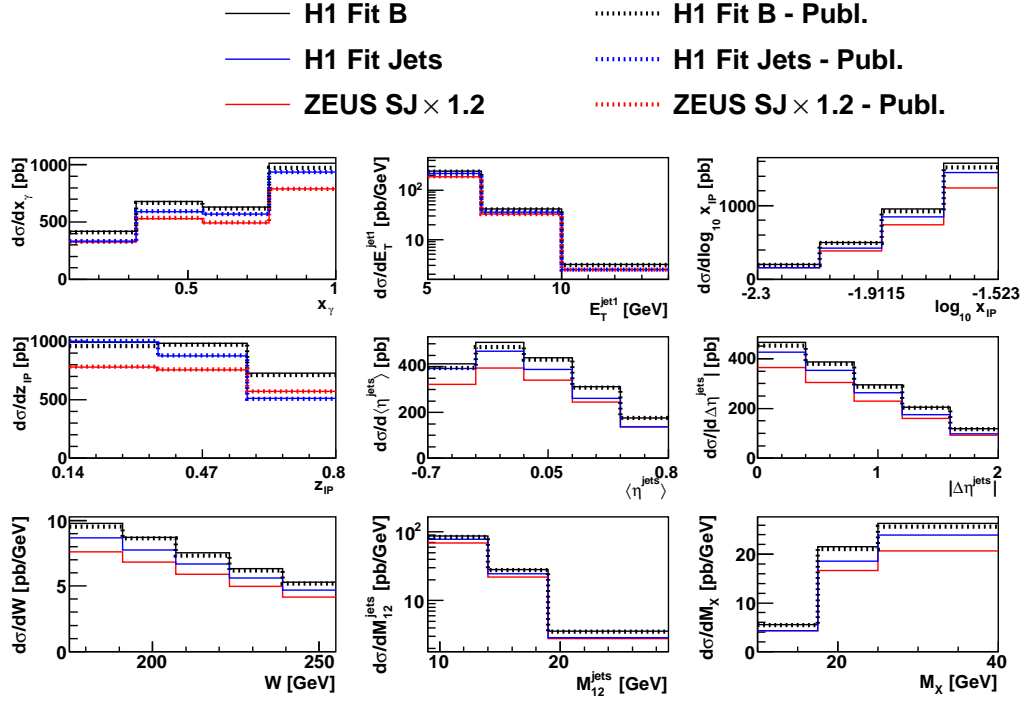


Fig. 4.1: Crosscheck of NLO calculations for H1 phase space for three DPDFs and GRV  $\gamma$ -PDF. Doted lines are H1 calculations published in [32].

sensitive variable from the point of view of the diffractive structure function used is  $z_{IP}$  variable. The total calculated cross section is the largest for H1 Fit B, the smallest for ZEUS SJ and H1 Fit Jets gives intermediate values. This behavior is determined by course of DPDFs plotted in Fig. 3.11.

Published NLO calculations are denoted with dotted lines. The small disagreement between published and recalculated differential ZEUS cross sections for H1 Fit B can be caused by using of different NLO program and the smaller number of quark flavours in ZEUS calculations [54].

### 4.3 Hadronization Corrections

It was already mentioned in the introduction of this chapter that no NLO program for  $ep$  interactions with incorporated hadronization exists in the present. Leading order Monte Carlo models imitate some features of NLO by using initial and final state parton showers so the shapes of parton-level distributions could be comparable

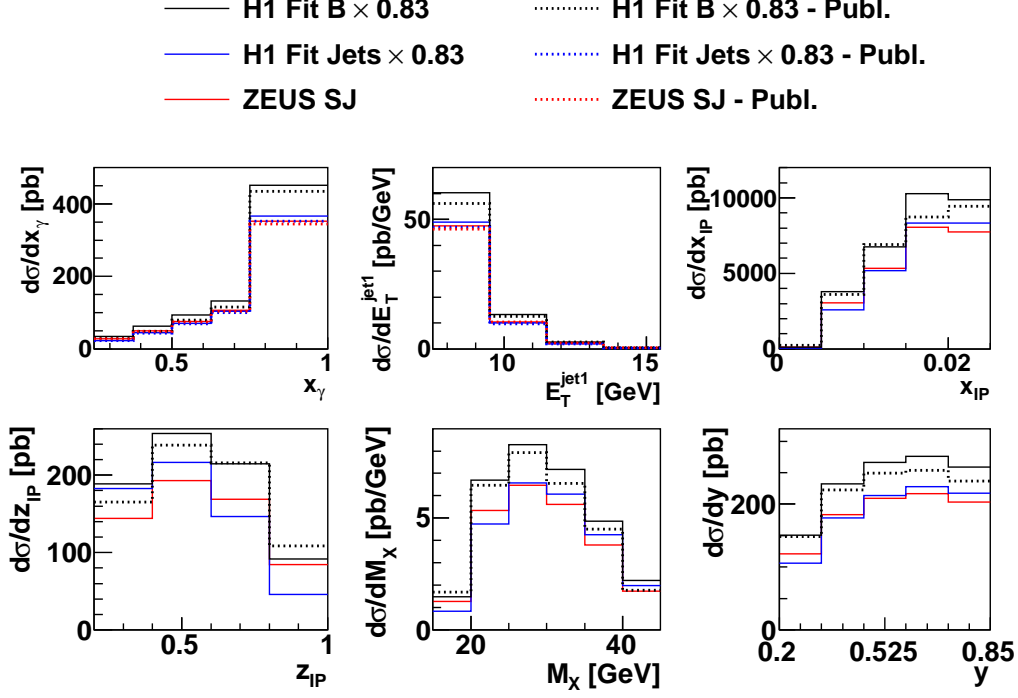


Fig. 4.2: Crosscheck of NLO calculations for ZEUS phase space for three DPDFs and GRV  $\gamma$ -PDF. Dotted lines are ZEUS calculations published in [41] (H1 Fit Jets, ZEUS SJ) and in [54] (H1 Fit B).

whereas the normalisation could differ significantly. The only way is to assume that hadronization simulated by LO MC will be similar to explicitly unknown hadronization of NLO parton-level.

Usual procedure of estimating of hadron-level NLO cross sections is:

1. Calculate parton-level NLO.
2. Calculate LO MC differential cross sections and reweight them in order to obtain very close LO parton-level and NLO parton-level cross section distributions.
3. From this reweighted LO MC model calculate the hadronization corrections  $C_i$  for all bins in kinematic variables we are interested

$$C_i = \frac{\sigma_i^{LO_{hadr}}}{\sigma_i^{LO_{part}}} \quad (4.8)$$

where the binning of the histograms and the kinematic cuts are the same at both levels.

4. Apply these HC to NLO from step 1. Hadron-level cross section in particular bin is then expressed as

$$\sigma_i^{NLOhadr} = C_i \sigma_i^{NLOpart}. \quad (4.9)$$

There are some important aspects of this method:

- To ensure conformity between Monte Carlo models and NLO predictions the same photon and diffractive structure functions should be used. On the other side the NLO structure functions cannot be applied directly in LO MC at least because there arises a question which NLO factorisation scheme (MS, DIS) one should use in LO program. So if both versions of the fit are available the proper procedure is to use LO version in Monte Carlo and NLO version in NLO program. It is demonstrated in Fig. 4.3 where are shown LO and NLO versions of GRV photon PDF. It is clear they differ significantly.

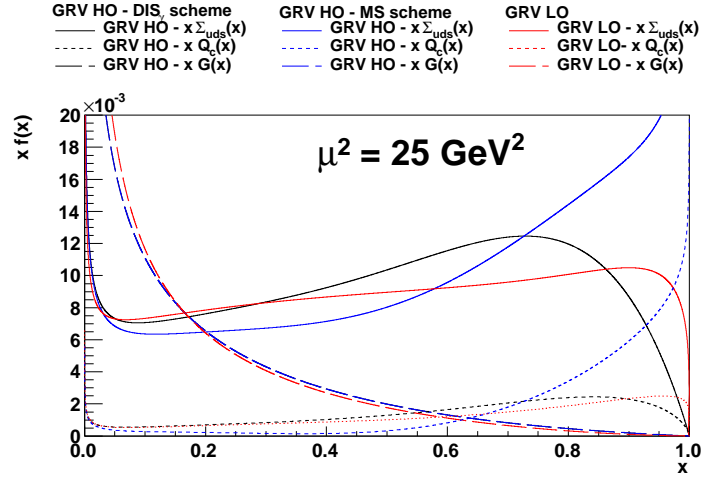


Fig. 4.3: GRV  $\gamma$ -PDF in LO and NLO (HO) version. NLO  $\gamma$ -PDF is plotted in DIS $_{\gamma}$  and MS factorisation scheme. Contribution from quark singlet of light quarks is denoted with full line, charm component with dotted line and gluon part with dashed line. Gluon component in NLO is scheme independent.

- Hadronization corrections depend on the model of hadronization which is implemented in MC (see section 2.2.4). In our analysis the RAPGAP MC with

Lund String Model of hadronization is used. Using of an alternative cluster model of the fragmentation implemented in MC program HERWIG [14] can provide valuable information about systematic errors. Such a procedure was used in [51], where the HERWIG MC was adopted to the diffraction by means of method described in previous section. Differences between HC calculated by RAPGAP and HERWIG were about 3 % in all bins.

- The reweighting procedure to LO MC distributions is applied in order to achieve better agreement of NLO and LO MC parton-levels. In general there exists 4 classes of events.
  1. Events which fulfill parton and hadron-level cuts.
  2. Events which fulfill parton-level cuts but not hadron-level cuts.
  3. Events which do not fulfil parton-level cuts but fulfill cuts in hadron-level.
  4. Events which are outside of the phase space at both levels.

The weights of the events  $W_{a_i}$  are mostly set in a way that some crucial distribution  $a_i$  ( $i$  indexes bins of this distribution at parton level) is after reweighting at parton-level identical to NLO distribution. Then

$$W_{a_i} = \frac{\sigma_{a_i}^{NLOpart}}{\sigma_{a_i}^{LOpart}} \quad (4.10)$$

and we can tell the parton-level MC was reweighted to NLO in  $a_i$  variable. The shapes of other distributions after reweighting change too. If all studied distributions are closer to the NLO after reweighting, the procedure was successful.

All kinematic variables where the cuts are applied and which will be plotted must be defined at both levels in the same way (even when the event do not fulfill the cuts in one level). For example there can not be any limit for the lowest transverse energy of the jets recognised by jet algorithm otherwise there arises a risk that event will fulfill hadron cuts but at parton-level there will be only one jet and the jets variables  $z_{IP}$ ,  $x_\gamma$  and  $M_{12}$  lost their sense as well as formula (4.10) for  $a = z_{IP}, x_\gamma, M_{12}$ .

If even after this reweighting to one variable the agreement between NLO and LO parton-level is not sufficient more complex reweighting procedure must be used, typically 2D reweighting or stepwise reweighting to more variables.

Reweighting is in general not unique because the events from class 3 do not influence parton level distributions but influence hadron-level ones. Changing of weights of these events will change hadron-level distributions and also HC but will preserve parton level distributions.



Here the hadronization corrections were estimated for 3 DPDFs (H1 Fit B, H1 Fit Jets and ZEUS SJ) and photon structure function GRV LO. The hadronization corrections were calculated using MC RAPGAP in the phase space defined in H1 [32] and ZEUS [54] analyses.

ZEUS SJ DPDF fit is defined from starting scale  $Q_0^2 = 1.8 \text{ GeV}^2$  and therefore the backward DGLAP evolution to  $1 \text{ GeV}^2$  was performed with program QCDNUM [60] with the same parameters as used ZEUS [41] in forward evolution to larger scales. The reason for the extension of the region of definition is that RAPGAP uses for simulation of parton showers DPDFs from the scale of  $1 \text{ GeV}^2$ .

H1 Fit Jets DPDF was not directly implemented into RAPGAP instead ZEUS SJ was reweighted to NLO with H1 Fit Jets.

The reweighting method was identical for H1 and ZEUS phase space and for all DPDFs and is inspired by ZEUS analysis. Two 2D histograms ( $z_{IP}$ ,  $x_\gamma$ ) with two bins in  $x_\gamma$  ( $x_\gamma < 0.75$  and  $x_\gamma > 0.75$ ) and the same binning in  $z_{IP}$  like in original H1 (ZEUS) analysis were filled by NLO and by parton-level RAPGAP calculated distributions. Weights were determined using (4.10).

The correspondence between NLO and LO parton-levels is demonstrated in the upper part of figures 4.4, 4.5, 4.6 and 4.8, 4.9, 4.10. NLO parton distributions mostly agree in shape with parton-level RAPGAP distributions but the normalisation is completely different. NLO differential cross sections are approximately two times higher than in LO model. Similar behaviour has been observed in H1 analyses [51, 32]. On the contrary in ZEUS analysis are NLO calculations smaller than leading order RAPGAP cross sections [54, 61]. Reweighting of LO model slightly improves the agreement between NLO and LO parton-level cross sections (see Figs. 4.4, 4.5, 4.6 and 4.8, 4.9, 4.10).

Calculated hadronization corrections are shown at the lower parts of figures 4.4, 4.5, 4.6 and 4.8, 4.9, 4.10. The reweighting procedure mostly affects bins with small cross section where the migration from other bins plays substantial role. Values of HC in these bins have however small impact to the total cross section.

Overview of all HC calculated for H1 and ZEUS can be seen in Fig. 4.7 and 4.11. The choice of the different DPDFs influences HC only a little and mostly in bins with low cross sections. HC calculated for H1 agree with published hadronization corrections [32] however HC calculated for ZEUS are lower than published ones [54]. Reason for this difference is difficult to establish. Some effect could have the fact that ZEUS used very old DPDF (H1 1997 LO Fit 2 from data measured in 1994 [62]) when knowledge of the gluon part of the DPDF (most important in this analysis) was limited.

The mean values of HC are shown in Tab. 4.1. It can be seen that ZEUS published correction are about 16 % higher than HC calculated here.

Neither collaboration published errors of their hadronization corrections.

A detailed study of HC and the correspondence between NLO and LO cross

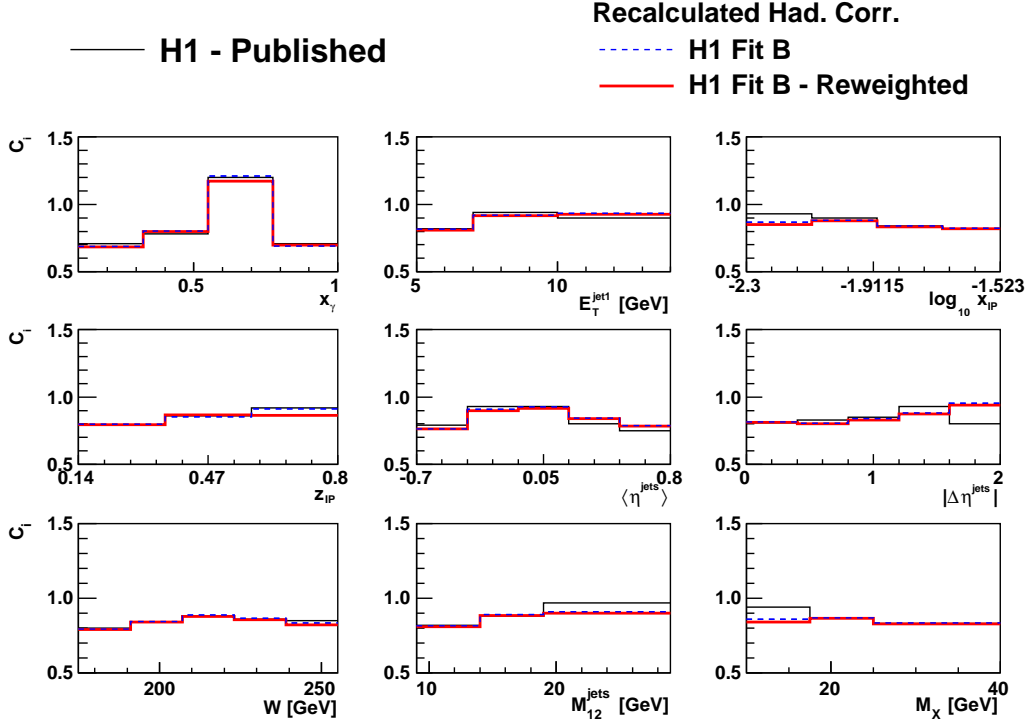
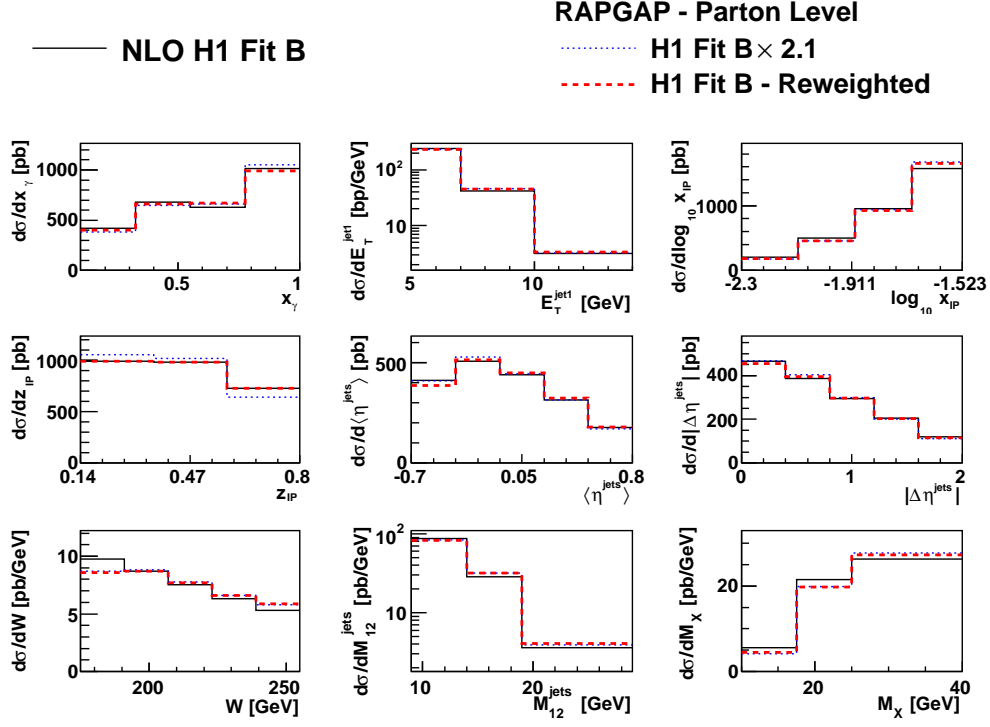


Fig. 4.4: At the top: correspondence between NLO and parton-level RAPGAP (before and after reweighting).

At the bottom: Hadronization corrections calculated by means of RAPGAP.

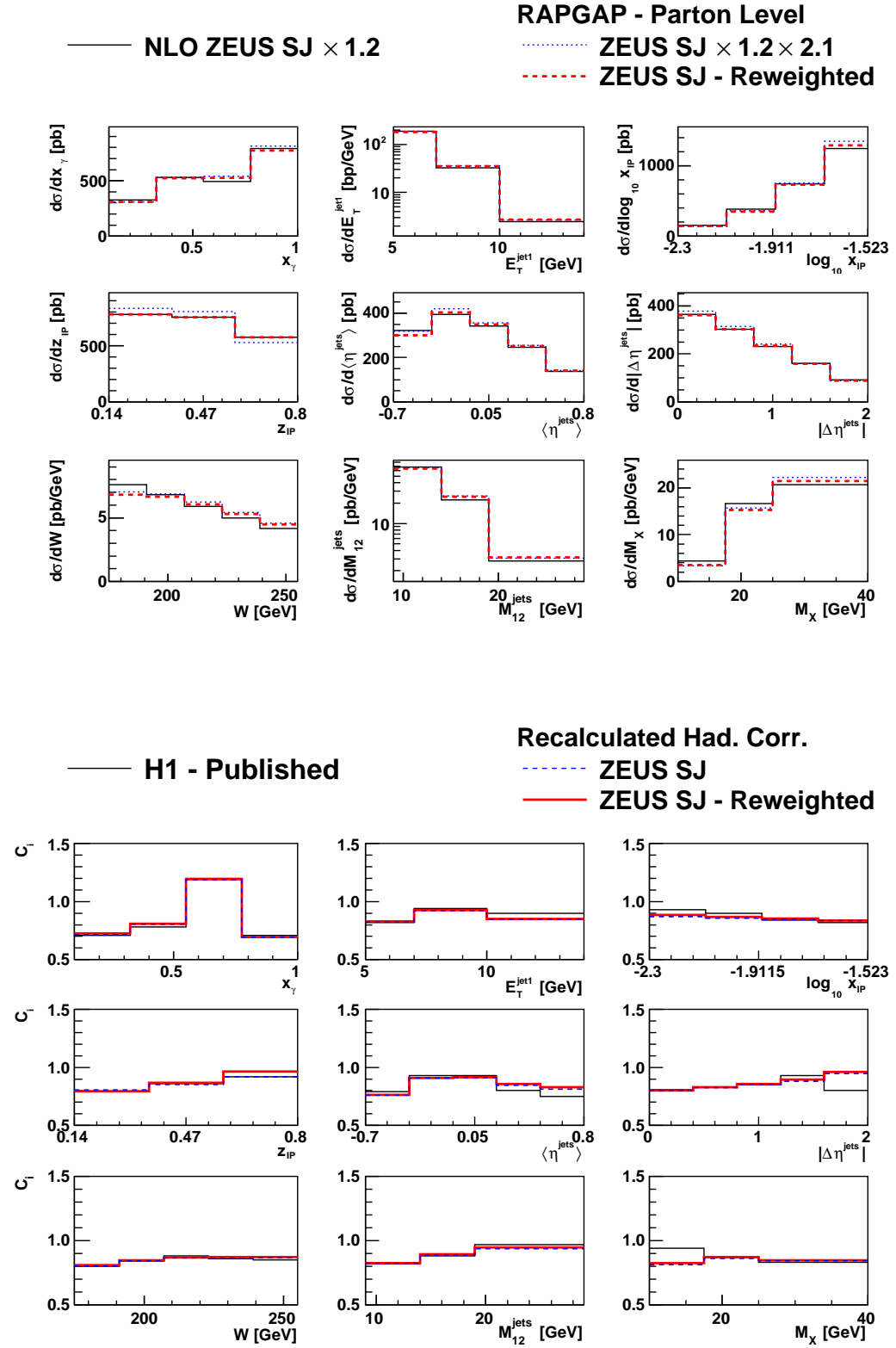


Fig. 4.5: At the top: correspondence between NLO and parton-level RAPGAP (before and after reweighting).

At the bottom: Hadronization correction calculated by means of RAPGAP.

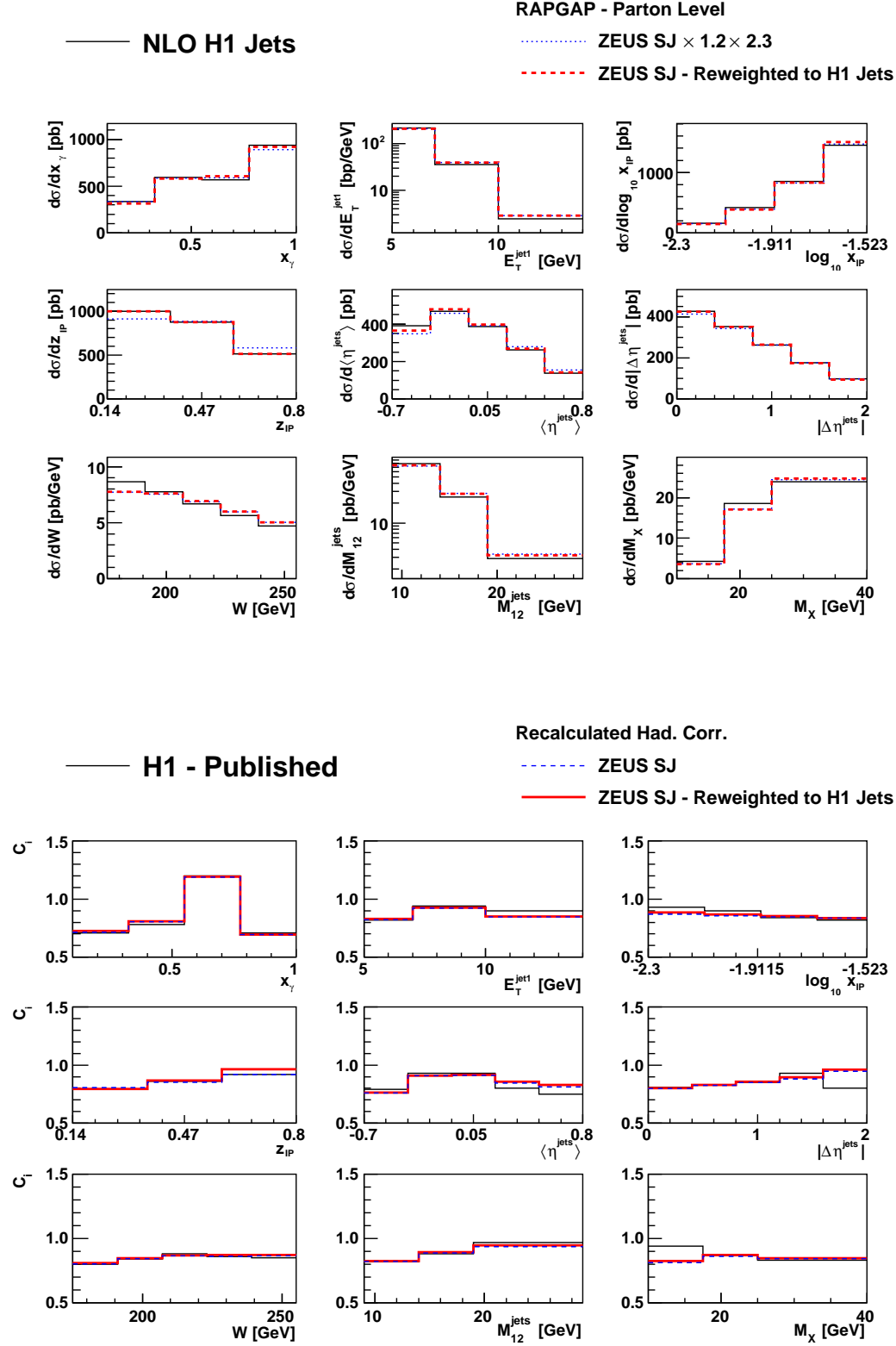


Fig. 4.6: At the top: correspondence between NLO and parton-level RAPGAP (before and after reweighting).

At the bottom: Hadronization correction calculated by means of RAPGAP.

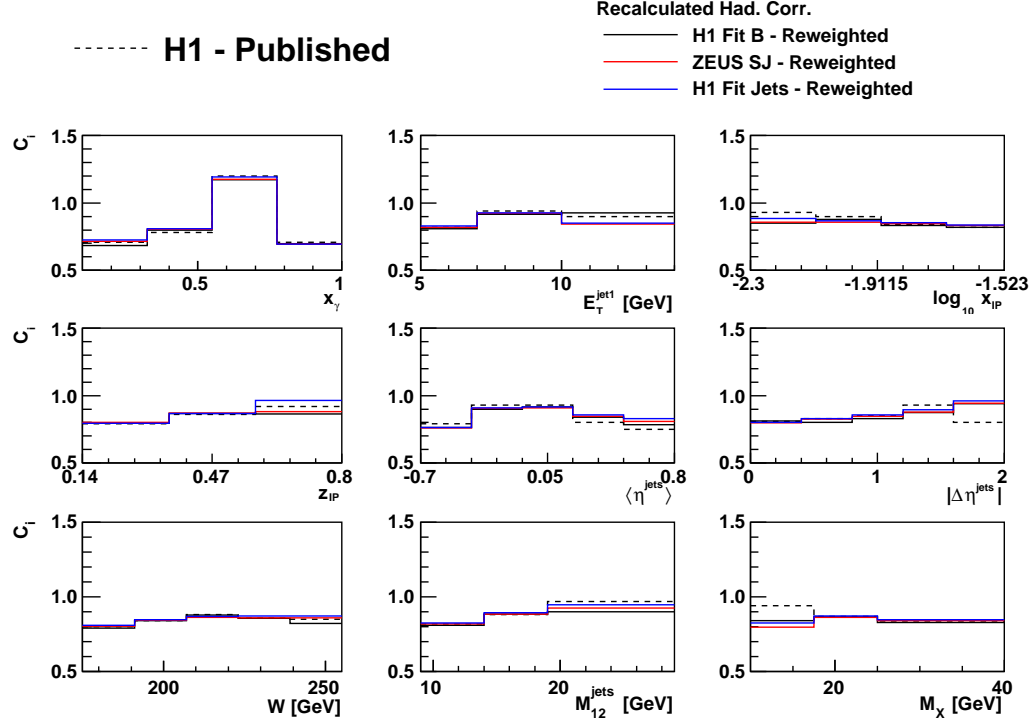


Fig. 4.7: Hadronization corrections  $C_i$  recalculated for H1 Fit B, H1 Fit Jets and ZEUS SJ and GRV  $\gamma$ -PDF. HC were calculated by RAPGAP reweighted to NLO distributions. Hadronization corrections published by H1 in [32] are plotted by dashed black line.

	H1	ZEUS
H1 Fit B	0.84	0.92
H1 Fit Jets	0.85	0.95
ZEUS SJ	0.85	0.93
Published	0.85	1.08

Tab. 4.1: The mean values ( $\sigma^{LO_{hadr}}/\sigma^{LO_{part}}$ ) of hadronization corrections.

sections for non-diffractive DIS dijet production [63] shows that hadronization corrections are smaller than unity and approach to unity with increasing of scale. Ratio between NLO to LO cross sections decreases with growing scale and is asymptotically getting to unity (see Fig. 4.12).

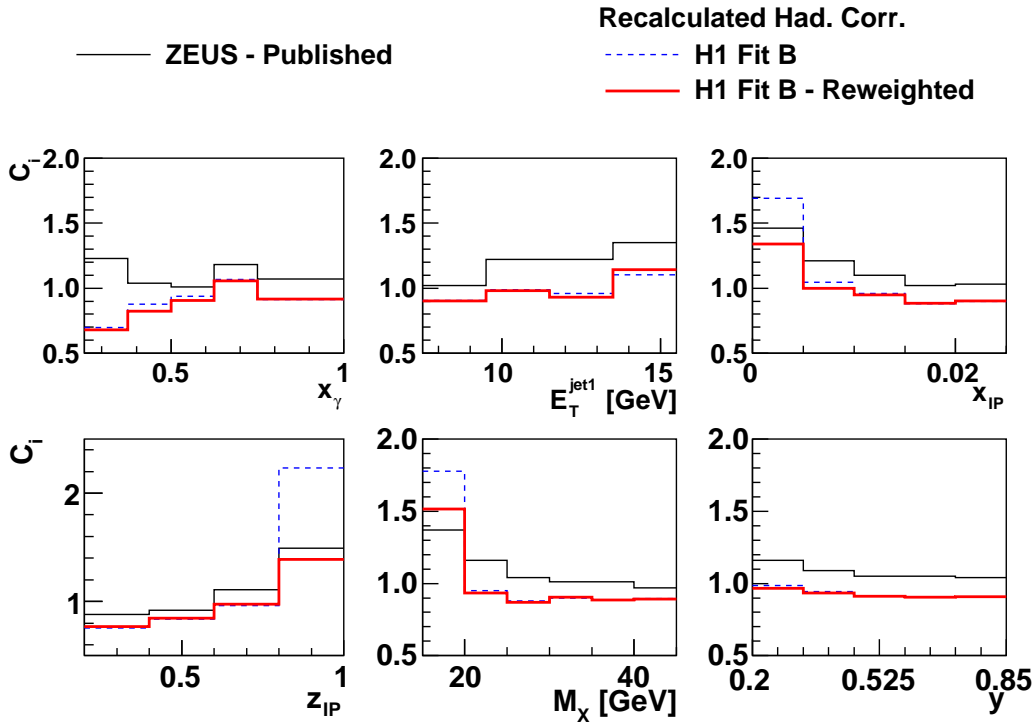
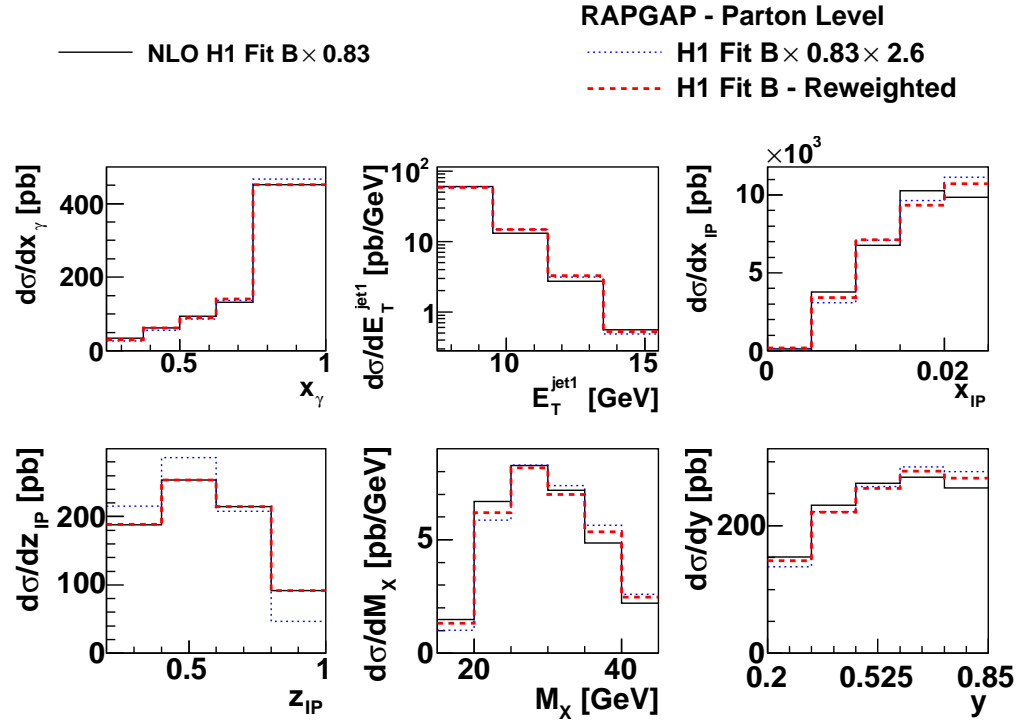


Fig. 4.8: At the top: correspondence between NLO and parton-level RAPGAP (before and after reweighting).

At the bottom: Hadronization correction calculated by means of RAPGAP.

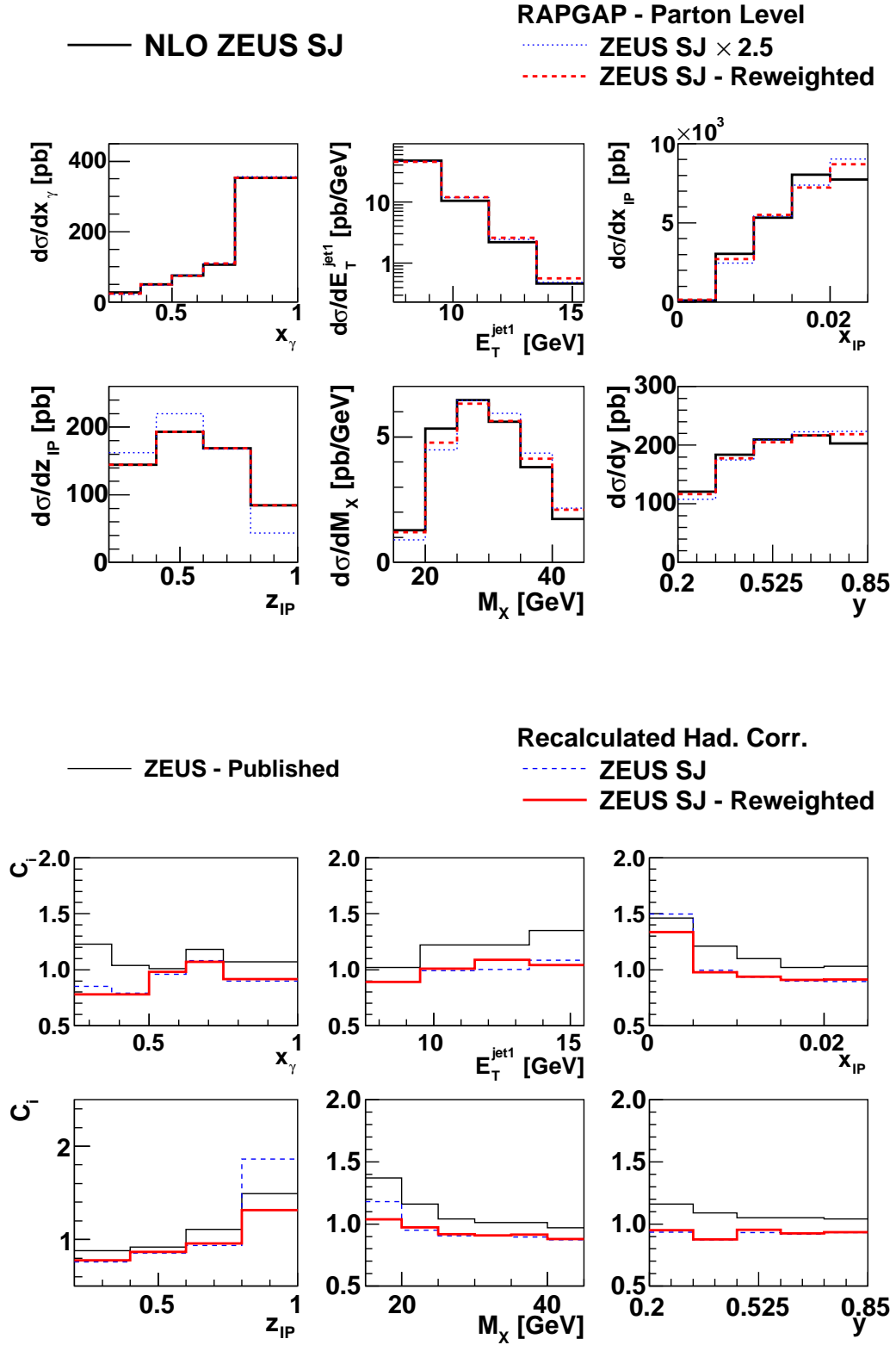


Fig. 4.9: At the top: correspondence between NLO and parton-level RAPGAP (before and after reweighting).

At the bottom: Hadronization correction calculated by means of RAPGAP.





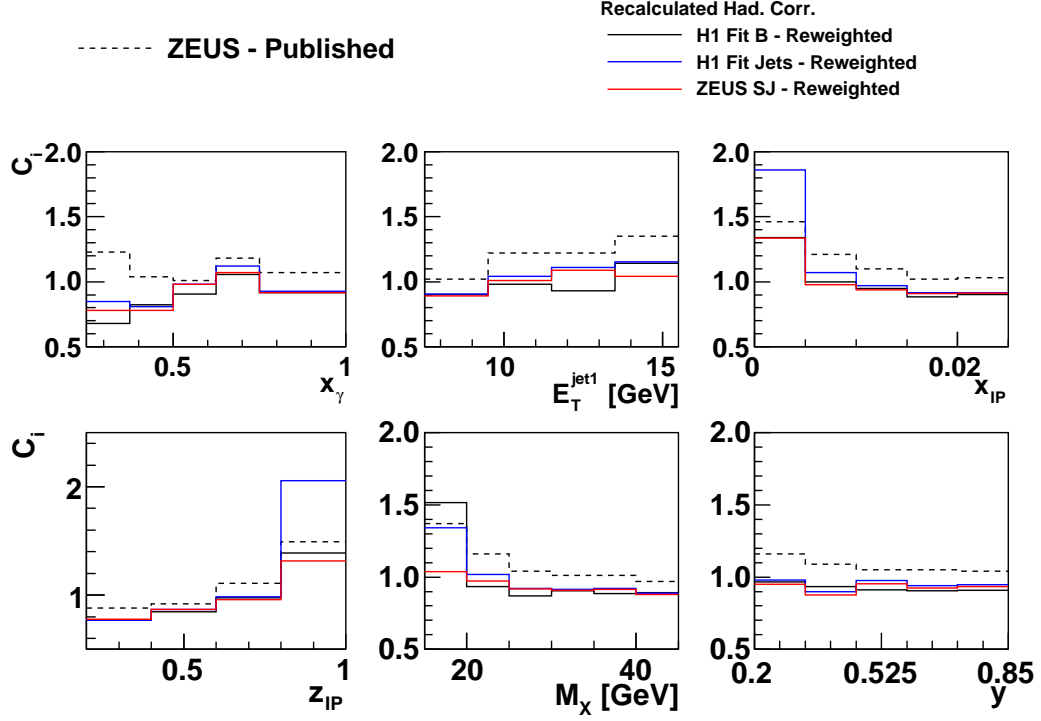


Fig. 4.11: Hadronization corrections  $C_i$  recalculated for H1 Fit B, H1 Fit Jets and ZEUS SJ and GRV  $\gamma$ -PDF. HC were calculated by RAPGAP reweighted to NLO distributions. Hadronization corrections published by ZEUS in [54] plotted as dashed black line.

#### 4.4 Hadron-Level NLO QCD Predictions

Estimating of hadron-level NLO cross sections from parton-level NLO calculations and hadronization correction is straightforward (4.9).

Results are shown in figures 4.13 and 4.14. Data are taken from H1 [32] and ZEUS [54] publications. Even after revision of NLO calculations remain the conclusions of both analyses unchanged - H1 data cross sections agree in shape with NLO predictions but are suppressed while in ZEUS case NLO calculations agree with the data. The difference between our NLO and ZEUS published calculations is caused by different hadronization corrections as it was discussed in previous section. Overall suppression factors are shown in Tab. 4.2.

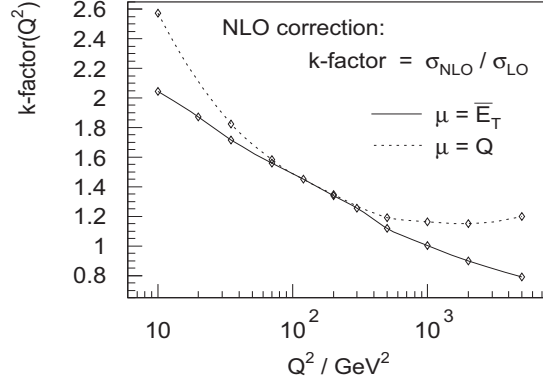


Fig. 4.12: Dependence of  $\sigma_{NLO}/\sigma_{LO}$  on scale for DIS dijet production [63].

	H1		ZEUS	
	revised	published	revised	published
H1 Fit B	0.57	0.58	0.88	0.77
H1 Fit Jets	0.63	0.64	1.08	1.01
ZEUS SJ	0.72	0.70	1.11	0.98

Tab. 4.2: Suppression factors ( $\sigma^{DATA}/\sigma^{NLO}$ ). Uncertainties of the data (QCD scale) are around 20 % (25 %) respectively.

## 4.5 Alternative Photon Structure Function

In the analysis mentioned above the GRV photon structure function [44] was used for NLO calculations and hadronization corrections. It was noticed [50] that the point-like part of the resolved contribution in GRV could be overestimated by about 25 % in comparison with more recent AFG photon structure function [45].

In this section the NLO calculations using AFG and GRV  $\gamma$ -PDF will be compared. To proceed in a correct way, the hadronization corrections must be also recalculated. Unfortunately AFG is available only in NLO  $\overline{\text{MS}}$  version. It can be however simply transformed to  $\text{DIS}_\gamma$  scheme which is more similar to LO (see Fig. 4.3). Even after this transformation is RAPGAP with GRV LO closer to NLO cross sections with AFG than RAPGAP with AFG  $\text{DIS}_\gamma$ . Therefore MC calculations were performed with GRV photon structure function and the parton-level distributions were reweighted to NLO. Only one representative DPDF for each phase space was chosen – H1 Fit B for H1 kinematics and ZEUS SJ for ZEUS phase space.

Calculations of AFG NLO cross sections were however not straightforward as it

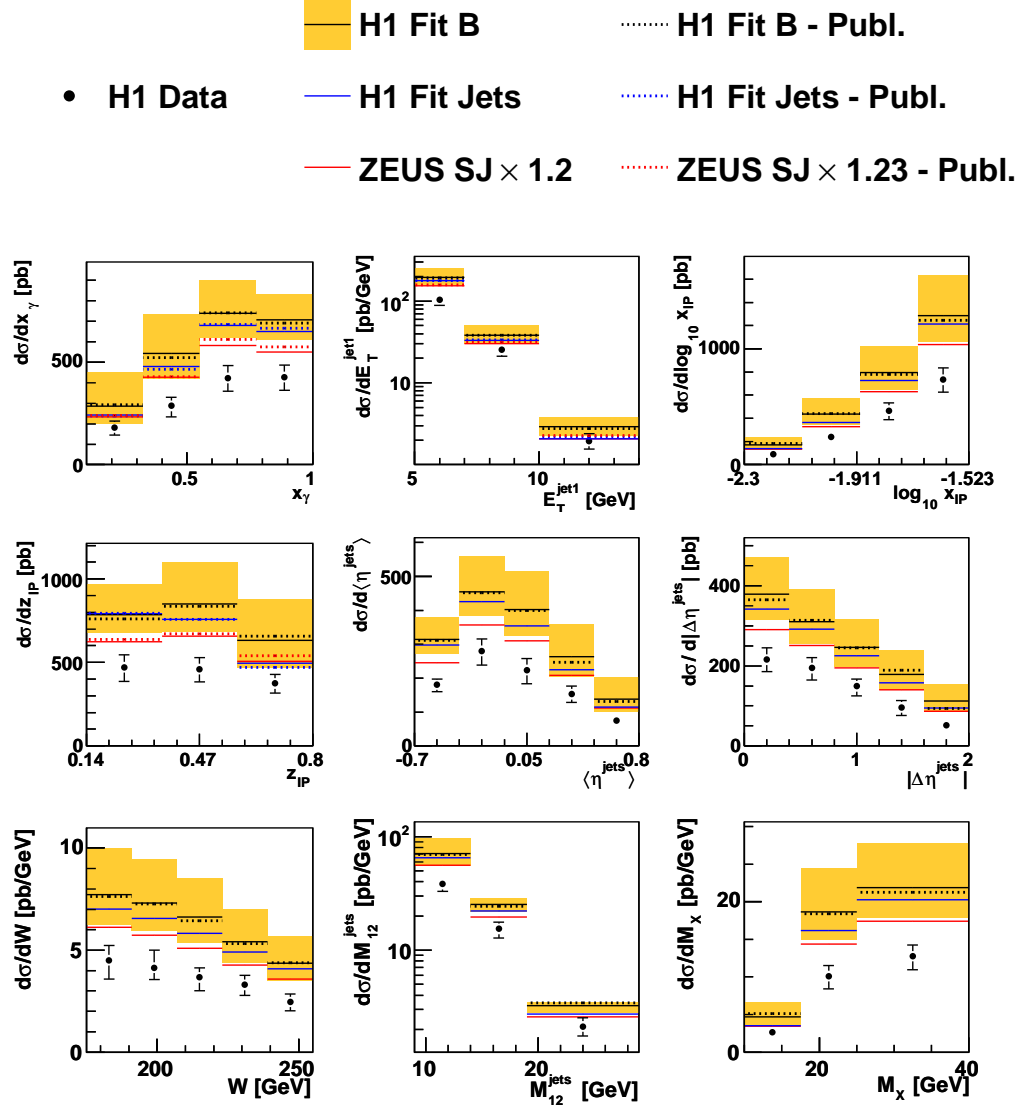


Fig. 4.13: NLO calculation corrected for hadronization compared with H1 data. Scale uncertainty band is plotted for H1 Fit B DPDF, GRV  $\gamma$ -PDF is used everywhere. Published NLO calculations are plotted with dotted line.

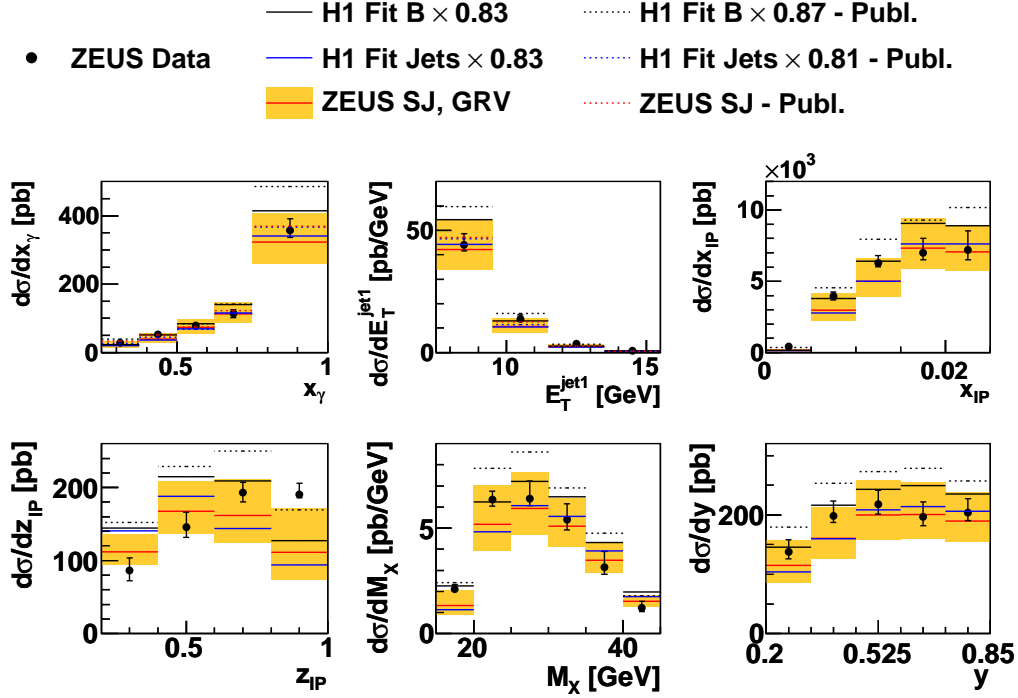


Fig. 4.14: NLO calculation corrected for hadronization compared with ZEUS data. Scale uncertainty band is plotted for ZEUS SJ DPDF, GRV  $\gamma$ -PDF is used everywhere. Published NLO calculations are plotted with dotted line.

was expected because of the bug in PDFs libraries which caused that AFG NLO cross sections were approx. 50 % higher than GRV NLO cross sections. Indeed u and d (anti-)quark densities implemented in PDFLIB [64] and LHAPDF [65] libraries were two times higher than in correct AFG fit. The librarians of LHAPDF were contacted and the bug was fixed<sup>2</sup>. In older not further supported PDFLIB this bug still persists.

NLO parton-level and MC parton-level distributions are compared in figures 4.15 and 4.16. In addition NLO with GRV is plotted which makes possible to compare NLO at parton-level with different photon PDFs. RAPGAP is reweighted by the same method as described before.

NLO calculations corrected for hadronization are shown in Fig. 4.17 and 4.18. Differential cross sections calculated with AFG photon structure function are really smaller. The change of photon PDF affects mostly resolved part  $x_\gamma \lesssim 0.75$  so the influence to the total cross section is higher for H1 kinematics where resolved part dominates. Overall suppression factors for both photon structure functions can be seen in Tab. 4.3.

	H1		ZEUS	
	GRV	AFG	GRV	AFG
all	0.57	0.63	1.11	1.16
direct	0.60	0.63	1.11	1.12
resolved	0.56	0.63	1.11	1.27

Tab. 4.3: Comparison of the total suppression factors ( $\sigma^{DATA}/\sigma^{NLO}$ ) for GRV and AFG  $\gamma$ -PDF. Experimental limit between direct and resolved part is 0.80 in H1 and 0.75 in ZEUS kinematic region which corresponds to the width of the highest  $x_\gamma$  bin. Uncertainties of the data (QCD scale) are around 20 % (25 %) respectively.

---

<sup>2</sup>See the patch from 11.11.2010 at <http://projects.hepforge.org/lhapdf/patches-5.8.4>

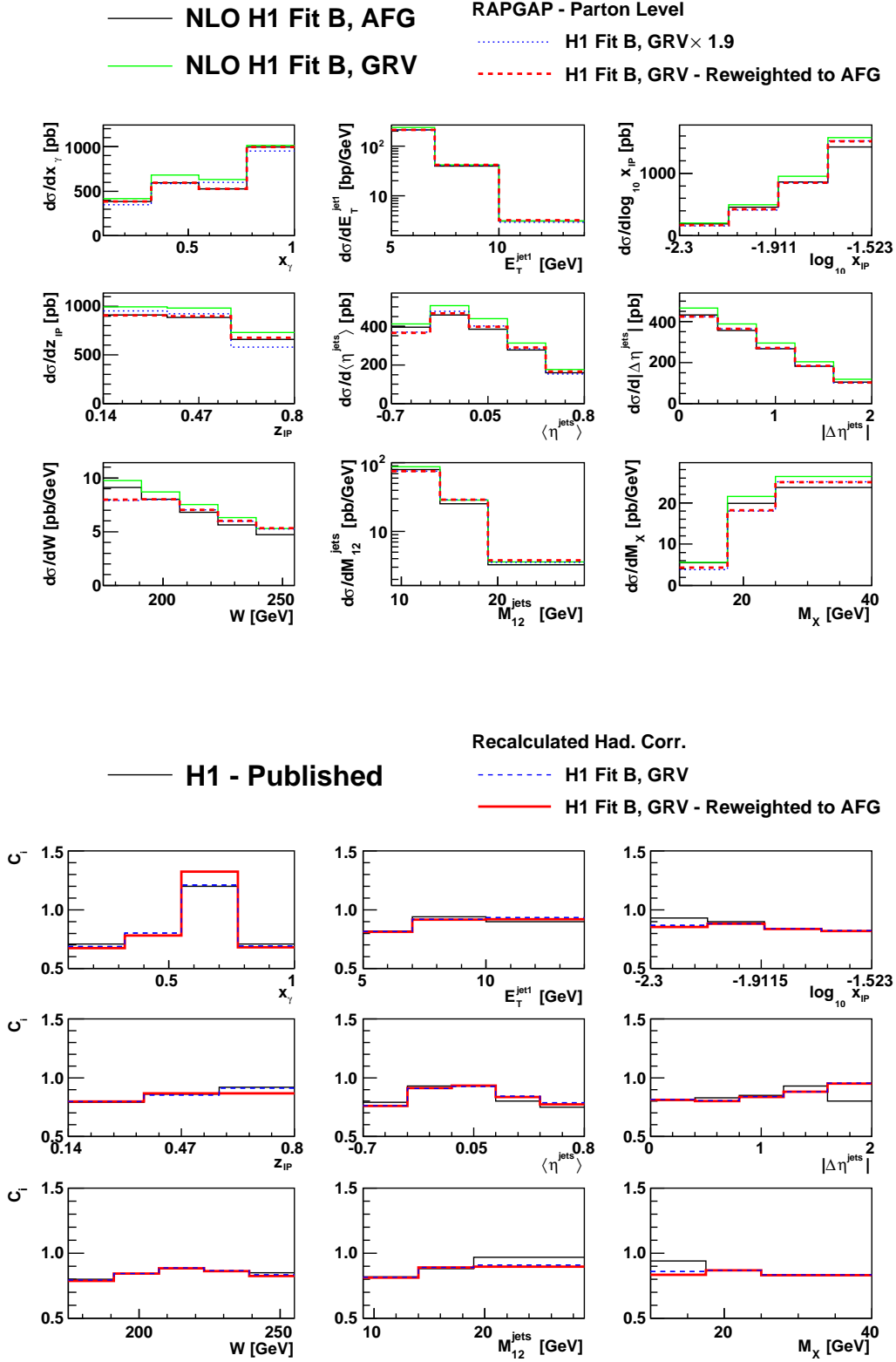


Fig. 4.15: At the top: correspondence between NLO and parton-level RAPGAP (before and after reweighting).

At the bottom: Hadronization correction calculated by means of RAPGAP.

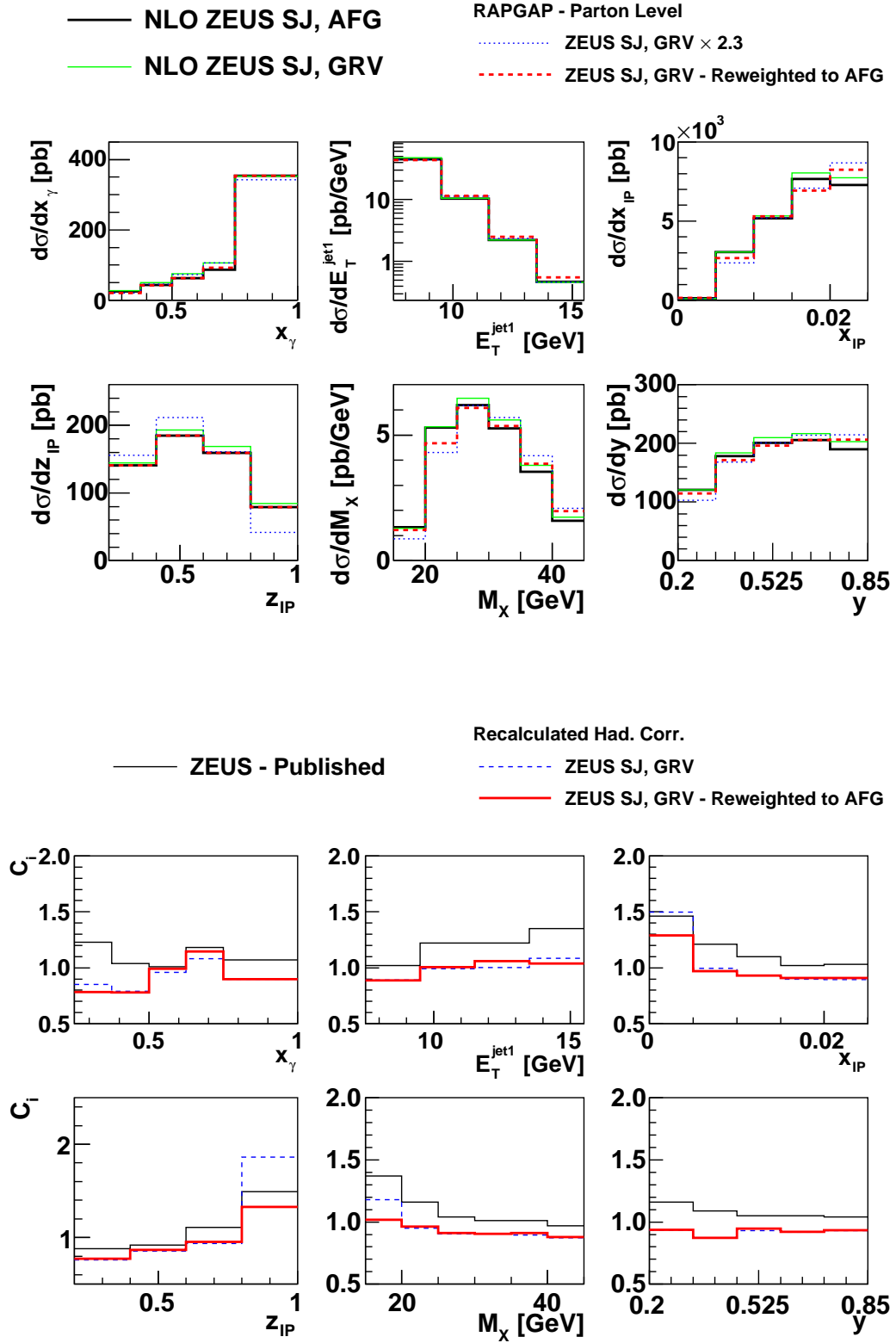


Fig. 4.16: At the top: correspondence between NLO and parton-level RAPGAP (before and after reweighting).

At the bottom: Hadronization correction calculated by means of RAPGAP.

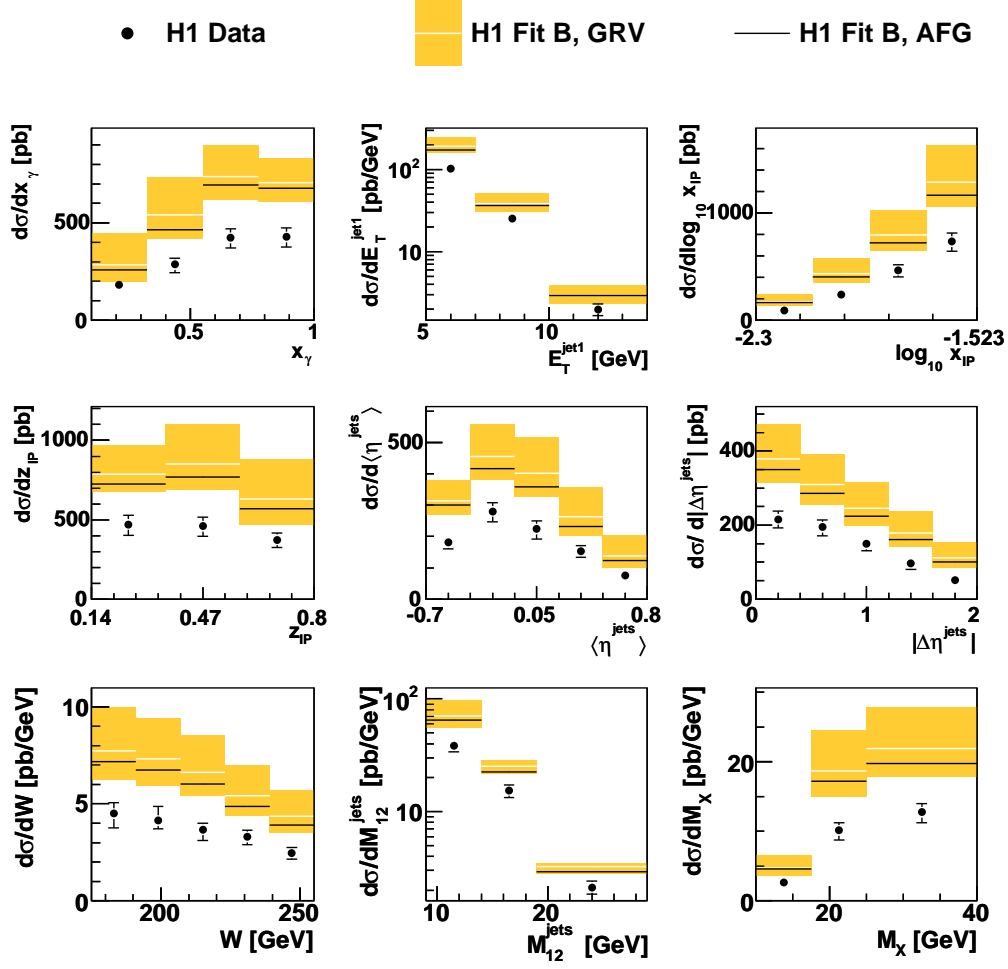


Fig. 4.17: NLO calculation using GRV and AFG  $\gamma$ -PDF corrected for hadronization compared with H1 data.



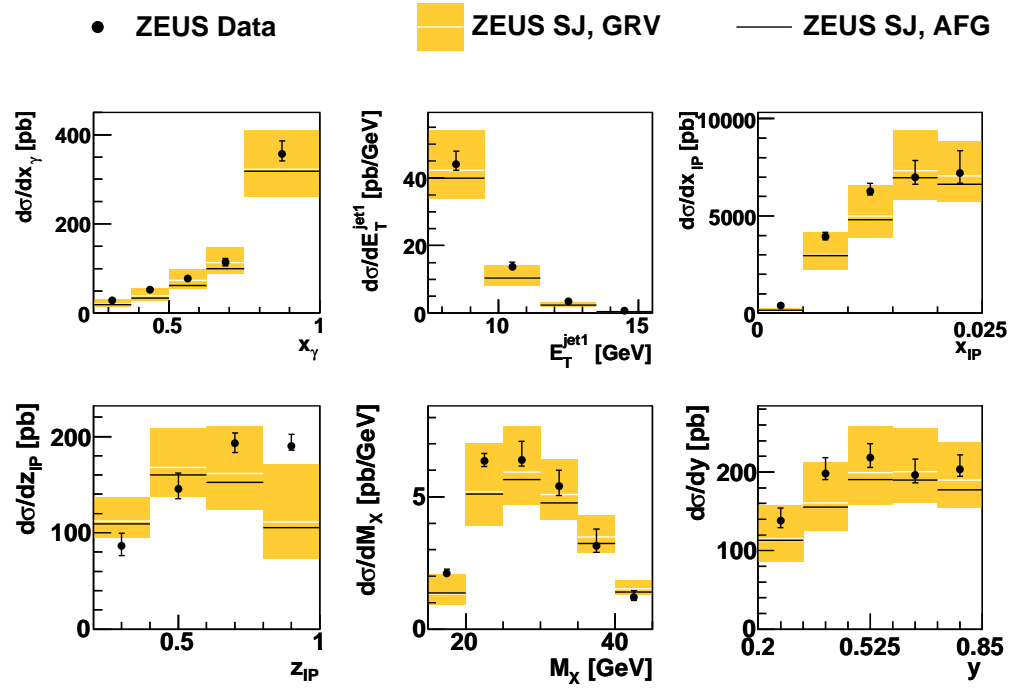


Fig. 4.18: NLO calculation using GRV and AFG  $\gamma$ -PDF corrected for hadronization compared with ZEUS data.

## Chapter 5

# Extrapolation between Measurements

H1 [32] and ZEUS [54] data cannot be compared directly since they were measured in different kinematic regions. It was suspected that contradictory conclusions can be caused by different cuts on  $E_T$  of the jets in H1 and ZEUS analysis. It was observed in H1 analysis [66] that the suppression decreases with increasing  $E_T$  of the leading jet. To study this effect in a more detailed way the H1 Hight Pt analysis [55] was done with the cuts similar to ZEUS analysis. The only differences between both analyses are in  $y$ ,  $Q^2$  and  $M_Y$  cuts (see Fig. 5.1). Suppression factor in [55] was really smaller (0.61 whereas Low Pt analysis gives 0.58, both for H1 Fit B DPDF) but it was still present.

Our next challenge is to test the compatibility of all three data sets. It will be done by the transformation of data sets from one kinematic region to another. MC model will be tuned to the data which will reduce model dependence of this procedure.

Overview of all three phase spaces is shown in Fig. 5.1. The arrows illustrate directions of the extrapolation between data sets. The method is more accurate if the phase spaces differ only a little and if the final phase space is a subset of the initial one.

### 5.1 Description of the Method

For concreteness we will discuss extrapolation from ZEUS to H1 High Pt phase space (red arrow in Fig. 5.1).

For this purpose a matrix is constructed, by means of MC RAPGAP, which accounts on transition from the ZEUS phase space to that of H1 High Pt,  $\mathbf{M}_{Z \rightarrow H}$ . The matrix is determined separately for each pair of corresponding differential cross

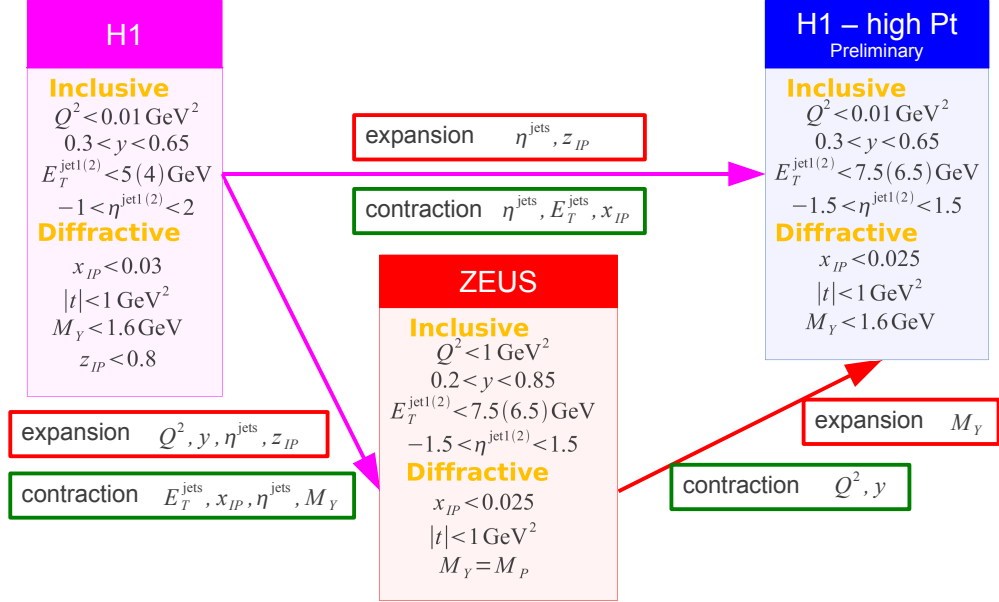


Fig. 5.1: Scheme of extrapolations between measurements [32, 55, 54] which have been done in this thesis.

sections from both analyses ( $x_\gamma^Z - x_\gamma^H$ ,  $E_T^{Z\text{jet1}} - E_T^{H\text{jet1}}$ , ...,  $y^Z - W^{H1}$ ). The matrix contains the probabilities that a particular event belonging to the  $i$ -th bin will end up in the  $j$ -th one of the given cross section as one makes the transition from the ZEUS to the H1 High Pt analysis phase space. Although the shapes of differential cross sections measured by ZEUS are rather well described by MC, to achieve a higher accuracy of the matrix determination, the MC spectra are reweighted to match the data better.

In general case (other extrapolations in Fig. 5.1) the contribution of events generated outside of the initial phase space but fulfilling cuts in final one needs to be taken into account. The normalization of this contribution is provided by the previously discussed reweighting of MC. The including of these events depends on the validity of used model in the region uncovered by the data in initial phase space. For each variable the result of the extrapolation procedure is given by a histogram  $\sigma_H$  determined as

$$\sigma_H = \mathbf{M}_{Z \rightarrow H} \sigma_Z + \sigma_H^{\text{add}} \quad (5.1)$$

where  $\sigma_Z$  is the vector of values of the measured cross sections (not-differential) for

<sup>1</sup>Because  $W$  and  $y$  are in photoproduction binded by relation  $W = \sqrt{ys}$

certain kinematic variable and  $\sigma_H^{add}$  is the contribution from outside of the initial phase space.

In all cases RAPGAP MC with H1 Fit B DPDF and GRV  $\gamma$ -PDF is used.

Uncertainties of the extrapolated data are determined by propagations of the original errors by means of the matrix  $\mathbf{M}_{Z \rightarrow H}$ . The relative uncertainty of the  $\sigma_H^{add}$  is assumed to be the same as the one of the total published cross section in initial phase space.

## 5.2 H1 Low Pt $\rightarrow$ H1 High Pt

This transformation was provided to test the method.

Cut on  $x_{IP}$  and  $E_T$  are in final phase space tighter whereas the range in  $z_{IP}$  is extended. Fortunately in H1 Low Pt analysis exists measurement in bin  $z_{IP} \in (0.8, 1)$  (without applying  $z_{IP}$  cut) so the MC can be tuned by reweighting in  $z_{IP}$  to the data in the full  $z_{IP}$  range. Cuts on pseudorapidities changed from  $-1 < \eta^{\text{jets}} < 2$  to  $-1.5 < \eta^{\text{jets}} < 1.5$ . Comparison of the H1 Low Pt data with reweighted MC is shown at the upper part of Fig. 5.2.

Results of this extrapolation at the lower part of Fig. 5.2 show that within the errors are both measurements compatible. The ratio of the extrapolated cross section to the H1 High Pt cross section [55] is:

$$\sigma_{extrap}^{\text{H1lowPt}} / \sigma^{\text{H1highPt}} = 1.0 \pm 0.1 \quad (5.2)$$

## 5.3 ZEUS $\rightarrow$ H1 High Pt

Bridging of ZEUS and H1 High Pt phase space is the first test of compatibility of the data between collaborations. These two phase spaces have very similar kinematics cuts. The range of  $y$  and  $Q^2$  variables must be however reduced. Different  $M_Y$  range is taken into account by using of the global factor 1.2 (see section 3.3).

Control plots and the results of the extrapolation can be seen in Fig. 5.3. The total cross sections ratio is

$$\sigma^{\text{H1highPt}} / \sigma_{extrap}^{\text{ZEUS}} = 0.6 \pm 0.1 \quad (5.3)$$

where  $\sigma^{\text{H1highPt}}$  is the total cross section from [55] and  $\sigma_{extrap}^{\text{ZEUS}}$  is the total cross section of extrapolated ZEUS data [54].

## 5.4 H1 Low Pt $\rightarrow$ ZEUS

Matching H1 and ZEUS results from publications [32] and [54] is the most complicated case because phase spaces differ substantially. Here is even not obvious what direction of extrapolation to choose.

We proceeded in two steps.

At the first step the H1 data were converted to  $Q^2 < 1 \text{ GeV}^2$  range applying of bin by bin correction factors which were estimated from RAPGAP. Change of  $Q^2$  range increases the cross sections by factor about 35 %.

In the second step the method of extrapolation (5.1) was applied to this extended data set. Due to the different  $M_Y$  cuts in the analyses the H1 data must be divided by global factor 1.2 (see section 3.3).

Results of the last extrapolation are plotted in Fig. 5.4 together with ZEUS published data. It can be seen that after the transformation to the identical phase space the H1 differential cross sections are lower than the ZEUS results by factor about 0.6. On the other hand the shapes of H1 and ZEUS differential cross sections are very similar, except for  $z_{IP}$ . The uncertainties of the extrapolated H1 data were determined by propagation of the statistical and uncorrelated systematic errors from [32]. The relative uncertainty of  $\sigma_Z^{add}$  was assumed to be the same as the one of the total cross section from [32].

The ratio of extrapolated cross sections to ZEUS published cross section is

$$\sigma_{extrap}^{\text{H1lowPt}} / \sigma^{\text{ZEUS}} = 0.6 \pm 0.2. \quad (5.4)$$

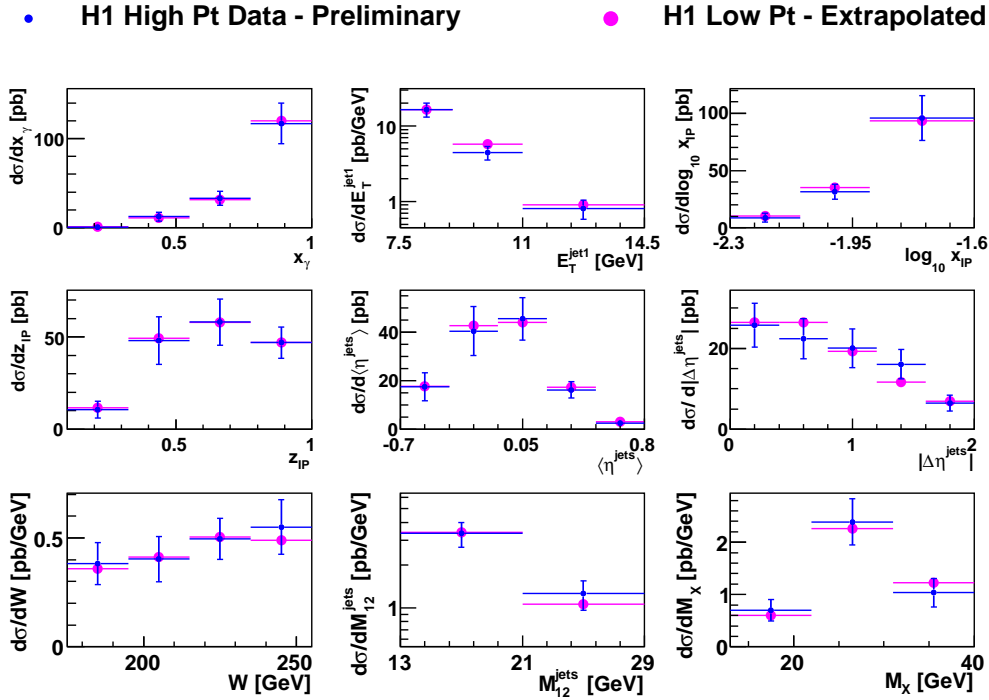
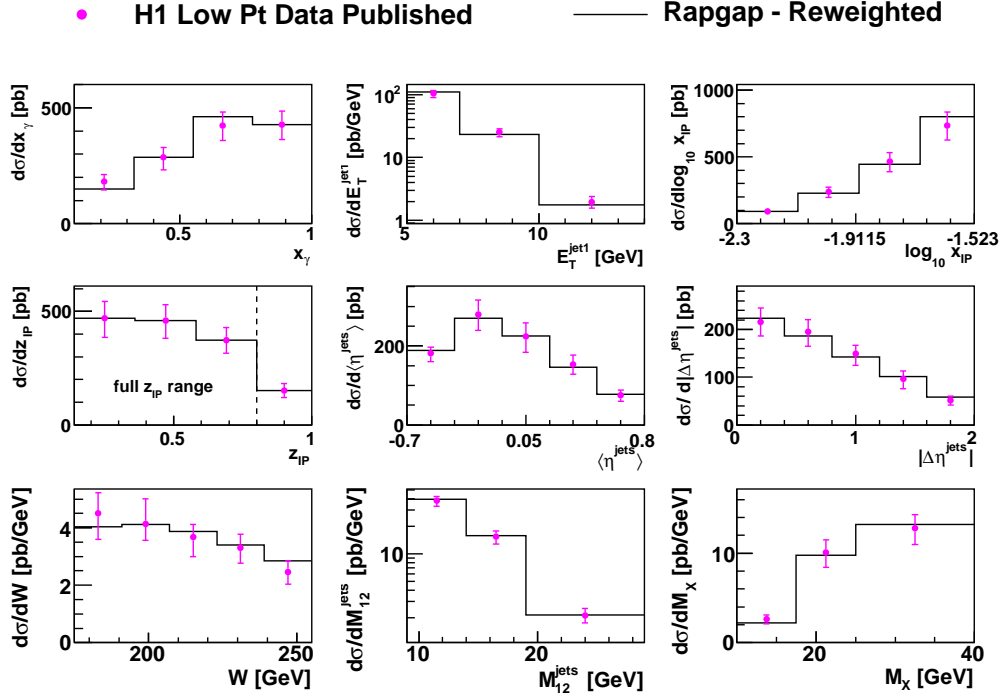


Fig. 5.2: *At the top:* Control plots which show the agreement between reweighted RAPGAP and H1 data.

*At the bottom:* Comparison between H1 High Pt Preliminary data and extrapolated H1 Low Pt data.

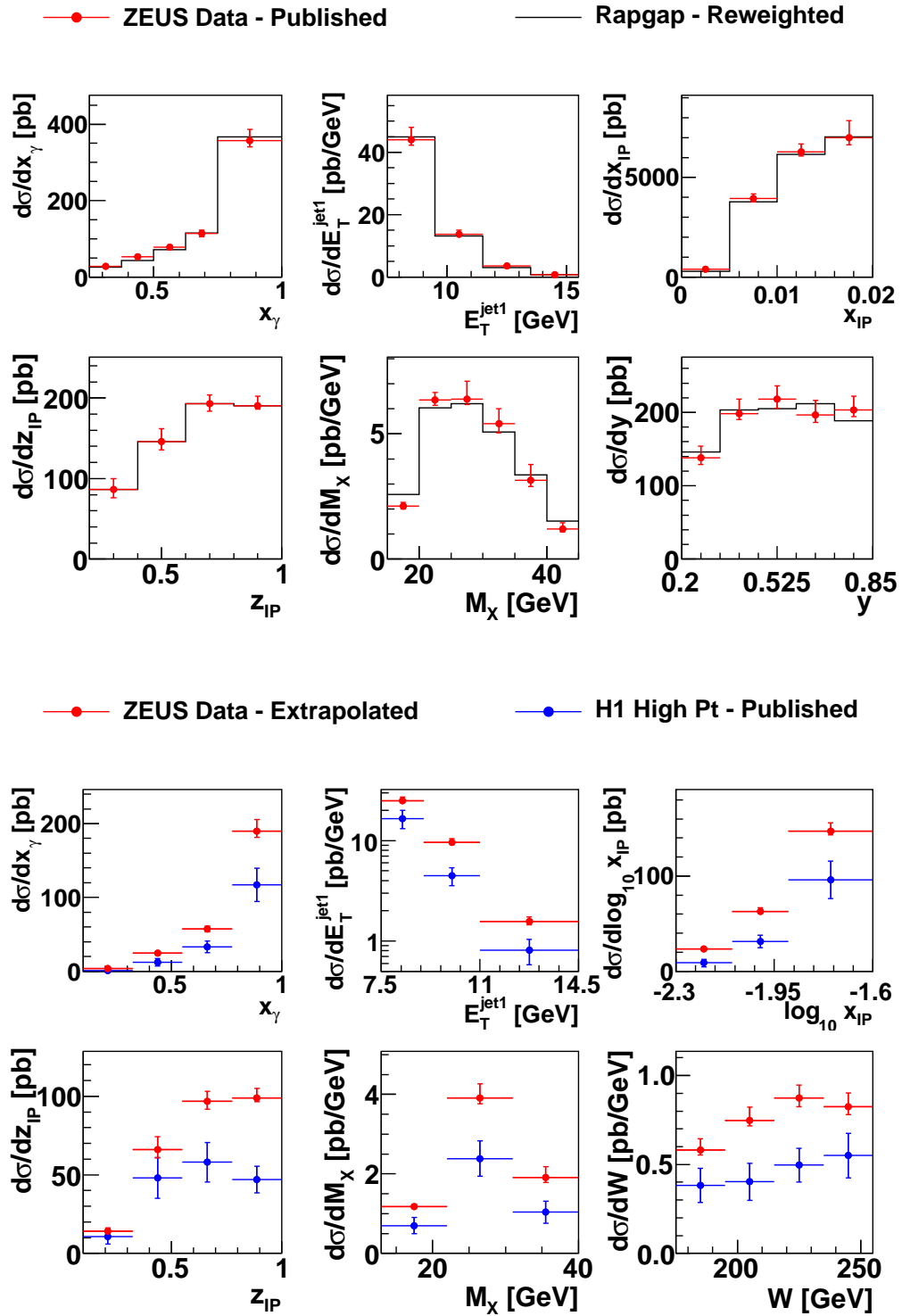


Fig. 5.3: *At the top:* Control plots which show the agreement between reweighted RAPGAP and ZEUS data.

*At the bottom:* Comparison between H1 High Pt preliminary data and extrapolated ZEUS data.

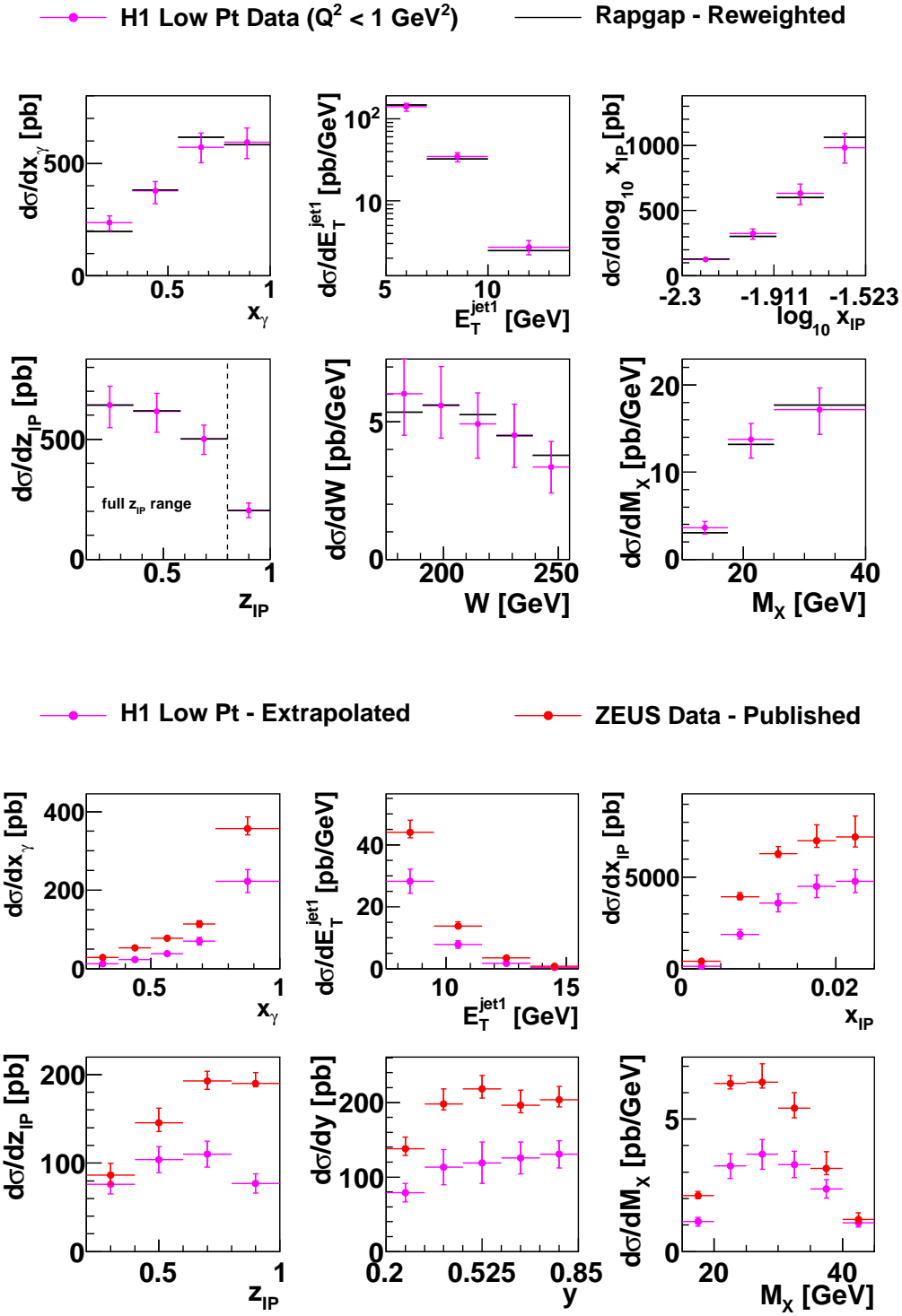


Fig. 5.4: *At the top:* Control plots which show the agreement between reweighted RAPGAP and H1 data unfolded to  $Q^2 < 1 \text{ GeV}^2$ .

*At the bottom:* Comparison between ZEUS published data and extrapolated H1 data.



## Chapter 6

# Conclusions

The analysis of published H1 and ZEUS results is done with the emphasis to understand better the possible sources of the discrepancies between the conclusions of both collaborations. It is shown that results are not significantly sensitive to the photon structure function used. Although, here the different hadronization corrections are obtained than in [54], it has no crucial impact to the interpretation of ZEUS differential cross sections. The conversion of H1 results to ZEUS phase space is done. The shapes of differential cross sections measured by both collaborations are in agreement (except for  $z_{IP}$  variable), however, the H1 results are on average lower by about 40 % than ZEUS ones. Within the limitations of the transformation method (based on Monte Carlo) there is a suggestion that the observed discrepancy between H1 and ZEUS results concerning factorisation breaking is not caused by different phase space of both analyses. The puzzle of factorisation breaking in diffractive dijet photoproduction could be resolved therefore by new experimental analyses. Among them the most promising one could be the identification of diffractive events based on leading proton detection. This method has both an advantage of providing a data sample free of proton dissociation and of reducing the uncertainties of the diffractive selection if compared with large rapidity gap method.

# Bibliography

- [1] J. Callan, Curtis G. and D. J. Gross, “High-energy electroproduction and the constitution of the electric current,” *Phys.Rev.Lett.* **22** (1969) 156–159.
- [2] E. D. Bloom, D. Coward, H. DeStaebler, J. Drees, G. Miller, *et al.*, “High-Energy Inelastic e p Scattering at 6-Degrees and 10-Degrees,” *Phys.Rev.Lett.* **23** (1969) 930–934.
- [3] M. Gell-Mann, “A Schematic Model of Baryons and Mesons,” *Phys.Lett.* **8** (1964) 214–215.
- [4] **H1 and ZEUS** Collaboration, F. D. Aaron *et al.*, “Combined Measurement and QCD Analysis of the Inclusive ep Scattering Cross Sections at HERA,” *JHEP* **01** (2010) 109, [arXiv:0911.0884 \[hep-ex\]](#).
- [5] K. G. Wilson, “Confinement of Quarks,” *Phys.Rev.* **D10** (1974) 2445–2459.
- [6] J. Chýla, “Quarks, partons and Quantum Chromodynamics,”.
- [7] E. Glover, “Progress in NNLO calculations for scattering processes,” *Nucl.Phys.Proc.Suppl.* **116** (2003) 3–7, [arXiv:hep-ph/0211412 \[hep-ph\]](#).
- [8] S. Moch and A. Vogt, “Higher-order soft corrections to lepton pair and Higgs boson production,” *Phys.Lett.* **B631** (2005) 48–57, [arXiv:hep-ph/0508265 \[hep-ph\]](#).
- [9] V. Gribov and L. Lipatov, “Deep inelastic e p scattering in perturbation theory,” *Sov.J.Nucl.Phys.* **15** (1972) 438–450.
- [10] R. Ellis, W. Stirling, and B. Webber, “QCD and collider physics,” *Camb.Monogr.Part.Phys.Nucl.Phys.Cosmol.* **8** (1996) 1–435.
- [11] T. Kinoshita, “Mass singularities of Feynman amplitudes,” *J.Math.Phys.* **3** (1962) 650–677.

- [12] T. Sjostrand, “High-energy physics event generation with PYTHIA 5.7 and JETSET 7.4,” *Comput.Phys.Commun.* **82** (1994) 74–90.
- [13] H. Jung, “Hard diffractive scattering in high-energy e p collisions and the Monte Carlo generator RAPGAP,”  
*Comp. Phys. Commun.* **86** (1995) 147–161.
- [14] G. Marchesini, B. Webber, G. Abbiendi, I. Knowles, M. Seymour, *et al.*,  
“HERWIG: A Monte Carlo event generator for simulating hadron emission reactions with interfering gluons. Version 5.1 - April 1991,”  
*Comput.Phys.Commun.* **67** (1992) 465–508.
- [15] S. Catani, Y. L. Dokshitzer, and B. Webber, “The K-perpendicular clustering algorithm for jets in deep inelastic scattering and hadron collisions,”  
*Phys.Lett.* **B285** (1992) 291–299.
- [16] S. D. Ellis and D. E. Soper, “Successive combination jet algorithm for hadron collisions,” *Phys.Rev.* **D48** (1993) 3160–3166,  
[arXiv:hep-ph/9305266](#) [hep-ph].
- [17] U. Amaldi, M. Jacob, and G. Matthiae, “Diffraction of Hadronic Waves,”  
*Ann.Rev.Nucl.Part.Sci.* **26** (1976) 385–456.
- [18] V. Barone and E. Predazzi, “High-energy particle diffraction,”. Berlin, Germany: Springer (2002) 407 p.
- [19] T. Regge, “Introduction to complex orbital momenta,”  
*Nuovo Cim.* **14** (1959) 951.
- [20] **UA8 Collaboration** Collaboration, R. Bonino *et al.*, “Evidence for Transverse Jets in High Mass Diffraction,” *Phys.Lett.* **B211** (1988) 239.
- [21] G. Ingelman and P. Schlein, “Jet Structure in High Mass Diffractive Scattering,” *Phys.Lett.* **B152** (1985) 256.
- [22] **ZEUS Collaboration** Collaboration, M. Derrick *et al.*, “Observation of events with a large rapidity gap in deep inelastic scattering at HERA,”  
*Phys.Lett.* **B315** (1993) 481–493.
- [23] A. Donnachie and P. Landshoff, “Total cross-sections,”  
*Phys.Lett.* **B296** (1992) 227–232, [arXiv:hep-ph/9209205](#) [hep-ph].
- [24] **H1 Collaboration**, A. Aktas *et al.*, “Measurement and QCD analysis of the diffractive deep- inelastic scattering cross-section at HERA,”  
*Eur. Phys. J.* **C48** (2006) 715–748, [arXiv:hep-ex/0606004](#).

- [25] J. C. Collins, “Proof of factorization for diffractive hard scattering,” *Phys.Rev.* **D57** (1998) 3051–3056, [arXiv:hep-ph/9709499](#) [[hep-ph](#)].
- [26] J. Binnewies, “Fragmentation functions in next-to-leading order QCD,” [arXiv:hep-ph/9707269](#) [[hep-ph](#)].
- [27] A. B. Kaidalov, V. A. Khoze, A. D. Martin, and M. G. Ryskin, “Factorization breaking in diffractive dijet production,” *Phys. Lett.* **B559** (2003) 235–238, [arXiv:hep-ph/0302091](#).
- [28] E. Witten, “Anomalous Cross-Section for Photon - Photon Scattering in Gauge Theories,” *Nucl.Phys.* **B120** (1977) 189–202.
- [29] C. von Weizsacker, “Radiation emitted in collisions of very fast electrons,” *Z.Phys.* **88** (1934) 612–625.
- [30] E. Williams, “Nature of the high-energy particles of penetrating radiation and status of ionization and radiation formulae,” *Phys.Rev.* **45** (1934) 729–730.
- [31] B. Potter, “Inclusive single- and dijet rates in next-to-leading order QCD for  $\gamma^* p$  and  $\gamma^* \gamma$  collisions,” *Eur. Phys. J. direct* **C1** (1999) 5, [arXiv:hep-ph/9707319](#).
- [32] **H1 Collaboration**, F. D. Aaron *et al.*, “Diffractive Dijet Photoproduction in ep Collisions at HERA,” [arXiv:1006.0946](#) [[hep-ex](#)].
- [33] **ZEUS Collaboration** Collaboration, J. Breitweg *et al.*, “Measurement of the diffractive cross-section in deep inelastic scattering using ZEUS 1994 data,” *Eur.Phys.J.* **C6** (1999) 43–66, [arXiv:hep-ex/9807010](#) [[hep-ex](#)].
- [34] **ZEUS Collaboration** Collaboration, J. Breitweg *et al.*, “Measurement of the diffractive structure function  $F_2(D(4))$  at HERA,” *Eur.Phys.J.* **C1** (1998) 81–96, [arXiv:hep-ex/9709021](#) [[hep-ex](#)].
- [35] **H1 Collaboration** Collaboration, A. Aktas *et al.*, “Diffractive deep-inelastic scattering with a leading proton at HERA,” *Eur.Phys.J.* **C48** (2006) 749–766, [arXiv:hep-ex/0606003](#) [[hep-ex](#)].
- [36] J. Owens, “ $Q^2$  Dependent Parametrizations of Pion Parton Distribution Functions,” *Phys.Rev.* **D30** (1984) 943.
- [37] and others, “Measurement of the Diffractive Deep-Inelastic Scattering Cross Section with a Leading Proton at HERA,” [arXiv:1010.1476](#) [[hep-ex](#)].

- [38] **H1 Collaboration**, A. Aktas *et al.*, “Dijet Cross Sections and Parton Densities in Diffractive DIS at HERA,” *JHEP* **10** (2007) 042, [arXiv:0708.3217 \[hep-ex\]](#).
- [39] **ZEUS Collaboration**, S. Chekanov *et al.*, “Dijet production in diffractive deep inelastic scattering at HERA,” *Eur.Phys.J.* **C52** (2007) 813–832, [arXiv:0708.1415 \[hep-ex\]](#).
- [40] S. Frixione, “A General approach to jet cross-sections in QCD,” *Nucl. Phys.* **B507** (1997) 295–314, [arXiv:hep-ph/9706545](#).
- [41] **ZEUS Collaboration**, S. Chekanov *et al.*, “A QCD analysis of ZEUS diffractive data,” *Nucl. Phys.* **B831** (2010) 1–25, [arXiv:0911.4119 \[hep-ex\]](#).
- [42] **CDF Collaboration**, A. A. Affolder *et al.*, “Diffractive dijets with a leading antiproton in  $\bar{p}p$  collisions at  $\sqrt{s} = 1800$  GeV,” *Phys.Rev.Lett.* **84** (2000) 5043–5048.
- [43] V. A. Khoze, A. D. Martin, and M. Ryskin, “Can the Higgs be seen in rapidity gap events at the Tevatron or the LHC?,” *Eur.Phys.J.* **C14** (2000) 525–534, [arXiv:hep-ph/0002072 \[hep-ph\]](#).
- [44] M. Gluck, E. Reya, and A. Vogt, “Parton structure of the photon beyond the leading order,” *Phys. Rev.* **D45** (1992) 3986–3994.
- [45] P. Aurenche, J. P. Guillet, and M. Fontannaz, “Parton distributions in the photon,” *Z. Phys.* **C64** (1994) 621–630, [arXiv:hep-ph/9406382](#).
- [46] R. Nisius, “The photon structure from deep inelastic electron photon scattering,” *Phys. Rept.* **332** (2000) 165–317, [arXiv:hep-ex/9912049](#).
- [47] A. Kaidalov, V. Khoze, A. Martin, and M. Ryskin, “Unitarity effects in hard diffraction at HERA,” *Phys.Lett.* **B567** (2003) 61–68, [arXiv:hep-ph/0306134 \[hep-ph\]](#).
- [48] M. Klasen and G. Kramer, “Factorization breaking in diffractive dijet photoproduction,” *Eur.Phys.J.* **C38** (2004) 93–104, [arXiv:hep-ph/0408203 \[hep-ph\]](#).
- [49] M. Klasen and G. Kramer, “Suppression factors in diffractive photoproduction of dijets,” *Eur.Phys.J.* **C70** (2010) 91–106, [arXiv:1006.4964 \[hep-ph\]](#).
- [50] A. Kaidalov, V. Khoze, A. Martin, and M. Ryskin, “Factorization breaking in diffractive dijet photoproduction at HERA,” *Eur.Phys.J.* **C66** (2010) 373–376, [arXiv:0911.3716 \[hep-ph\]](#).

- [51] **H1 Collaboration**, A. Aktas *et al.*, “Tests of QCD factorisation in the diffractive production of dijets in deep-inelastic scattering and photoproduction at HERA,” *Eur. Phys. J.* **C51** (2007) 549–568, [arXiv:hep-ex/0703022](#).
- [52] **H1 Collaboration**, C. Adloff *et al.*, “Diffractive dijet production at HERA,” *Eur. Phys. J.* **C6** (1999) 421–436, [arXiv:hep-ex/9808013 \[hep-ex\]](#).
- [53] **ZEUS Collaboration**, J. Breitweg *et al.*, “Diffractive dijet cross-sections in photoproduction at HERA,” *Eur. Phys. J.* **C5** (1998) 41–56, [arXiv:hep-ex/9804013 \[hep-ex\]](#).
- [54] **The ZEUS Collaboration**, S. Chekanov *et al.*, “Diffractive photoproduction of dijets in  $ep$  collisions at HERA,” *Eur. Phys. J.* **C55** (2008) 177–191, [arXiv:0710.1498 \[hep-ex\]](#).
- [55] K. Cerny, “Tests of QCD hard factorization in diffractive photoproduction of dijets at HERA,”.
- [56] **H1 Collaboration**, A. Aktas *et al.*, “Diffractive open charm production in deep-inelastic scattering and photoproduction at HERA,” *Eur. Phys. J.* **C50** (2007) 1–20, [arXiv:hep-ex/0610076](#).
- [57] **ZEUS Collaboration**, S. Chekanov *et al.*, “Diffractive photoproduction of  $D^{*+}$ -(2010) at HERA,” *Eur. Phys. J.* **C51** (2007) 301–315, [arXiv:hep-ex/0703046 \[hep-ex\]](#).
- [58] S. Frixione, Z. Kunszt, and A. Signer, “Three jet cross-sections to next-to-leading order,” *Nucl. Phys.* **B467** (1996) 399–442, [arXiv:hep-ph/9512328 \[hep-ph\]](#).
- [59] M. Klasen and G. Kramer, “Inclusive two jet production at HERA: Direct and resolved cross-sections in next-to-leading order QCD,” *Z. Phys.* **C76** (1997) 67–74, [arXiv:hep-ph/9611450 \[hep-ph\]](#).
- [60] M. Botje, “QCDNUM: Fast QCD Evolution and Convolution,” *Comput. Phys. Commun.* **182** (2011) 490–532, [arXiv:1005.1481 \[hep-ph\]](#).
- [61] S. Kagawa, “Study of the diffractive photoproduction of dijets in  $e p$  collisions at HERA,”.
- [62] **H1 Collaboration**, C. Adloff *et al.*, “Inclusive measurement of diffractive deep inelastic  $ep$  scattering,” *Z. Phys.* **C76** (1997) 613–629, [arXiv:hep-ex/9708016 \[hep-ex\]](#).

- [63] M. Wobisch and T. Wengler, “Hadronization corrections to jet cross-sections in deep inelastic scattering,” [arXiv:hep-ph/9907280](#) [[hep-ph](#)].
- [64] H. Plathow-Besch, “PDFLIB: A Library of all available parton density functions of the nucleon, the pion and the photon and the corresponding  $\alpha_s$  calculations,” *Comput.Phys.Commun.* **75** (1993) 396–416.
- [65] M. Whalley, D. Bourilkov, and R. Group, “The Les Houches accord PDFs (LHAPDF) and LHAGLUE,” [arXiv:hep-ph/0508110](#) [[hep-ph](#)].
- [66] W. Slominski and A. Valkarova, “Diffractive final states and factorisation at HERA,”.